Characterization of the CMS Pixel Detectors

Von der Fakultät für Mathematik, Informatik und Naturwissenschaften zur Erlangung des akademsichen Grades einer Doktorin der Naturwissenchaften genehmigte Dissertaion

vorlegt von

Diplom-Physikerin
Weihua Gu
aus Shanghai, V.R. China

Berichter:	Universitätsprofessor Dr. K. Lübelsmeyer
	Universitätsprofessor Dr. St. Schael
Tag der mündlichen Prüfung:	30. Januar 2002

Contents

Chapter 1

Introduction

The Standard Model has enjoyed its great success through the years. But the ultimate understanding of electroweak symmetry breaking is still missing. The theory suggests that at least one scalar particle, the Higgs boson with a mass of less than roughly 1 TeV, can explain the observed mass spectrum of bosons and fermions. Supersymmetry explores a way to solve the fine tuning problem (i.e. the stability of the Fermi mass scale) of the Standard Model. The primary motivation of the new high energy proton-proton collider - LHC[1], with its two general purpose experiments ATLAS[2] and CMS[3], is to discover the Higgs boson(s) and the supersymmetric particles. The detectors are also optimized to detect a range of diverse signatures in order to provide guidance for future physics.

The silicon pixel system makes up the innermost part of the CMS experiment. Its main tasks are vertex detection and flavor tagging. The high rate environment at the LHC imposes stringent requirements on pixel detectors; therefore, the properties of the detectors should be extensively investigated. This thesis concentrates on studying the suitability of different test stands used to characterize pixel detectors, especially a flexible laser test stand with the provision of completely controllable source and repeatable measurements.

A brief description of the LHC physics and an overview of the CMS experiment are given in Chapter two. The following chapter is primarily concerned with the layout of the CMS pixel system and the design of the pixel detectors. Chapter four describes the pixel readout chip - the AC30 chip fabricated in the RICMOS IV-Technology, together with its readout architecture, the operation procedures and the method of data processing. Infrared absorption in semiconductor detectors is treated in Chapter five. Various absorption mechanisms are outlined and the results of the absorption measurements in Si and GaAs wafers, as well as the measurements of a GaAs Schottky diode with a 1084 nm pulsed laser diode and a GaAs strip detector with a 1064 nm pulsed Nd:YAG laser, are presented. Chapter six defines and discusses the performance parameters used to characterize a pixel

[1] Large Hadron Collider

[2] A Toroidal LHC ApparatuS

[3] Compact Muon Solenoid

detector. In this chapter two test stands are studied in detail: one employs test pulses, while the other is a laser test stand equipped with a 670 nm laser diode and a 1064 nm Nd:YAG laser. The results of the measurements of the performance parameters of the CMS Si pixel detector prototype are presented and discussed. The suitability of the test stands is then evaluated at the end of the thesis.

Chapter 2

The CMS Experiment at the LHC

This chapter is laid out in two parts. The first part investigates the physics aspects of the LHC. The Standard Model is briefly reviewed and the Higgs mechanism is introduced as the most promising explanation of spontaneous symmetry breaking in the Standard Model. After a brief discussion of the main production processes and discovery signatures of Higgs boson(s) at the LHC, the global running scenario and the experimental conditions for the CMS detector are presented in the second part, together with the layout and design goals of its detector subsystems.

2.1 The LHC Physics

The LHC will address one of the key issues of particles physics, namely the origin of spontaneous symmetry breaking in the Standard Model. Let us first review the theory.

The Standard Model describes the interactions of elementary leptons and quarks (spin-1/2 particles), mediated by spin-1 bosons. These elementary fermions are classified in three generations with left handed in doublets and right handed in singlets. An overview of the three generations of fermions is given in Table 2.1; an overview of the four fundamental interactions is given in Table 2.2.

The Standard Model is embodied in a gauge field theory based on vector fields associated with the group SU(3)⊗SU(2)⊗U(1). The SU(3) gauge interactions are the strong forces associated with QCD[1], while the SU(2)⊗U(1) interactions describe the electroweak isospin and hypercharge structure of the Glashow-Weinberg-Salam model[1][2]. Since the SU(2)⊗U(1) gauge invariance of the theory leads to massless gauge bosons, it contradicts the real experimental observations.

[1]Quantum Chromo Dynamics

Helicity	Leptons			Q	T_3	Y_W
L	$\begin{pmatrix} \nu_e \\ e \end{pmatrix}_L$	$\begin{pmatrix} \nu_\mu \\ \mu \end{pmatrix}_L$	$\begin{pmatrix} \nu_\tau \\ \tau \end{pmatrix}_L$	0 -1	$+1/2$ $-1/2$	-1 -1
R	e_R	μ_R	τ_R	-1	0	-2
Helicity	**Quarks**			**Q**	**T_3**	**Y_W**
L	$\begin{pmatrix} u \\ d \end{pmatrix}_L$	$\begin{pmatrix} c \\ s \end{pmatrix}_L$	$\begin{pmatrix} t \\ b \end{pmatrix}_L$	$+2/3$ $-1/3$	$+1/2$ $-1/2$	$+1/3$ $+1/3$
R	u_R	c_R	t_R	$+2/3$	0	$+4/3$
R	d_R	s_R	b_R	-1/3	0	-2/3

Table 2.1: Elementary fermions with their electro-weak quantum numbers (electric charge Q, third component of weak isospin T_3 and weak hypercharge Y_W; these are coupled via the isospin formalism: $Q = T_3 + \frac{1}{2}Y_W$). The quarks come in three colors, which have not been indicated here.

The Higgs[3] mechanism circumvents this problem by introducing (at least) four additional degrees of freedom into the theory in the form of a doublet of complex fields. Three of these are used up to provide mass to the gauge bosons of the weak interaction (Z^o, $W^{\pm}$), while the photon remains massless. The remaining degree of freedom manifests itself as a real scalar particle, referred in this minimal version of the Standard Model as the Standard Model Higgs H^0. This model has however the so called hierarchy problem, which is theoretically solved by a supersymmetric theory. Supersymmetric theories suggest supersymmetric partners to every known boson and fermion. Such minimal supersymmetric version of the Standard Model introduces two SU(2) doubles of complex Higgs fields. As a consequence there should be five spin-zero Higgs particles, with three of them neutral and the other two a charged pair.

	strong interaction	electromagnetic interaction	weak interaction	gravitation
range	10^{-15} m	∞	$\ll 10^{-16}$ m	∞
relative strength	1	10^{-2}	10^{-14}	10^{-41}
gauge boson	gluons g	photon γ	Z^0, $W^{\pm}$	Graviton G
gauge boson spin	1	1	1	2
gauge boson mass	0	0	$m_W \simeq 81\,GeV$ $m_Z \simeq 91\,GeV$	0

Table 2.2: Four fundamental interactions together with their gauge bosons. The Standard Model doesn't deal with gravity.

The Higgs boson couples to fermions and gauge bosons with a strength proportional to their mass. But the mass of the Higgs boson itself remains undetermined by the theory. By combining the results on radiative corrections to the Standard Model of all four LEP experiments, an upper bound of 262 GeV/c^2[4][5] for the mass of the Standard Model Higgs boson H^0 was estimated at a confidence level of 95% . Both the ALEPH and L3 experiments at the LEP[2] have recently reported the observation of Higgs candidates. Based on these events the mass of the Higgs is evaluated to be 115 GeV/c^2[6]. Due to the tight schedule of the LHC project LEP has closed down before the observation could be confirmed or disproved.

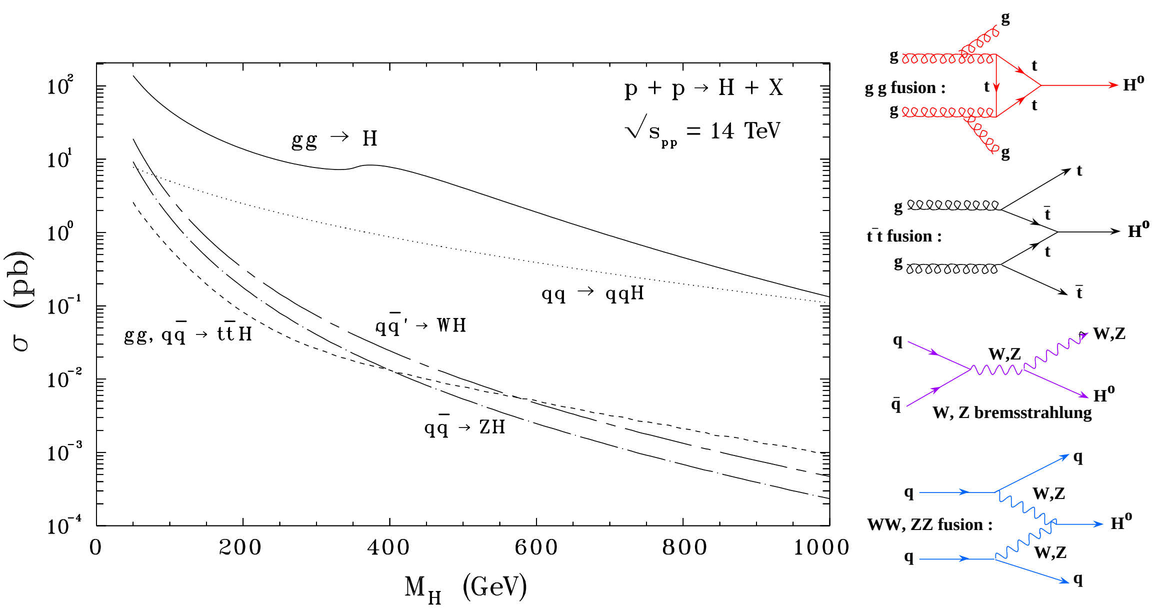

Figure 2.1: Standard Model Higgs production diagrams and corresponding cross sections at the LHC[5]. The theoretical uncertainties of cross section are about a factor 2 due to uncertainties in parton distribution functions and QCD corrections.

The prime motivation for the experiments at the LHC[7] is the search for the Higgs boson(s) and the supersymmetric particles. It is also tempting to search for a sign of new physics beyond the Standard Model. Studies show that constituent energies (i.e. the energies of the quarks, gluons which are constituents of proton) of about 1 TeV and a high luminosity are required in order to discover the new phenomena. The LHC is designed to meet these demands: it collides protons at a center-of-mass energy of $\sqrt{s}$=14 TeV every 25 ns at a luminosity from 10^{32} to 10^{34} cm^{-2}s^{-1} [8]. At this high energy the Standard Model Higgs H^0 is mainly produced via gluon-gluon fusion. In addition to the dominant cross section due to the gluon-gluon fusion, W, Z bremsstrahlung process turns out to be important at low Higgs mass. Figure 2.1 gives the production diagrams of these processes and the corresponding cross sections as functions of the Higgs mass.

The search for mass peaks in the invariant mass distribution of decay products is widely employed to discover new particles. Other methods exploit quantities

[2]Large Electron Positron collider

like the p_t spectra of leptons, photons, jets and their angular correlations, or the missing energy and momentum signature. Studies on various decay modes of the Higgs boson have been made to evaluate the experimental sensitivity for the Higgs searches[9]. Figure 2.2 shows the diagrams of the most promising discovery modes and the corresponding detectable cross sections as a function of the Higgs mass between 80 GeV and 400 GeV.

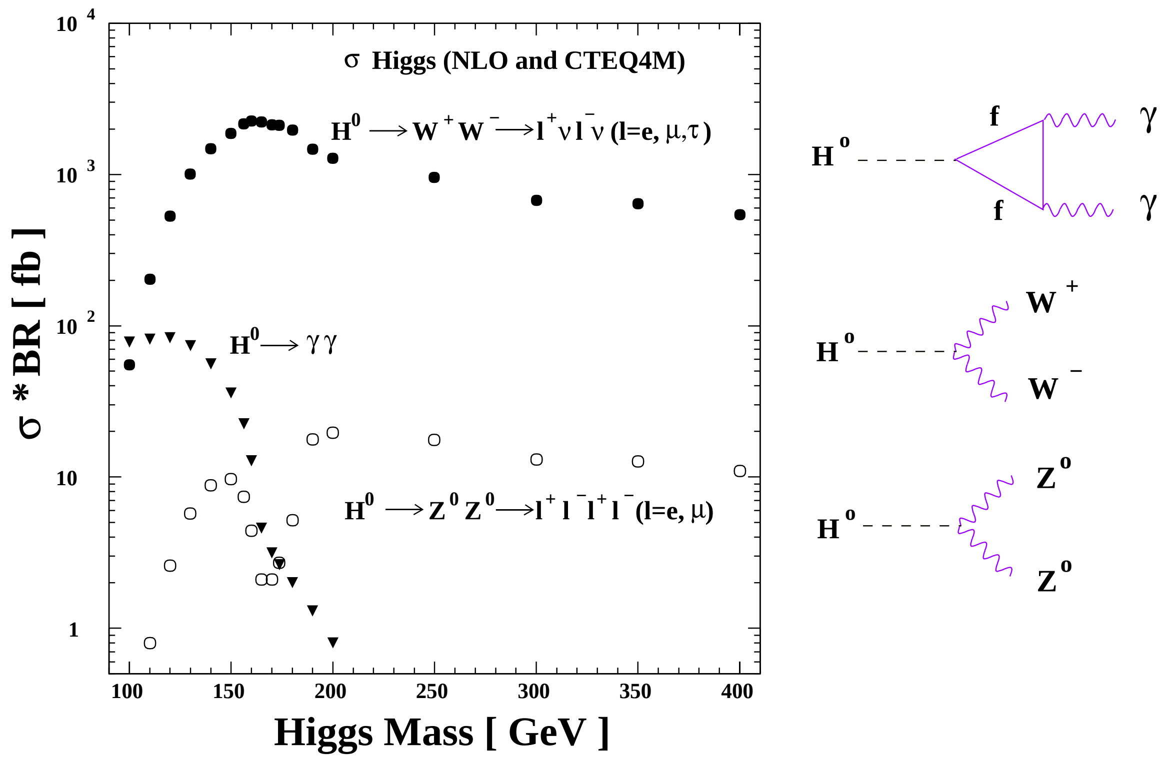

Figure 2.2: Expected detectable cross section $\sigma \cdot BR$ of the most promising discovery modes of the Standard Model Higgs at the LHC (σ is the total cross section, BR denotes branching ratio of the decay channel)[9].

For m_{H^0} in the range of 80-150 GeV, $H^0 \rightarrow \gamma\gamma$ allows a precise and direct mass reconstruction; γ-detection with high energy resolution and a large acceptance at highest luminosity is required due to the rather small detectable cross section of this decay mode. For the mass range from 140 GeV up to 500 GeV, $H^0 \rightarrow ZZ^*$, $ZZ \rightarrow 2l^+2l^-$ provides a distinctive signature. A very good muon momentum resolution, an excellent electron energy resolution and a large acceptance should be available. For Higgs mass between 140 GeV and 200 GeV, the $4l^\pm$ signature has however a very low branching ratio. Recent researches have shown that $H^0 \rightarrow W^+W^- \rightarrow l^+\nu l^-\overline{\nu}$ should do a good job to cover this mass range. The Higgs search becomes complicated for M_{H^0} ¿ 500 GeV since the natural width of Higgs boson grows and at the same time the production cross section decreases. Detection of additional signatures with neutrinos and jets from hadronic decays of W's and Z's become essential for the Higgs search in this range.

2.2 The CMS Detector

2.2.1 Global Running Scenario at the LHC

The LHC will be constructed in the 27-kilometer LEP tunnel together with the existing particle sources and pre-accelerators. Figure 2.3 shows the schematic layout of the LHC.

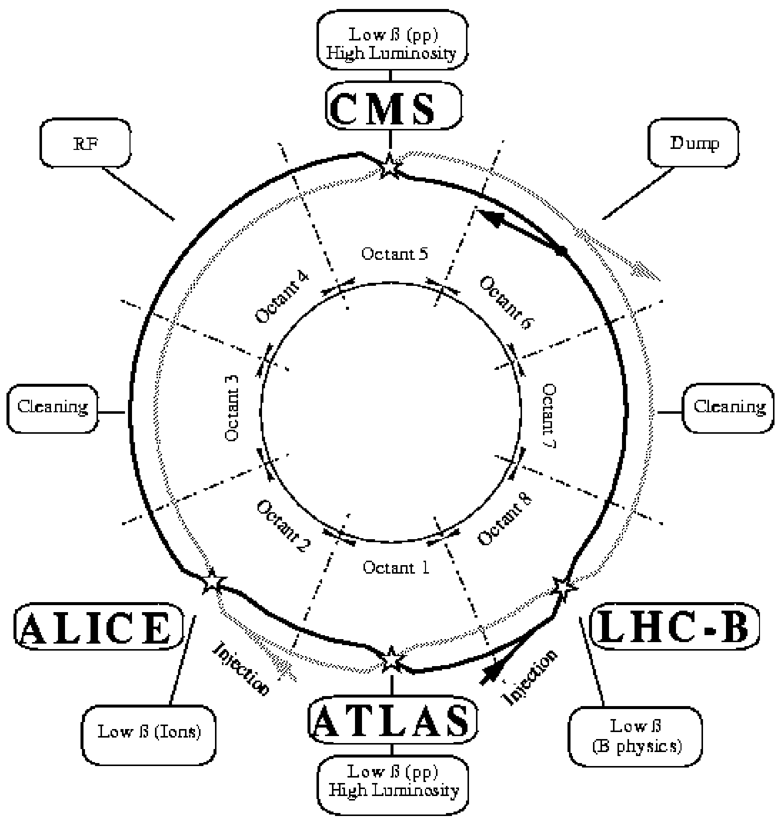

Figure 2.3: Schematic layout of the LHC.

As mentioned above, high energy proton-proton collisions will be realized at the LHC with high luminosity. In addition, heavy ions (e.g. Pb-Pb) will collide head-on at high energy densities well above the threshold for the formation of quark-gluon plasma. Four experiments are foreseen at the LHC: CMS, ATLAS, LHC-b[3] and ALICE[4].

CMS and ATLAS are two general purpose detectors aiming at excellent muon measurements and good electron/photon detection. More details of the CMS experiment will be given in the next section. The LHC-b detector is specially constructed for precision measurements of CP violation and rare decays in the B-meson system, since the LHC provides a large number of B mesons due to the

[3]Large Hadron Collider Beauty experiment
[4]A Large Ion Collider Experiment

high $b\bar{b}$ cross section and the high luminosity. ALICE will exploit the heavy ion collisions to study important issues in QCD like confinement and chiral-symmetry restoration.

It is planned to run LHC in two successive phases: the low and the high luminosity phase. The proposed luminosity profile is shown in Figure 2.4. The most important LHC parameters for the high luminosity phase are listed in Table 2.3.

The maximum luminosity at the LHC will progressively increase from 10^{32} to 10^{34} $cm^{-2}s^{-1}$ over the first one or two years. During this period single p-p interaction within the same bunch crossing is dominant; consequently the pile-up problem is not so severe as in the high luminosity phase. It is therefore advantageous in this phase to study high cross section phenomena, to study the detector performance and to prepare for higher luminosity running. In addition to the Higgs boson search, main topics of physics that can be studied with lower luminosity are heavy flavor (b and t quark) production and the physics associated with heavy flavors, anomalous gauge coupling via $W^{\pm}Z^{o}$ and $W^{\pm}\gamma$ production, jet production etc.

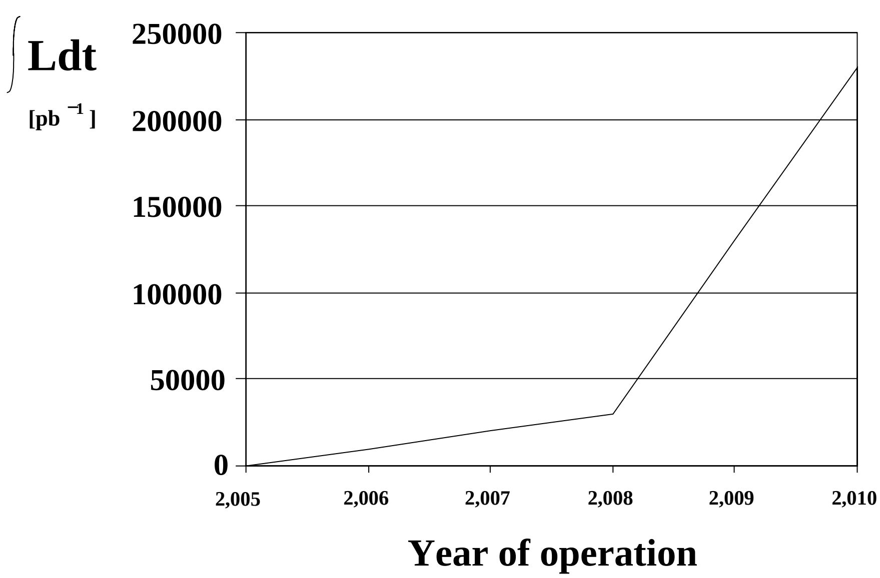

Figure 2.4: Luminosity profile of the LHC[10].

2.2.2 General Layout

As discussed above, excellent measurement of muons, electrons and photons with a large acceptance is crucial for the Higgs search. The CMS[11] detector is designed to meet these demands. Besides the search for Higgs boson(s) it is also optimized to search for supersymmetric particles as well as for hints of new physics beyond the Standard Model. Studies of t, b and τ physics are also covered in the experiment.

Energy at collision	14	TeV
Circumference	26.7	km
Crossing points	4	
Dipole field at 7 TeV	8.33	T
Luminosity	10^{34}	$cm^{-2}s^{-1}$
Luminosity lifetime	10	h
Bunch separation	24.95	ns
Bunch spacing	7.48	m
Total crossing angle	300	μrad
Number of particles per bunch	$1.1 \cdot 10^{11}$	
Energy loss per turn	6.7	keV
Total radiated power per beam	3.8	kW
Stored energy per beam	350	MJ

Table 2.3: LHC parameters[8].

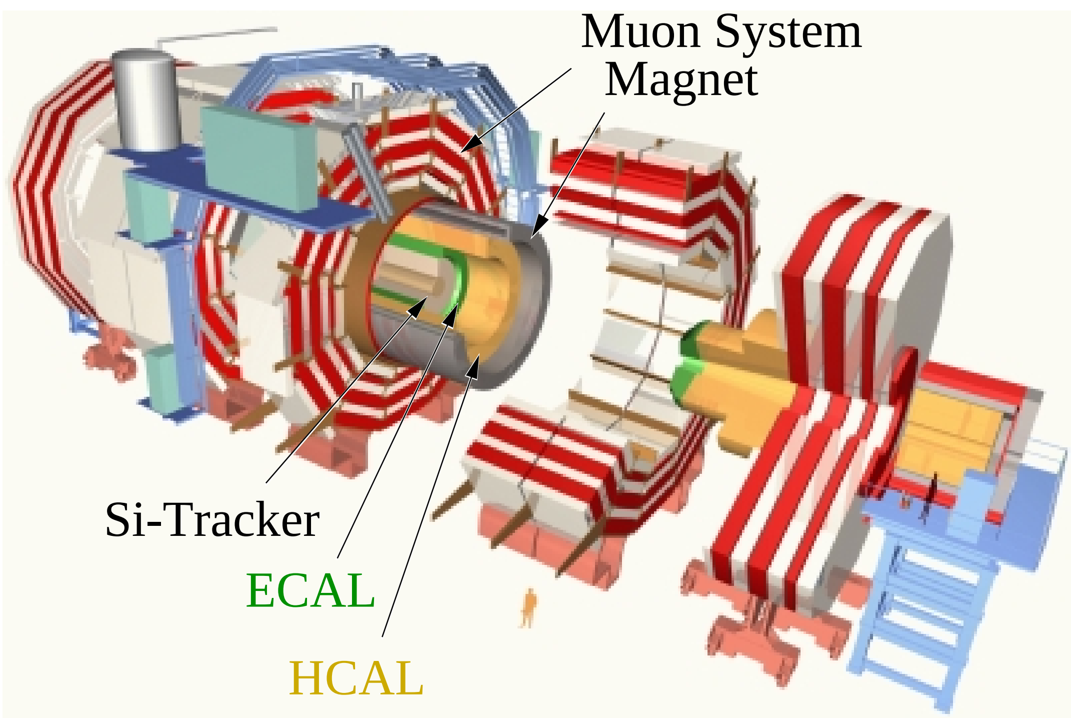

Figure 2.5: 3D Overview of the CMS detector.

The CMS detector is based on a conventional solenoidal configuration. The overall layout of the detector is illustrated in Figure 2.5. The whole system will be 21 m long and 15 m in diameter with a total weight of 12.500 t. It involves four detector subsystems, which will be described in the following:

- muon system
- HCAL[5]
- ECAL[6]
- central tracking system

A large superconducting solenoid sits at the core of the CMS detector generating a uniform magnetic field of 4 T. Tracker, ECAL and HCAL are located inside the solenoid, while the muon system is outside the solenoid. The strong magnetic field leads to good momentum resolution up to pseudorapidity values $|\eta|$[7] ¡ 2.4 and allows for a compact design of the muon system.

2.2.3 Muon System

The muon system[12] is the largest and the outermost subsystem of the CMS detector. The main tasks of the muon system are muon identification, (signed) momentum measurement and triggering. Muons provide distinctive signatures for most of the LHC physics. They are important final products of the Higgs boson decay chain. They also have the advantage of being identified inside jets without any isolation cuts; therefore muon signatures with high p_t are widely used for b-tagging. The whole muon system is embedded in the iron return yoke for the magnetic flux, covering the $\mid \eta \mid$ range from 0 to 2.5. Different technologies are employed to reach the design objectives: drift tubes in the barrel region, cathode strip chambers in the endcap region and resistive plate chambers in both the barrel and the endcap.

2.2.4 HCAL

The HCAL[13] aims for precise jet-jet mass resolution and precise missing transverse energy resolution. The expected hadronic energy resolution is $\sigma_E/E = 70\%\sqrt{E/GeV} \oplus 5\%$. Since it is essential to have a very hermetic coverage to exploit missing transverse energy signatures, the HCAL system is designed to cover the $\mid \eta \mid$ range up to 5. The pseudorapidity range ($\mid \eta \mid$ ¡ 3.0) is covered by the barrel and endcap hadron calorimeter. They are equipped with plastic-scintillators, which are inserted between copper absorber plates. In the forward direction (3.0 ¡ $\mid \eta \mid$ ¡ 5.0) an iron/quartz fiber system is proposed because of the

[5] Hadron CALorimeter

[6] Electromagnetic CALorimeter

[7] $\eta = -\ln\tan(\Theta/2)$ with Θ the scattering angle of the particle

very high radiation environment (estimated gamma radiation doses will reach 500 Mrad at $\mid \eta \mid \approx 5.0$ for an integrated luminosity of $5{\times}10^5$ pb^{-1}, neutron flux $\approx 10^8$ cm^{-2}s^{-1} at $\mid \eta \mid \approx 5.0$).

2.2.5 ECAL

The ECAL[14] is optimized to measure the two-photon decay mode $H^0 \rightarrow \gamma\gamma$, which is assumed to be the most promising signature of a light Higgs boson. It is also designed to measure electrons and positrons, which are the decay products of W's and Z's originating from Higgs decays. Due to the narrow natural width (a few MeV for $m_H = 100$ GeV) of the Higgs Boson at low masses, the Higgs mass resolution is entirely dominated by the experimental resolution. High resolution and high granularity lead tungstate ($PbWO_4$) crystals are therefore chosen as the baseline design. They have fast scintillation speed (¡25 ns), short radiation length (9 mm) and small Moliere radius (2 cm). The geometrical crystal coverage extends to $\mid \eta \mid$=3. Whereas avalanche photodiodes are used to collect the scintillation light in the barrel region, vacuum photo-triodes are proposed for the endcaps to survive a much higher integrated radiation dose (~50 kGy) and neutron fluence ($\sim 7{\times}10^{14}$ cm^{-2}). A preshower detector composed of two lead/silicon detector layers is foreseen in front of the endcap calorimeter in order to improve the π^o/γ separation.

2.2.6 Central Tracking System

As the innermost part of the CMS detector the central tracking system[15][16] is designed to provide robust tracking and detailed vertex reconstruction. It is composed of two main sub-detector elements: the silicon pixel and the silicon strip detectors. General design goals are:

- reconstruction of isolated high p_t tracks with an efficiency better than 95%
- reconstruction of high p_t tracks within jets with an efficiency better than 90%
- a momentum resolution of $\Delta p/p \sim 0.1 p_t$ (p_t in TeV) for charged particles in the rapidity range $|\eta\mid$ ¡ 2.5

The pixel and strip detectors are exposed to a high rate and consequently to a high radiation environment. Figure 2.6 shows the radiation levels (absorbed dose, fast neutron and charged hadron fluence) at selected radii in the tracker region. As a result, demanding requirements are imposed on the tracker system:

- resistance to high radiation, sufficiently signal/noise ratio during the full operational lifetime
- adequate bunch crossing identification

- pipelines on the front-end electronics which are consistent with the CMS trigger requirements (Level-1 Trigger latency ∼ 3.2 μs)
- minimized material budget to enhance the energy resolution of the ECAL and reduce the occurrence of photon conversion and bremsstrahlung of electrons

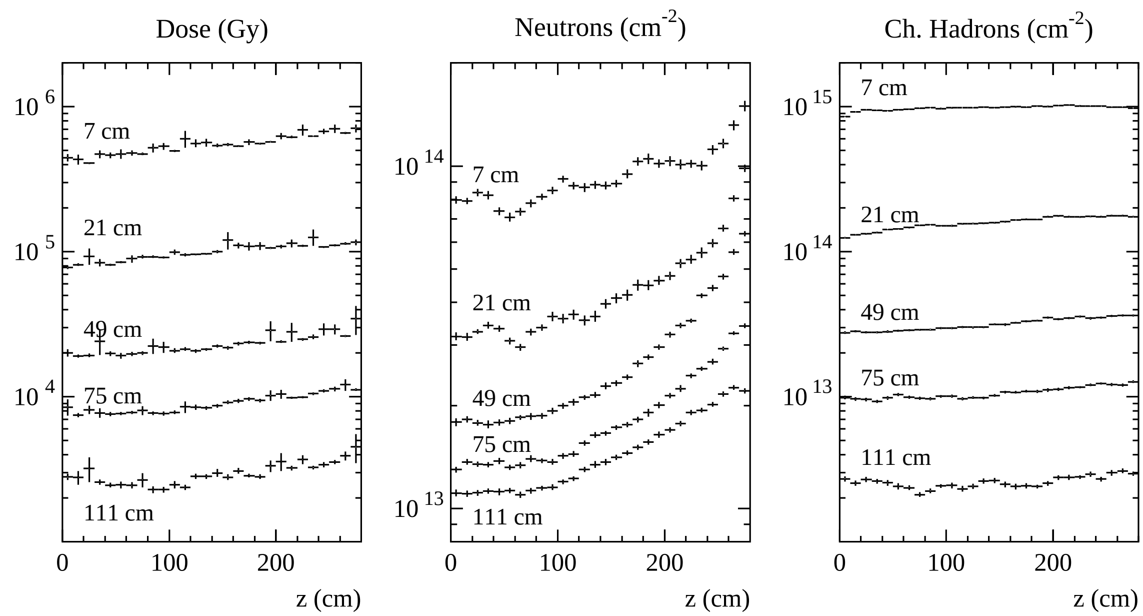

Figure 2.6: Radiation loads at selected radii in the CMS tracker, simulated at a integrated luminosity of $5{\times}10^5$ pb^{-1}. Neutron fluence only includes the part of the spectrum above 100 keV[15].

Large efforts have been invested to evaluate the overall performance of the CMS tracking detector[17]. The pixel detectors will be described in Chapter 3. Here the Si-Strip detectors will be introduced. A schematic layout of the Si-Strip system is given in Figure 2.7.

The strip detector system is constructed in four parts: TIB[8], TOB[9], TID[10] and TEC[11]. Each part is equipped with single modules and double modules. Double modules are made by two single sided detector placed back to back and rotated by a stereo angle of 100 mrad. The important parameters of the strip detector layout are given in Table 2.4.

[8]Tracker Inner Barrel
[9]Tracker Outer Barrel
[10]Tracker Inner Disks
[11]Tracker EndCap

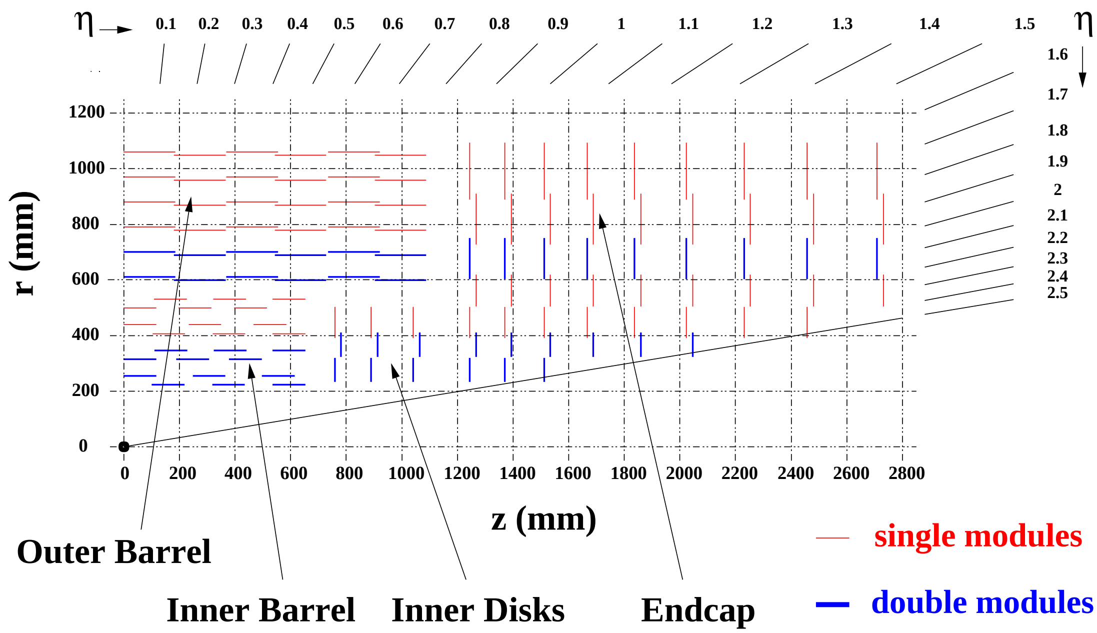

Figure 2.7: Layout of Si-Strip system (1/4 of the z-view)[18]. The system is divided into four parts: inner barrel, out barrel, inner disks and endcap.

TIB, TID and the four innermost rings of TEC are equipped with detectors of 320 μm thickness, while TOB and the three outermost rings of the TEC have detectors of 500 μm thickness. Thin detectors have one sensor made out of one 6" wafer. Thick detectors are composed of two back-to-back bonded sensors; each sensor is made out of one 6" wafer.

layout	structure	Total # of modules	Total # of APVs	active area (mm^2)
TIB	4 layers	2808	14400	62x120
TOB	6 layers	5928	29232	94x186
TID & TEC	TID: 3 small disks TEC: 9 big disks	7216	34624	

Table 2.4: Parameters of the Si-Strip detector subsystem.

The Si-Strip detectors are achievable in well established technology of strip sensors. Each sensor is AC-coupled, poly-biased, single-sided p^+ on n-bulk. Studies have shown that the Si-Strip sensors must stand high voltage operation in order to survive the high radiation environment at the LHC. For this purpose the detectors are further optimized by special processing (front face passivation, front and back-side wafer polishing, etc), by varying guard ring geometry, lattice orientation, pitch/width ratio, bulk resistivity, etc. An effective cooling system is also essential for the tracker system due to the expected 40 kW heat generated by the electronics and the detectors. To avoid thermal run-away the silicon detectors must be operated below -10^o. The cooling is also useful to reduce the bulk radiation damage.

The front-end chip, the so-called APV[12] series implemented in radiation hard technology is chosen as the baseline design of the readout electronics. It is based on a fast amplifier followed by an analog pipeline and a deconvolution circuit. Following a Level-1 Trigger analog data from the front-end chips are first time-multiplexed and then converted to analog optical signals. They are transfered to the FED boards via bundles of optical fibers. From there cluster data are determined with specialized hardware and software and then transfered to Dual-Ported Memories, where they participate the CMS general data flow.

[12] Analogue Pipeline (Voltage mode)

Chapter 3

The CMS Pixel Detector

This chapter is concerned with the design of the CMS pixel detector. The design aims, layout and data rate of the pixel system will be presented in this chapter. These will be followed by a review of the principles of a semiconductor detector. After that the baseline design of the CMS pixel detector will be introduced and discussed. The final part of the chapter gives a brief introduction of the processing of pixel detectors.

3.1 Layout and Data Rate

The pixel detector is an essential element of the central tracking system. It provides high resolution 3-D space points, which are required for:

- b-tagging as well as tagging of c quarks and τ-leptons, in order to distinguish them against a large background of light quark- and gluon jets
- pattern recognition, i.e to confirm or reject track segments proposed by the outer tracking system
- vertex reconstruction

The layout of the CMS pixel system is schematically shown in Figure 3.1. The pixel system extends from $37 \leq r \leq 210$ mm and for $-500 \leq z \leq 500$ mm (including cables and support). The system will have two barrel layers and two end disks on each side of the barrel. The two end disks are designed to complement the barrel layers so that two pixel hits can be ensured over the entire η-coverage (η=$\pm$2.4).

As mentioned before, the LHC will start running at low luminosity and proceed gradually to the high luminosity phase. The dimensions and parameters of the pixel detector for the two phases are given in Table 3.1.

The barrel layers and the disks are composed of modular detector units, each consists of a thin sensor plate segmented into 2756 pixels, which is connected via

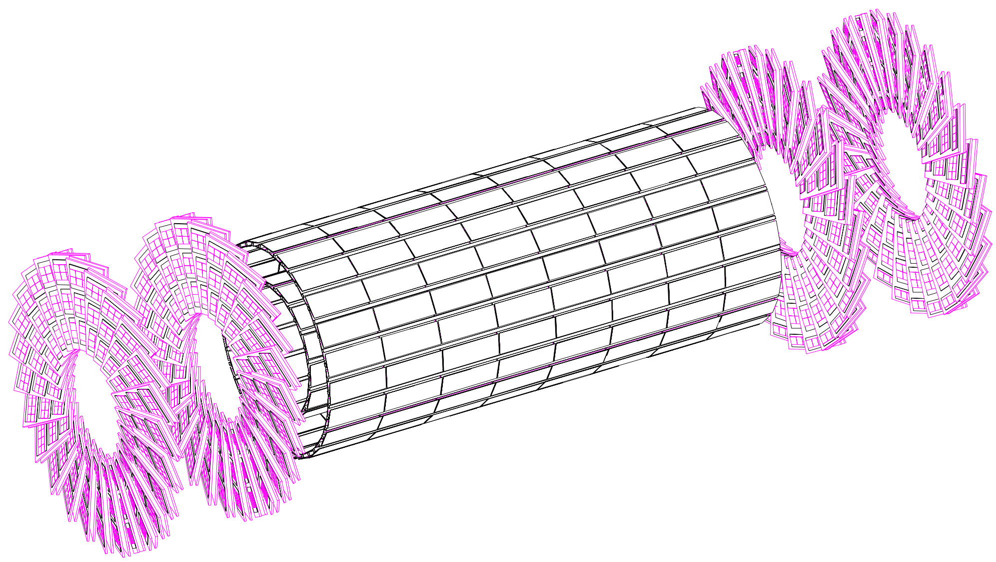

Figure 3.1: Perspective view of the pixel detector subsystem[15].

	Configuration		Radius (mm)	z (mm)	Chips	Pixels	Area (m^2)
Barrel	layer 1	low lumi	41-45	±256	2304	6.35×10^6	0.15
	layer 2	low & high lumi	70-75	±256	3840	1.06×10^7	0.25
	layer 3	high lumi	107-112	±256	5888	1.62×10^7	0.38
Endcap	disk 1,2	low & high lumi	30-150	±325	4320	6×10^6	0.14
	disk 3,4	low & high lumi	30-150	±465	4320	6×10^6	0.14
Total	low lumi				10464	2.895×10^7	0.68
	high lumi				14098	3.88×10^7	0.91

Table 3.1: Dimensions and parameters of the CMS pixel detector. The harsh environment of irradiation close to the interaction region will cause great damage to the detectors and hence limit their lifetime. When reasonable performance of layer 1 is no longer provided, this innermost layer will be removed and a new layer (layer 3) will be installed at the high luminosity phase. It is also anticipated to replace the innermost modules of the end disks once during the experiment[15].

bump bonding to a highly integrated array of readout chips (one chip/pixel). The sensors will be described in the following section.

High luminosity *pp* collisions lead to a superposition of typically 20 minimum bias events per bunch crossing, each providing hundreds of tracks in the tracker region. Out of these less than 50 tracks are interesting with p_T ¿ 1 GeV. The average data rates for the barrel is listed in Table 3.2. Assuming 3 Bytes of data per pixel, the data flow is estimated at 4 GBytes/s with a Level-1 Trigger of 100 kHz.

Radius	40	70	110	mm
Luminosity	0.1	1.0	1.0	10^{34} cm^{-2}s^{-1}
Pixel hit rate	7.6	13.0	6.9	kHz
Double column hit rate (2 x 53 pixels)	0.47	0.77	0.44	MHz
Average number of hit pixels in a hit column	1.9	1.9	1.7	
Readout chip hit rate (26 double columns)	3.3	3.5	3.6	MHz
Barrel module hit rate (16 chips)	36	40	38	MHz
Pixel occupancy	1.9	3.3	1.7	10^{-4}

Table 3.2: Average data rates for the barrel pixel (pixel size 150×150 μm^2)[15].

3.2 Baseline Design

3.2.1 Principles of Semiconductor Detectors

Before the discussion about the baseline design of the CMS pixel detector, the principles of semiconductor detectors will first be reviewed.

Figure 3.2 gives a schematic view of a semiconductor sensor. When a high energy charged particle passes through the sensor, electron-hole pairs are generated due to ionizing energy loss. These pairs are separated when an electric field is applied to the sensor, and the electrons and holes drift to the corresponding electrodes. The amount of influenced charge on the electrodes can be evaluated by Ramo's theorem and the charge pulse is sent to a charge sensitive preamplifier. Depending on the leakage current of the semiconductor detector, a DC or AC coupling between preamplifier and detector is used. The further readout chain usually consists of a shaper, a multiplexer and an ADC[1].

3.2.2 CMS Pixel Sensors

The most important consideration in the design of the pixel detector is to ensure radiation hardness of all the components and adequate bunch crossing identification at the high rate environment of the LHC. The handling of the huge number

[1]Analog to Digital Converter

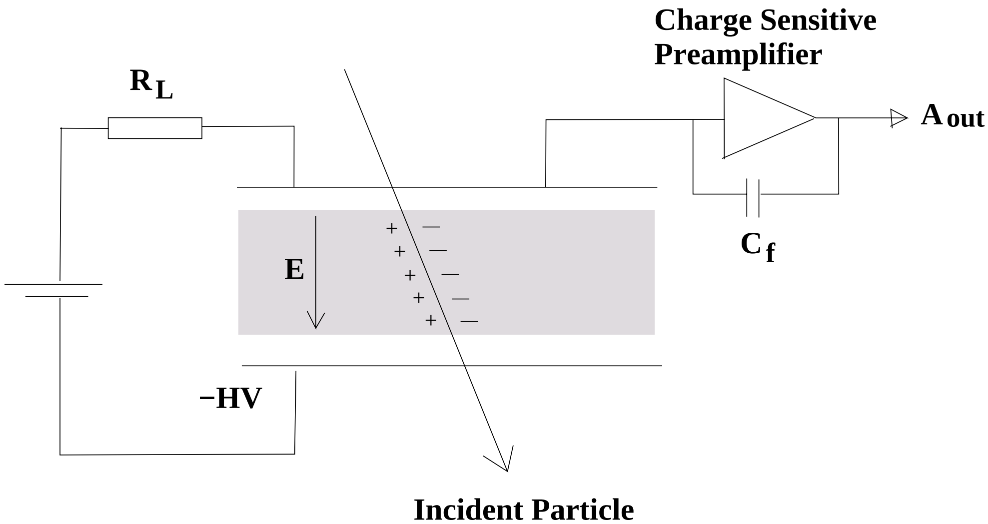

Figure 3.2: Schematic view of a semiconductor sensor with DC coupling of the preamplifier to the electrode. HV is the applied detector voltage. R_L the bias resistance, E the electric field. A_{out} is the output of the preamplifier. C_f is the feed back capacitance, which can be used to change the shaping time and the amplifying factor of the preamplifier.

of pixels also imposes a great challenge for the design. To implement the sensors the following points must be taken into account:

- detector material
- detector shape and size
- bonding technique

Detailed irradiation studies show that Si is a viable detector material, provided that the detector is sufficiently cooled down and other protective measures are taken, like front face passivation, guard ring, etc. Therefore Si has been chosen as the baseline sensor material. n-side readout is required because the detector is anticipated to undergo type inversion in a short time after being taking into operation. Another reason to choose the n-side readout is the different Lorenz angle of electrons and holes. In the barrel region the detectors are deliberately not tilted so that the effect of charge sharing induced by the Lorenz shift in the magnetic field is used to enhance the spatial resolution. The drift angle for electrons is estimated to be 32^o in a B-field of 4 T, which is three times larger than that of holes. n-pixels which collect the electrons are thus favored. A schematic view of the pixel sensor operating after type inversion is shown in Figure 3.3.

A square pixel shape is proposed in order to optimize the resolutions in both coordinates simultaneously and to give the smallest pixel capacitance to minimize detector noise. The pixel size is principally determined by the required occupancy. The originally proposed size of $(125\ \mu m)^2$ is now enlarged to $(150\ \mu\text{m})^2$

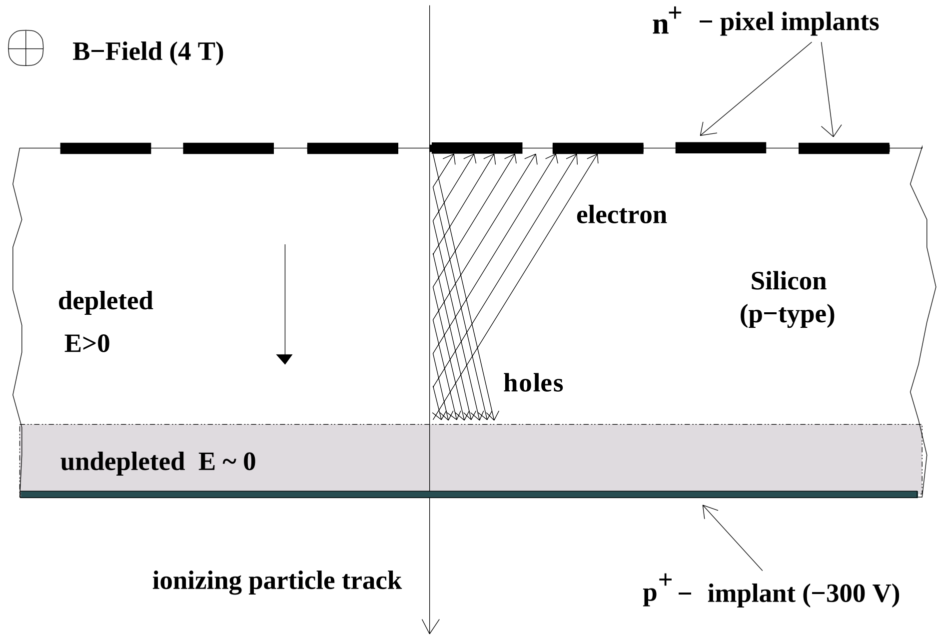

Figure 3.3: Schematic view of the CMS pixel detector in the barrel region after type inversion. Charge sharing induced by Lorenz drift in the magnetic field is used to enhance the spatial resolution[15].

to accommodate more electronics. The corresponding occupancy (see Table 3.2) is proved to be acceptable.

Since two-dimensional interconnections are required to bond readout chip and pixel sensor together, standard methods like wire bonding cannot be used here, bump bonding is instead adopted for the processing of pixel detectors. Figure 3.4 gives a schematic view of such a pixel detector. The technique will be explained after a brief discussion of the pixel readout chip.

3.2.3 Pixel Readout Chip

The primary tasks of the pixel readout chip are hit detection, signal processing (amplifying, shaping, transferring), data buffering and time-stamping. All the components of the chip must be radiation hard. An analog readout is required to improve the spatial resolution of the pixel detectors.

The total dissipated power for the analog block should be limited to less than 50 μW/pixel due to the compact dimension of the system. The choice of silicon implies typical leakage currents of 10 nA per pixel, however, the leakage currents are expected to rise after irradiation. Considering the DC connected readout scheme, the preamplifier circuit is required to absorb the sensor leakage current up to 100 nA per pixel.

A low noise performance with high signal-to-noise ratio is vital for a robust hit discrimination. The noise of about 500 e^- should not be exceeded during the

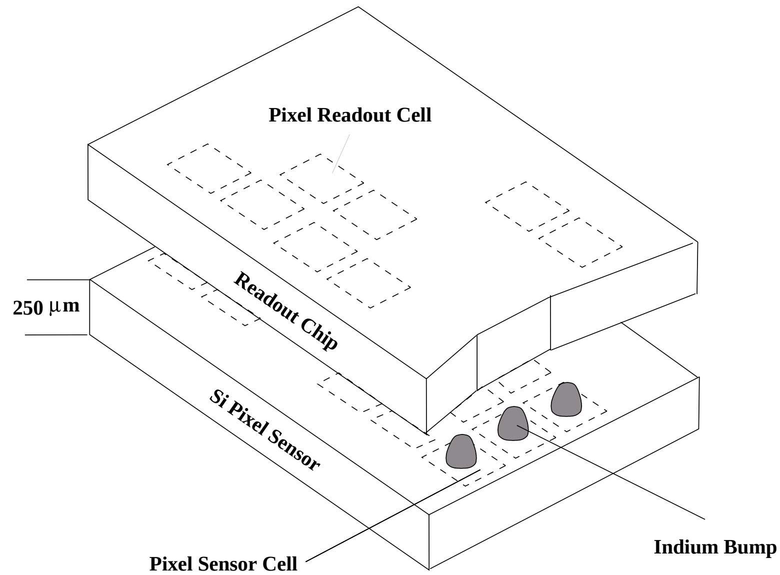

Figure 3.4: Schematic view of a pixel detector.

whole operation at the LHC. A comparator for each pixel cell is needed to detect single pixel hits. Since charge sharing is used to enhance the spatial resolution of the detector, the detection of small signals with less than 20% of the total deposited charge ($\sim 2.0\times10^4\ e^-$ in 250 μm thick Si for a MIP[2]) is required. The comparator threshold should therefore be less than 4000 e^-. Since pixel-to-pixel variations are expected to be more severe with increasing irradiation levels, an individual adjustment of the threshold is demanded for the chip.

Time-stamping is essential for CMS trigger identification. The following requirements are imposed on the front-end electronics regarding the trigger identification:

- peaking time should be less than the bunch crossing time of 25 ns.
- time walk, defined as the time difference of the comparator response for large and small input charge signals, should be minimized (see Section 6.2.5).

An implementation of the pixel readout chip in RICMOS IV-technology will be discussed in Chapter 4.

3.3 Processing of Si Pixel Detectors

3.3.1 Si Pixel Sensor

The backside of the sensor is p^+ implanted with appropriate metalization, followed by a thick passivation. On the readout side, n^+-implants in pixel shape are fabricated. They are covered by metalization and a passivation layer, but left

[2]Minimum Ionizing Particle

with a bump pad window of about 13 μm in diameter. In order to reduce the capacitance to the nearest-neighbor which dominates the total pixel capacitance, two concentric p-stop rings are implemented around the n-implant of each pixel. A guard ring is foreseen all around the pixel array to ensure the operation at a detector voltage as high as 300 V.

The pixel detectors investigated in this work are based on n-type Si bulk of high resistivity. The thickness of the wafer is 250 μm, and the pixel are arranged in an array of 32×22 with a size of (125 μm)^2. This design was based on the technical proposal of CMS[11], therefore it does not correspond to the final design (an array of 52×53 pixels with a size of (150 μm)^2.

3.3.2 Bump Bonding

A demanding procedure in processing the CMS pixel detectors is the bump bonding of the sensors and the readout chips. The I. Physics Institute of the RWTH in Germany and the PSI in Switzerland have collaborated in developing the bump bonding technique successfully.

Figure 3.5 illustrates a typical bump bonding process. During the process small indium balls or hemispheres are first deposited on the bump pads of each pixel cell of the sensor and of the chip by means of evaporation and melting. The bond pads of the sensor and the readout chip are then aligned precisely before they are assembled together (the pixel sensor and the readout chip must have the same dimensions). Figure 3.6 shows a photo of an array of pixel cells after deposition and melting of the Indium. More details about bump bonding can be found in [19][20][21].

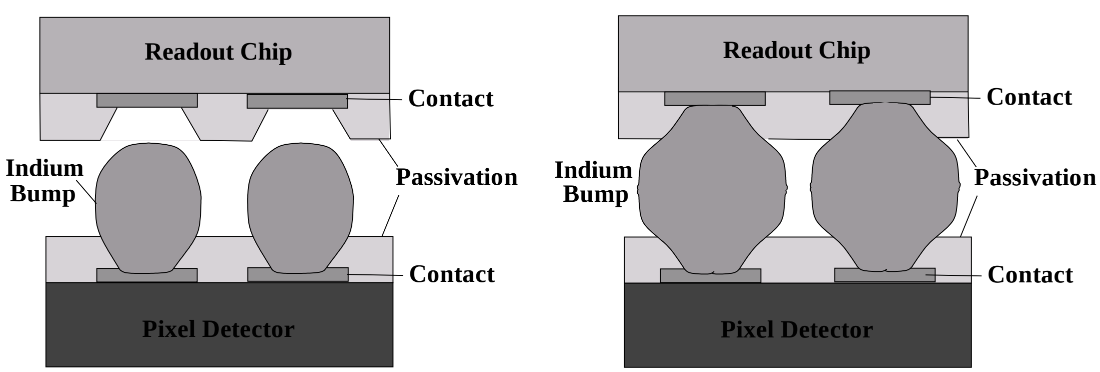

Figure 3.5: Schematic view of the bump bonding process.

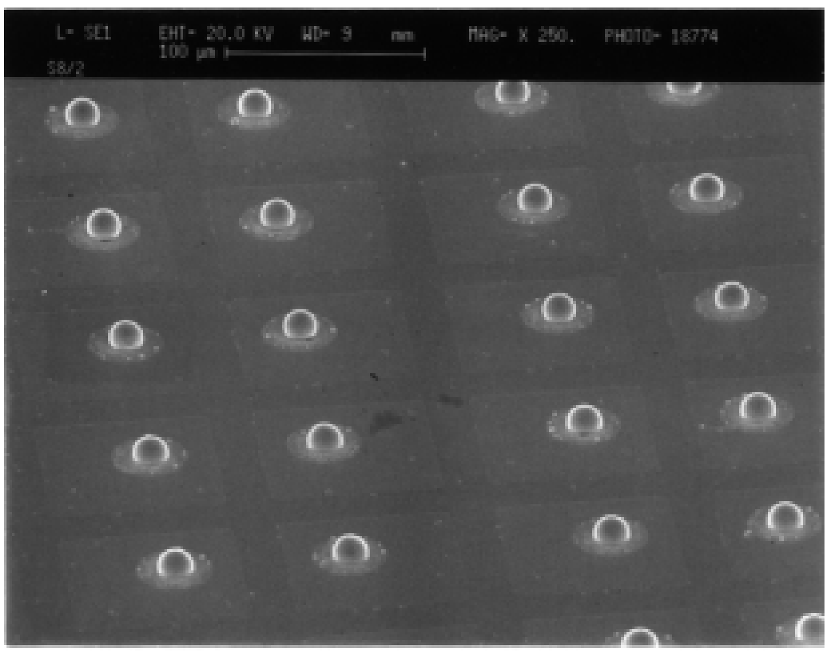

Figure 3.6: SEM photograph of an array of pixel cells after deposition and melting of the Indium.

Chapter 4

AC30 Chip

This chapter describes the readout chip for the CMS pixel detector prototype - the AC30 chip. The RICMOS IV-Technology from Honeywell, which is used to fabricate the chip, will be briefly introduced in the first part of the chapter. The following sections are concerned with the readout architecture of the chip, together with its operation conditions, i.e. the operation voltages, the pixel programming and the readout sequence. Data handling and processing will be discussed at the end of the chapter.

4.1 AC30 Chip in RICMOS IV-SOI Technology

The AC30 chip was developed by the I. physics institute of the RWTH Aachen[22][23]. It is designed to read out an array of 22x32 pixels. The whole chip has an area about 3×5 mm^2, each pixel cell has a square shape with the size of 125×125 μm^2. This design was based on the technical proposal of CMS[11], therefore it does not correspond to the final design (an array of 52×53 pixels with a size of 150×150 μm^2). Figure 4.1 shows a photograph of such a chip.

The AC30 chip is implemented in the RICMOS IV-SOI[1] technology, which was developed by Honeywell for radiation hard applications. This technology allows for the utilization of high density circuits. It also provides standard 3-layer metal or optional 4-layer metal for interconnections. In order to evaluate the applicability for the pixel detector readout NMOS and PMOS transistors were first fabricated with the technology and their DC, AC as well as noise parameters were measured. The investigations show full functionality of the transistors without any anomalous behaviors after gamma irradiation with Co^{60} up to a total dose of 55 Mrad. The technology was then employed to fabricate pixel readout chips.

The readout architecture of the chips will be described in the next section.

[1]Silicon On Insulator

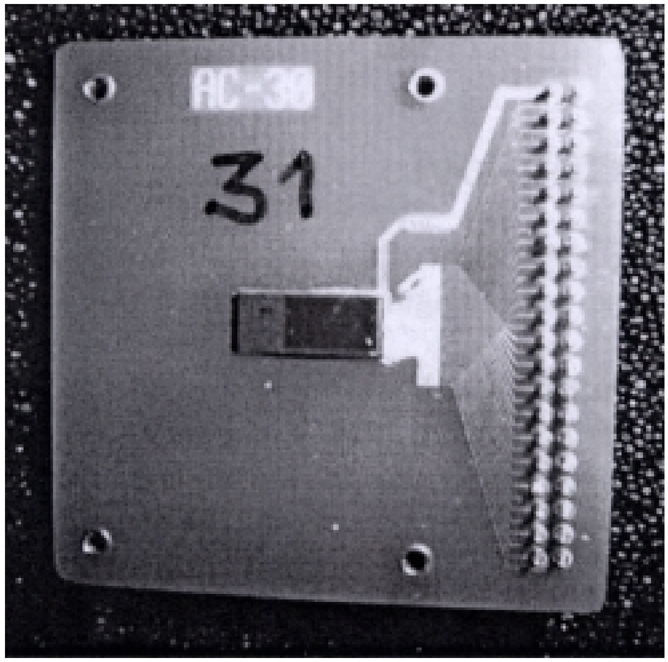

Figure 4.1: Photograph of an AC30 chip. The chip is wire bonded to a fine pitch connector.

4.2 Readout Architecture

As mentioned before, the AC30 chip consists of an array of 22x32 pixels. Each PUC[2] of the chip is DC-coupled to a detector pixel cell at the bump bonding pad. Every two PUC columns form a double column, which is the basic readout unit. In addition to the pixel cells, supplementary space at the lower part of the chip is reserved for the double column periphery and for the readout bus (see Figure 4.2). PUCs are designed for signal amplification, hit detection and temporary single hit storage, while the column periphery performs the tasks of time-stamping, multiple hit and readout buffering.

Figure 4.3 shows the signal processing chain of a PUC[24]. Each PUC is composed of an analogue and a digital block. The analogue block consists of a preamplifier, a shaper and a comparator. The main components of the digital block include a flip-flop (FF) and shift registers.

When charges are injected into the pixel detector, signal of the influence charges will be first amplified and shaped. The gain of the preamplifier as well as the time constant of the shaper can be controlled by the feedback resistors. For test purposes a calibration capacitance (CC) of 1.7 fF is implemented in each pixel cell.

The output of the shaper is transfered to the comparator and to the sampling capacitance (SC) separately. When the signal exceeds the comparator threshold,

[2]Pixel Unit Cell

a hit pulse is generated. The global threshold of an AC30 chip is controlled by the operation voltage V_{comp}.

An individual adjustment for each PUC is also implemented through a 3-bit static memory cell (SRAM) and a DAC[3] unit. The SRAM setup, i.e, the trim bits, are first programmed and then uploaded to each pixel before any data taking. All together nine configurations of trim bits are available for each PUC. Trim bits DTR=0 is reserved to switch off the comparator; therefore it can be effectively used to disable any nonfunctional pixels.

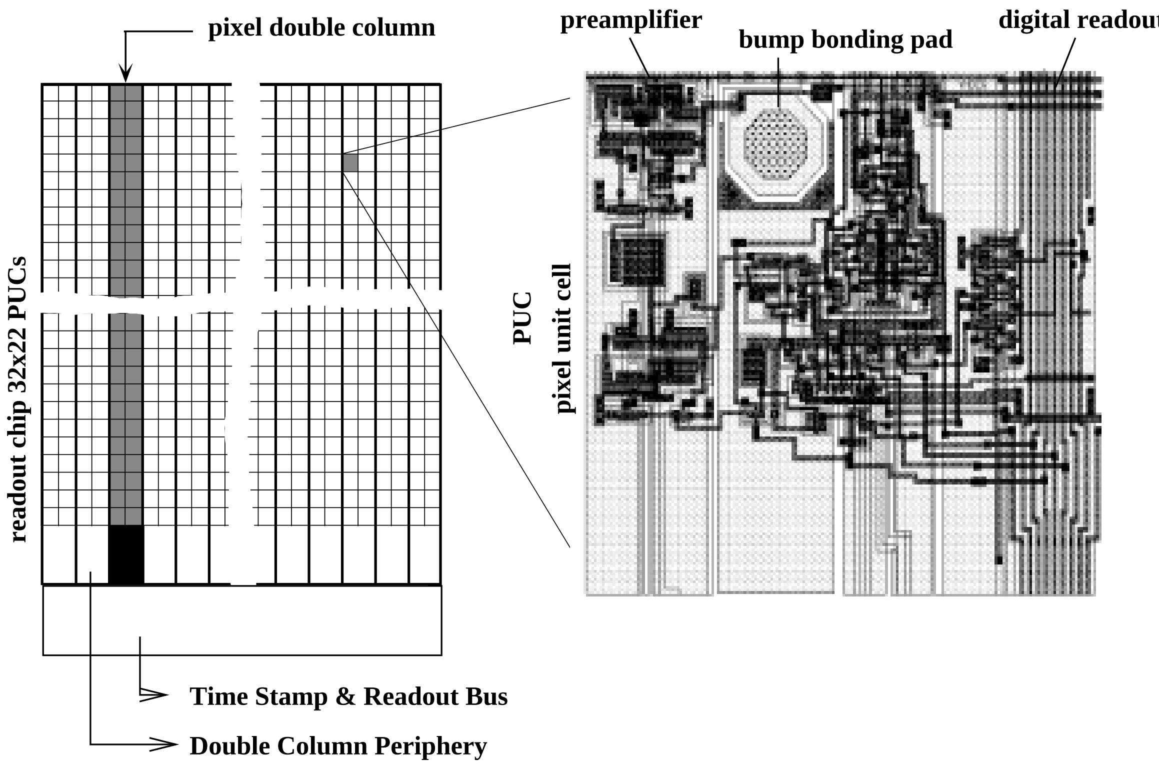

Figure 4.2: Schematic layout of the AC30 chip and its PUC. The chip is used to read out an array of 22x32 pixels.

In the regular readout mode the hit pulse from the comparator sets the hit flag of the flip-flop and the column OR signal is consequently pulled down from its original high state to ground. The column logic of the chip latches the OR signal and sends an internal $HOLD$ signal to all pixel cells in the hit double column. This $HOLD$ signal disconnects the sampling capacitance from the output of the shaper, disables the comparator, and therefore freezes the states of all the pixel cells in the double column.

[3]Digital-Analog-Converter

A read bit is then initiated from the periphery to run up and down the hit double column via a shift register. This read bit bypasses the empty pixels, while enabling the transfer of the digital and analogue signals to the data bus where the pixel is hit.

In addition to the above described regular mode an alternative readout mode, the so called full-readout mode is also implemented for test purposes. Within this mode it is possible to read out all the double columns independently of the trigger signal.

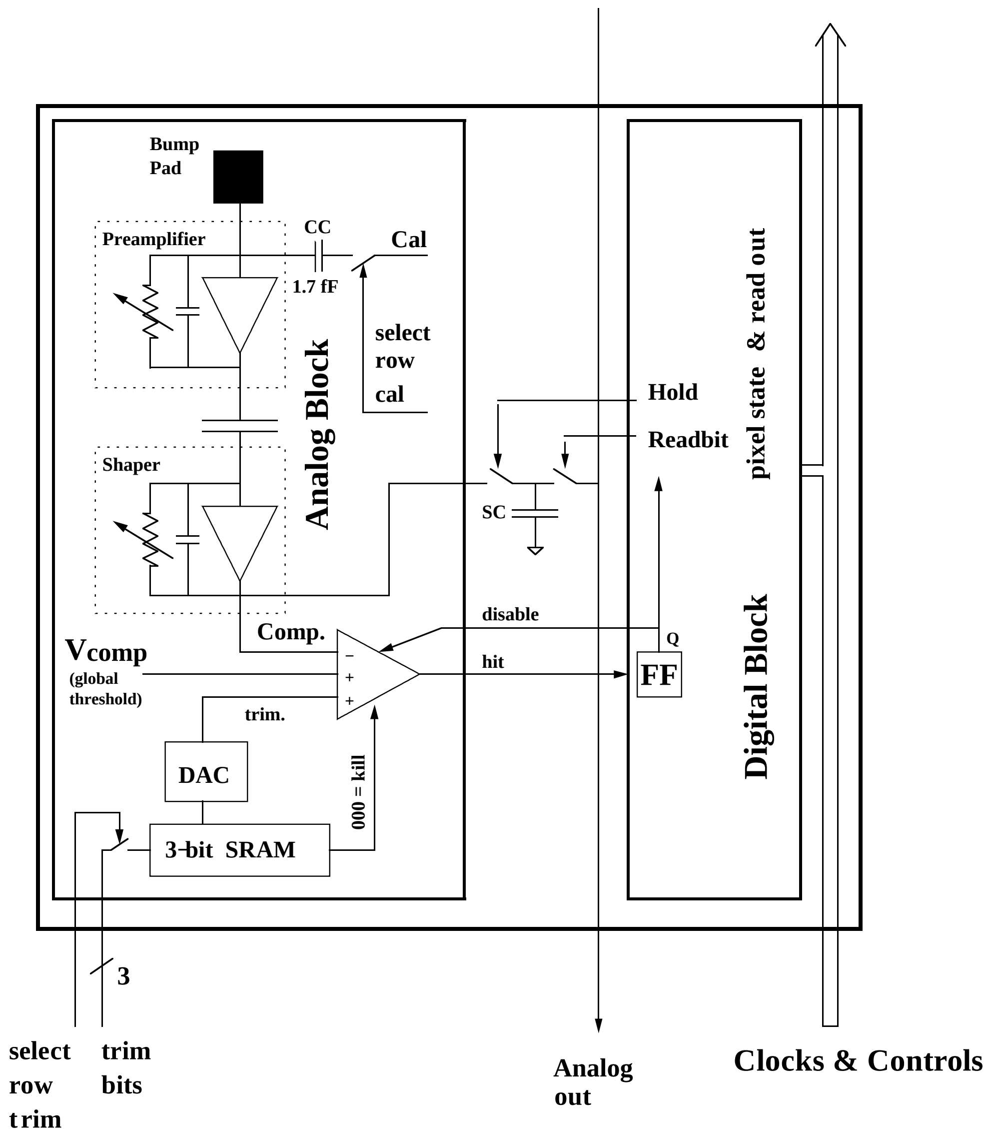

Figure 4.3: Readout chain of a PUC[24].

After reading out the chip, the flip-flop is reset and the sampling capacitance of each PUC is reconnected to the output of the shaper. The comparator is also set free for further detection. The transfered data, which include coded addresses of the hit double columns and the pixel signals, are stored in a data buffer until the arrival of the trigger decision.

At the same time when the hit flip-flop is set, the current status of a local time stamp counter is copied into the time stamp buffer of the chip. At each bunch crossing all stored time stamps are compared with the local bunch crossing number used to count the last 128 bunch crossings (i.e, 3.2 μs corresponding the latency of the Level-1 Trigger). If any coincidence is detected and if the first level trigger is available for this bunch crossing, the associated signals and addresses are transmitted directly from the double column peripheries to the front-end drivers in the counting room via the analogue optical links. In case the first level trigger is absent, the time stamp register and its associated data buffer are set free for further data taking.

4.3 Operation Voltages

The AC30 chip is supplied with various operation voltages. The main part of them and their functions are listed below:

- V_{ssana}, V_{dig}: supply voltage of the analogue and the digital part of the chip respectively
- V_{ssf}: control voltage of the source follower
- V_{rgpr}, V_{rgsh}: controlling the pulse form of the preamplifier and the shaper respectively
- V_{comp}: controlling the global comparator threshold
- V_{trim}: controlling the range of the individual adjustment of the comparator threshold for each pixel cell
- V_{bro}: controlling the baseline level of the analogue output A_{out}
- V_{hld}: controlling the delay time of the internal $HOLD$ signal

operation voltage	value (mV)	operation voltage	value (mV)
V_{ssana}	-1966	V_{ssf}	-3434
V_{dig}	-5000	V_{trim}	-984
V_{rgpr}	-2289	V_{bro}	-3795
V_{rgsh}	-3611	V_{hld}	0

Table 4.1: Standard values of the main operation voltages of the AC30 chip.

The standard values of these operation voltages are determined after careful studies of the performance of the detector[25]. They are listed in Table 4.1. All the operation voltages have a negative value. The adjustment of V_{comp} will be described in Chapter 6. In a regular readout mode V_{hld} is set to zero; for the measurements of pulse form, however, V_{hld} should be set to -5 V in order to access the external $HOLD$ signal, while switching off the internal $HOLD$ signal.

4.4 Chip Programming

Before taken into operation, the chip must be configured in order to:

- adjust the comparator threshold globally and individually
- switch off nonfunctional pixels
- set to readout mode and select pixel cells to access test pulses if a calibration process is followed

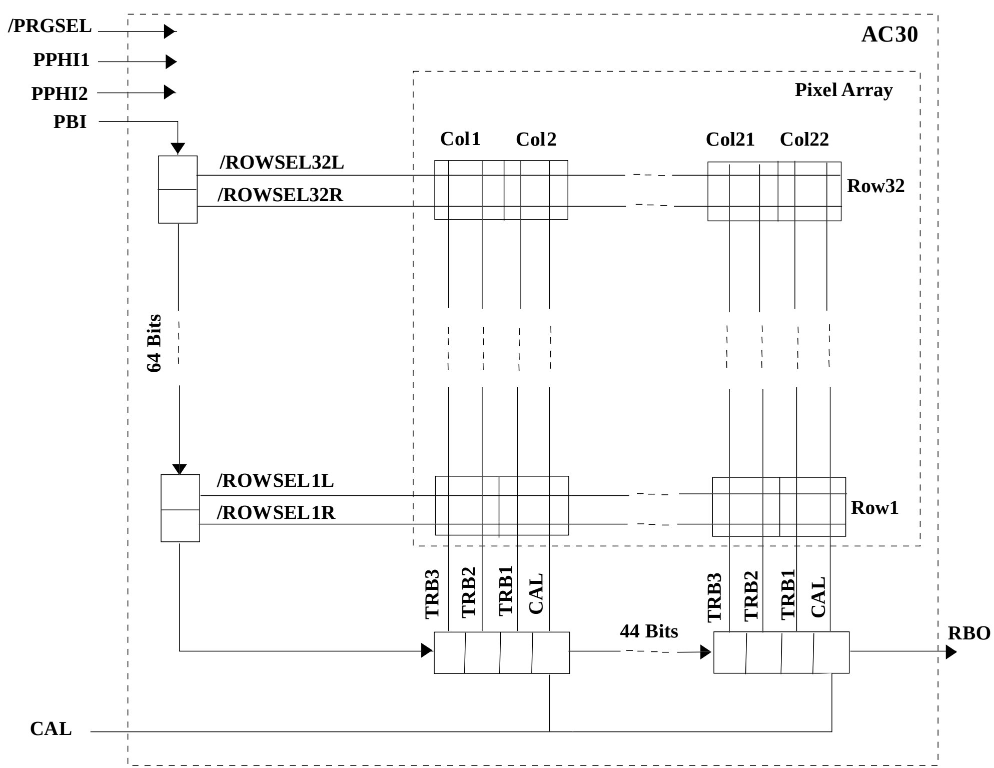

Figure 4.4: Schematic view of the programming sequence of the AC30 chip. A 108-bit shift register is implemented to configure an array of 22x32 pixel cells.

A 108-bit shift register is employed for the pixel programming. Four slow digital control signals are necessary for the procedure:

- $PPHI1$: the first stroke of the shift register

- $PPHI2$: the second stroke of the shift register
- PBI: programming data in a 108-bit sequence
- $PROGSEL$: stroke to initiate the uploading of the trim bits

Figure 4.4 shows the pixel programming sequence of the AC30 chip. The first 44 bits of PBI are used for the 11 double columns with four bits for each unit: Cal=1(0) to disable(enable) test pulses, $TRB1$, $TRB2$ and $TRB3$ are the trim bits, which are used to set the individual threshold of each PUC.

The following 64 bits are called $ROWSEL$: There are two PBI bits for each of the 32 rows; one referring to the right side of the double column and the other referring to the left side of it.

$PROGSEL$ comes at the end of the sequence. When $PROGSEL$ is active, i.e in a low state, the trim bits will be assigned to the pixel cells, otherwise the input of the trim bits will have no effect, only the bits of Cal will be effectively uploaded.

4.5 Readout Sequence

To read out the AC30 chip another shift register is implemented. Three fast digital control signals are necessary at this point:

- $PHI1$, the first stroke of the shift register
- $PHI2$, the second stroke of the shift register
- RBI, stroke to initiate readout

Provided that the three signals are given in the right order, the readout procedure runs automatically and independently of the pixel programming. Figure 4.5 shows the schema of the readout procedure in the regular readout mode.

Each pixel cell has a 1-bit buffer processing the read bit(RBI/RBO). When RBI=1, the digital and analogue outputs of each PUC will be transmitted to the data bus. Each double column holds additionally four one-bit buffers controlled by the read bit. The first three bits enable the transfer of the time stamp coded in an analogue form and the last bit enables the transfer of the column number, which is also coded in an analogue form (different voltage level corresponds to different double column number).

Each double column is daisy chained to the adjacent double column. When the read bit RBI is sent from the periphery, it goes up and down the double columns which are hit, skipping those that are not hit. In the full-readout mode, however, all double columns are forced to be free for the read bit, so that the whole chip can be readout by applying enough tokens of $PHI1$ and $PHI2$.

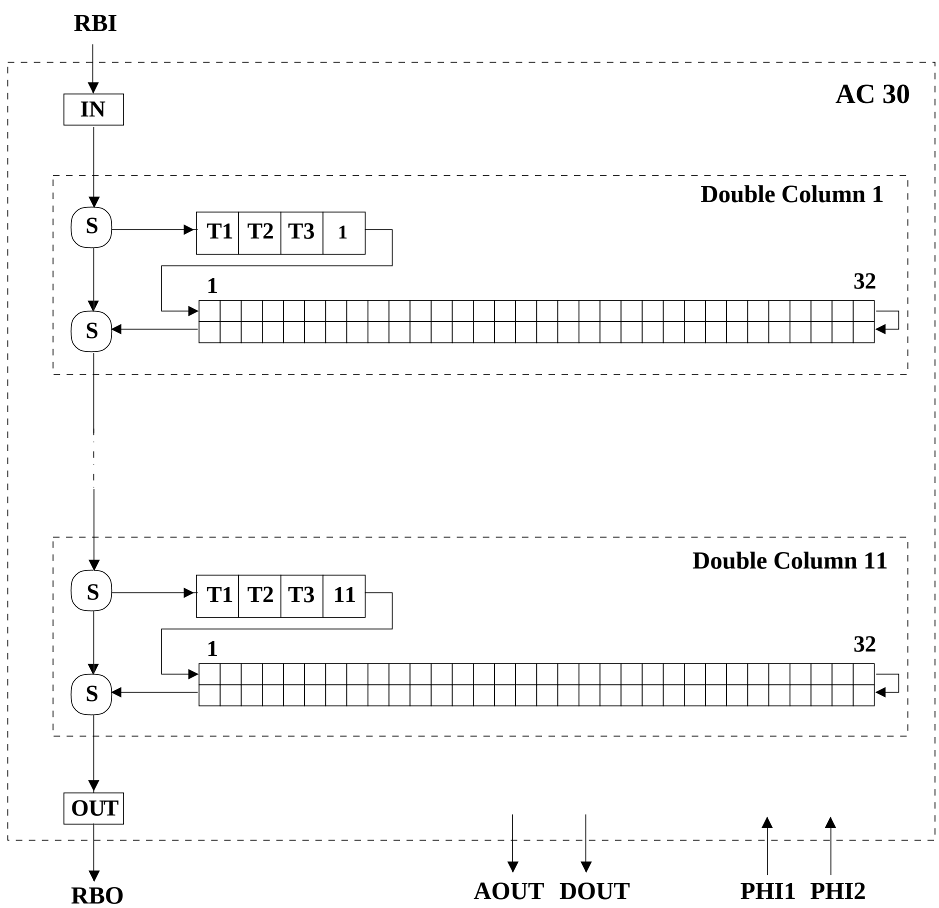

Figure 4.5: Schematic view of the readout sequence of the AC30 chip.

4.6 Data Handling and Processing

The analogue signal A_{out} as the output of the shaper for each PUC should be evaluated by subtracting its pedestal from raw data. The pedestals can be acquired by an independent run for about 500 events without any charge injection. In order to calculate the pedestals and noise levels correctly, the effect of baseline shift from event to event should also be taken into account. In the following discussion I will show that there are two contributions to this effect:

- one that affects each double column in the same way, which is caused by a variation of the operation voltages within a small range. This kind of shift is denoted as common mode (CM).
- one that affects only the double columns which are hit. This kind of shift is denoted as BS.

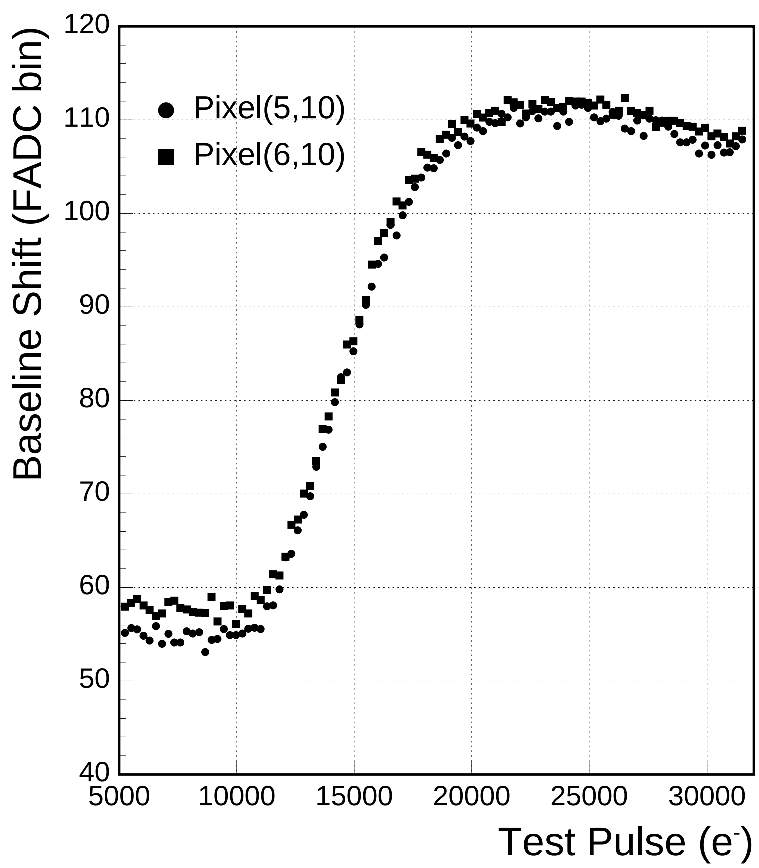

Figure 4.6: Measurements of baseline shift of the hit double column 5 and 6. Pedestal and CM are taken into account in the data analysis. Pixel(5,10) and pixel(6,10) are the pixels which are not hit.

BS has been found to be mainly dependent on the signal height of the hit pixel(s). Figure 4.6 demonstrates this effect. In the two measurements the test pulses are sent to pixel(5,20) and pixel(6,20) respectively. The other pixels are not allowed to access the input charges.

The baselines of double columns 5 and 6 are evaluated as the corrected data of pixel(5,10) and pixel(6,10) respectively, which are not hit. It can be seen that the level of the baseline changes as the amplitude of the test pulse varies. It is stable with the small input charges, but begins to rise with the increasing test pulse height. When the input charges exceed 20000 e^-, the shift of the baseline reaches its maximum. After the stage of saturation, it finally declines a little when the test pulse height is above 25000 e^-. The shift of the two double columns follows the same pattern; the result is consistent with the consideration of CM.

Other measurements show that the number of hit pixels can also have an influence on the baseline shift. This effect is considerable for the DMILL chips[25], but for the AC30 chips it plays only a minor role.

To sum up, raw signals have to be processed in the following way:

1. For a pedestal run with n events (typically 500) without any charge input:

   (a) The common mode CM of each double column i, can be expressed as:

   $$CM_{ei} = \tfrac{1}{m}\sum_{j=1}^{64} A_{eij} \cdot c_{ij} \tag{4.1}$$

   with:

   $$c_{ij} = \begin{cases} 0 & \text{noisy pixel} \\ 1 & \text{else} \end{cases}, \qquad m = \sum_{j=1}^{64} c_{ij} \tag{4.2}$$

   A_{eij} is the raw data of analog signal A_{out} of each pixel for each event. e denotes the event number, i is the number of the double column (i=1..11) and j is the pixel number in that double column (j=1..64, the total number of a double column is 64). Noisy pixels are those pixels which have the trim bits DTR=0. Since the common mode is identical for all the pixels, CM_e is calculated only with one double column, e.g. double column 2.

   (b) The pedestal P_{ij} for each functional pixel is determined as:

   $$P_{ij} = \frac{1}{n}\sum_{e=1}^{n}(\, A_{eij} - CM_e \,) \tag{4.3}$$

   (c) Finally the noise N_{ij} is calculated by:

   $$N_{ij} = \sqrt{\frac{1}{n}\sum_{e=1}^{n}(A_{eij} - P_{ij} - CM_e)^2} \tag{4.4}$$

(d) In order to decide which pixel is hit when charge is injected, the pedestal d_{ij} of digital output D_{out} for each pixel (i.e, the output of the comparator) has to be calculated at this step with the following equation:

$$d_{ij} = \frac{1}{n} \sum_{e=1}^{n} D_{eij}$$

where D_{eij} is the raw data of D_{out} read out by an FADC for event e.

2. For a data run of N events with test pulse or laser pulse injection:

(a) The mean signal level D_{ij} of D_{out} for each pixel is:

$$D_{ij} = \frac{1}{N} \sum_{e=1}^{N} D_{eij}$$

so that the pixel is determined to be hit if $\mid D_{ij} - d_{ij} \mid$ ¿ 200 FADC bins.

(b) The common mode CM_e will be again evaluated after the above discussed procedure. The selected double column for the calculation of CM has to exclude any hit pixels.

(c) The baseline shift BS_{ei} for a hit double column i is determined as:

$$BS_{ei} \quad = \quad \tfrac{1}{l} \textstyle\sum_{j=1}^{64} (A_{eij} - P_{ij} - CM_e) \cdot c_{ij} \tag{4.5}$$

with:

$$c_{ij} = \begin{cases} 0 & \text{noisy/hit pixel} \\ 1 & \text{else} \end{cases} , \qquad l = \sum_{j=1}^{64} c_{ij} \tag{4.6}$$

(d) It is only interesting to calculate the analogue signals for those hit columns of event e. They are calculated by subtracting the pedestal and the baseline shift from the raw data:

$$S_{eij} = A_{eij} - P_{ij} - CM_e - BS_{ei} \tag{4.7}$$

(e) The signal is finally analyzed as the average value over all events:

$$S_{ij} = \frac{1}{N} \sum_{e=1}^{N} S_{eij} \tag{4.8}$$

(f) The signal-to-noise ratio is therefore:

$$SN_{ij} = \frac{S_{ij}}{N_{ij}} \tag{4.9}$$

4.7 Summary

The AC30 chip has been developed to read out the CMS pixel detector prototype in analogue mode. The main implemented functions of the chip are hit detection and signal processing (amplifying, shaping and transferring).

The AC30 chip has to be applied with various supply and control voltages. Their values have been determined after careful studied on the performance of the chip. The comparator thresholds of the chip should be configured globally and individually; any nonfunctional pixel cells have to be switched off and the chip should be set to readout mode before any data taking. In case of a calibration process, pixel cell(s) should be first selected to access test pulses.

For the data analysis of the AC30 chip both pedestal and baseline shift of each pixel have to been taken into account. I have demonstrated that two effects contribute to the baseline shift: one is the so called common mode (CM), which is caused by a variation of the operation voltages within a small range and affects each double column in the same way; the other one, denoted as BS, affects only those double columns which include any hit pixels. BS is mainly influenced by the amplitude of the input charges. As the consequence the signals have to be calculated by subtracting the pedestal, the CM and the BS from the raw data.

Chapter 5

Infrared Absorption in Si and GaAs

Normally we use test pulses, radioactive sources and radiation sources from particle accelerators to study a tracker detector. Until recently various test stands for the evaluation of Si-strip detectors were reported to be equipped with pulsed lasers[26]. The main benefit of using a laser system is to have a completely controllable source and high statistics for the laboratory use.

In order to study the suitability of such a laser system to characterize the pixel detectors, the light absorption in Si will be treated in this chapter. Since GaAs was a candidate for the CMS pixel detector material, the properties of GaAs will also be discussed and a comparison between the two materials will be made. Main parameters of Si and GaAs will be reviewed in the first part of the chapter. Dominant processes of infrared absorption will be then discussed in the following sections, together with the results from the measurements of transmission and absorption in both materials. Finally the measurements on a GaAs diode and strip detector with laser pulses will be presented .

5.1 Properties of Si and GaAs

Before we consider the photon absorption mechanisms of Si and GaAs, the main properties of the two materials will be briefly reviewed (see Table 5.1).

Photon absorption in Si and GaAs is mainly dependent on the band structure of the material. Figure 5.1 shows the energy band diagram of defect free un-doped Si and GaAs. Unlike Si, GaAs is a direct semiconductor, by which the maximum of the valence band and the absolute minimum of the conduction band are found at the same value of the wave vector (Γ point). The band gap energy E_g, i.e., the energy difference between the lowest conducting band and the highest valence band, is 1.12 eV for Si and 1.42 eV for GaAs respectively.

In pure and defect free semiconductor no states can exist in the forbidden energy region. Commercially available Si and GaAs wafers however contain a certain

	Si	GaAs	
Crystal structure	Diamond	Zinc blende	
Band structure	indirect	direct	
Atomic number	14	31/33	
Density	2.33	5.32	$\frac{g}{cm^3}$
Dielectric constant ϵ	11.9	13.1	
Band gap energy E_g	1.12	1.42	eV
Intrinsic carrier density	1.45×10^{10}	1.79×10^{10}	cm^{-3}
Specific most probable ionization energy loss for MIPs	0.28	0.57	keV/μm

Table 5.1: Physical properties of Si and GaAs at 300 K[27].

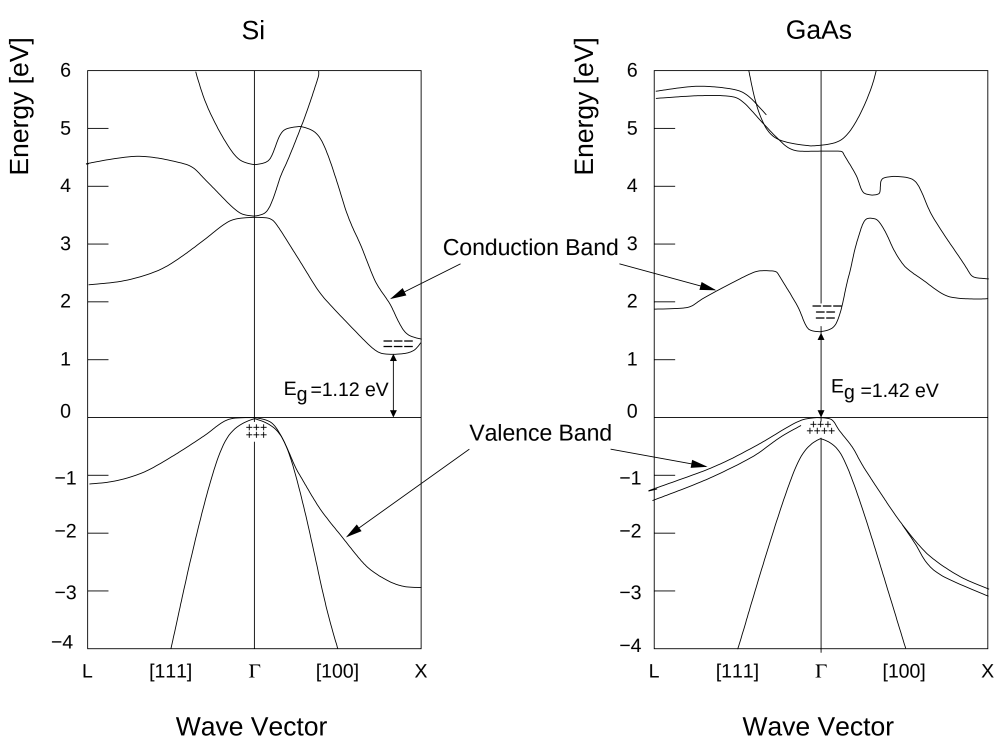

Figure 5.1: Energy band diagram of Si and GaAs.

amount of impurities and defects, which create shallow and deep levels in the forbidden gap. As we shall see later, these energy levels could have considerable influence on photon absorption.

5.2 Introduction of Absorption Coefficient

Absorption is characterized with the absorption coefficient α, which is defined as the relative rate decrease of the light intensity L along its propagation path:

$$\alpha = \frac{1}{L}\frac{dL}{dx} \tag{5.1}$$

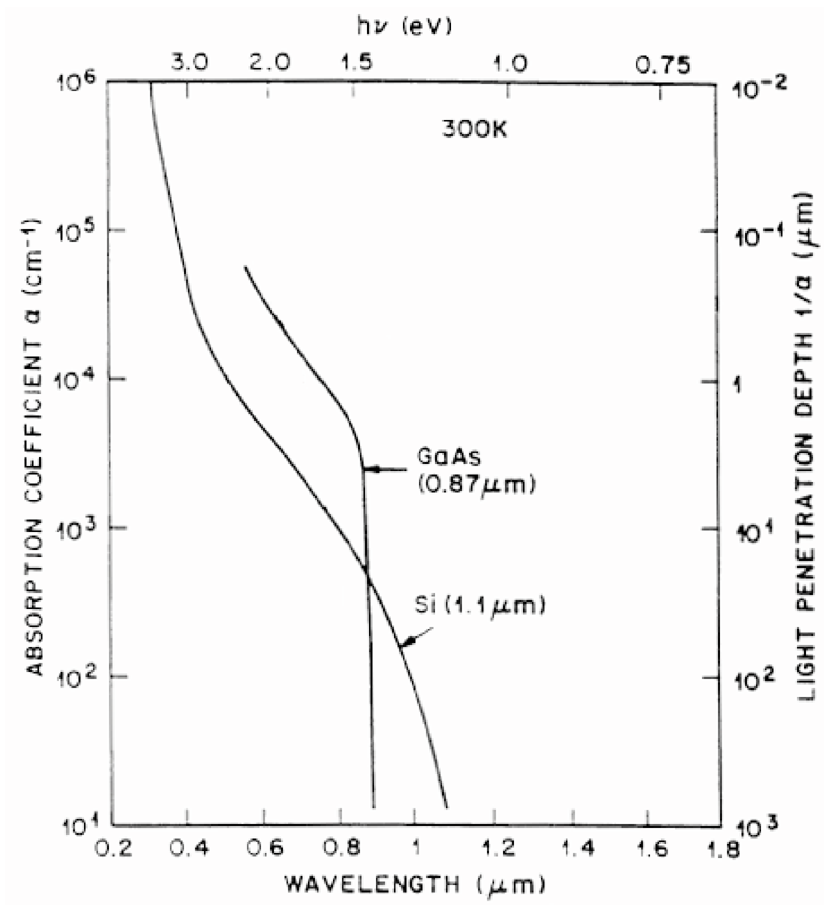

Figure 5.2: Absorption coefficient α and light penetration depth ($d = 1/\alpha$) of Si and GaAs as a function of wavelength and photon energy[28].

Figure 5.2 shows the absorption coefficient α of Si and GaAs as a function of wavelength and photon energy. It can be seen that up to a wavelength of 1100(900) nm the absorption coefficient in Si(GaAs) decreases with the increasing wavelength. α of GaAs drops sharply near the band gap, i.e. at a wavelength λ_g of 875 nm. The drop of α in Si is relatively smooth; the band gap energy E_g of Si corresponds to a wavelength λ_g of 1100 nm. Since both wavelengths are in the infrared region, I will focus on the infrared absorption in the following discussion.

5.3 Absorption Process in Si

Two processes are the dominant contributions to the absorption up to a wavelength of 5.0 μm in silicon: indirect interband transition α_{BG} and free-carrier absorption α_{FC}, so that α can be expressed as:

$$\alpha = \alpha_{BG} + \alpha_{FC} \tag{5.2}$$

5.3.1 Indirect Interband Transitions

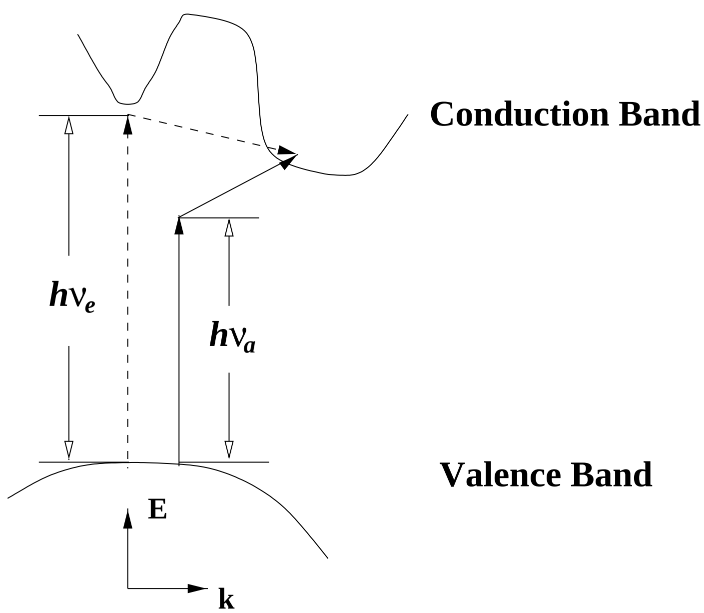

Figure 5.3: Schematic view of the indirect transitions in Si (E and k denote the energy and the wave vector). The solid lines show the involved process with phonon absorption ($h\nu_a$ denotes the photon energy in the process); whereas the dashed lines show that of phonon emission ($h\nu_e$ is the corresponding photon energy). One has: $h\nu_a = E_f - E_i - E_p$ for the phonon absorption process and $h\nu_e = E_f - E_i + E_p$ for the phonon emission process. E_p is the characteristic energy of the phonon, $E_i(E_f)$ denotes the electron energy of the initial(final) state.

The indirect transitions between the indirect valleys are illustrated in Figure 5.3. This kind of transitions is concerned with a two-step process. Either phonon emission or absorption is involved to conserve both energy and momentum. Since the involved phonon energy is very small compared to E_g, the transition is dominant in the near infrared region.

α_{BG} of this band-to-band absorption can be determined after Macfarlane's model, which was defined by Jellison *et al.*[29]:

$$\alpha_{BG}(h\nu, T) = \sum_i \sum_{l=1}^{2} (-1)^l \frac{\alpha_i(h\nu - E_g(T) + (-1)^l k\theta_i)}{exp[(-1)^l \frac{\theta_i}{T}] - 1} \tag{5.3}$$

where k is the Boltzmann constant, T is the absolute temperature and $h\nu$ the photon energy. $l = 1$ and $l = 2$ represent phonon emission and absorption respectively.

i in Eq. 5.3 denotes the different types of the phonons involved in the transition and $k\theta_i$ is the corresponding phonon energy. Two dominant phonons are taken into account in Si (i = 1, 2). One is the transverse acoustic phonon with θ_1 =212 K and the other is the transverse optical phonon with θ_2=670 K[30]. The denominator of the Eq. 5.3 arises from the Bose-Einstein phonon population.

$\alpha_i(x)$ with $x = h\nu - E_g(T) + (-1)^l k\theta_i$ gives the absorption from the transverse acoustic and optical phonons:

$$\alpha_1(x) = 0.504\sqrt{x} + 392(x - 0.0055)^2 \qquad x \geq 0.0055\, eV \tag{5.4}$$
$$= 0.504\sqrt{x} \qquad 0 \leq x \leq 0.0055\, eV \tag{5.5}$$
$$= 0 \qquad x < 0 \tag{5.6}$$

$$\alpha_2(x) = 18.08\sqrt{x} + 5760(x - 0.0055)^2 \qquad x \geq 0.0055\, eV \tag{5.7}$$
$$= 18.08\sqrt{x} \qquad 0 \leq x \leq 0.0055\, eV \tag{5.8}$$
$$= 0 \qquad x < 0 \tag{5.9}$$

where α is in units of $cm^{-1}$and x in eV.

To calculate α_{BG} with Eq. 5.3 one uses the temperature dependence of the band gap energy E_g with[31]:

$$E_g(T) = 1.155 - \frac{4.73 \times 10^{-4} T^2}{635 + T} eV \tag{5.10}$$

In this way α_{BG} can be determined as a function of wavelength and temperature. Since the band gap of Si narrows with the increasing temperature, the absorption edge is expected to shift to longer wavelength when the temperature increases.

5.3.2 Free-carrier Absorption

As presented above, α_{BG} is dominant for the short wavelengths. It drops significantly with increasing wavelength. In the infrared region one has also to consider the free-carrier absorption, by which a carrier is free to move inside a band by interacting with its ambient (see Figure 5.4).

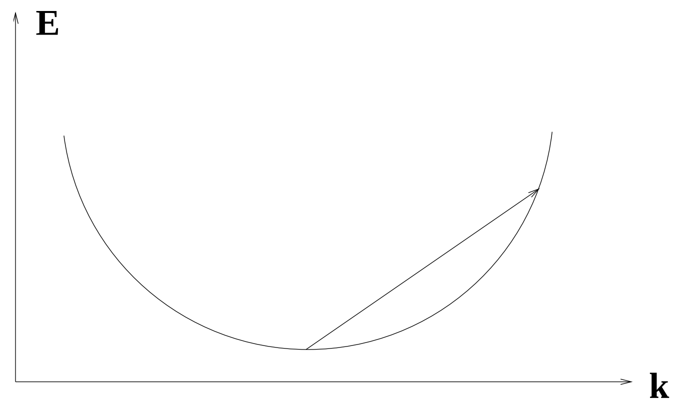

Figure 5.4: Transition of a free electron in the conduction band (E and k denote the energy and the wave vector).

The free-carrier absorption grows as λ^p, where p can range from 1.5 to 3.5 for different semiconductors. It is also been found to increase with the temperature. The free-carrier absorption coefficient α_{FC} of Si can be expressed as[32]:

$$\alpha_{FC} = n \cdot \sigma_n + p \cdot \sigma_p \tag{5.11}$$

where n and p denote the carrier concentration; σ_n and σ_p are the absorption cross section, which are found to have a classical λ^2 wavelength dependence for the wavelength between 1.0 μm and 1.6 μm[32]:

$$\begin{aligned} \sigma_n &= 1.01 \times 10^{-12} \cdot T \cdot \lambda^2 \\ \sigma_p &= 0.51 \times 10^{-12} \cdot T \cdot \lambda^2 \end{aligned} \tag{5.12}$$

With a doping of 10^{18} cm^{-3}, α_{FC} is estimated to be 4 cm^{-1} for a wavelength of 1064 nm, which is comparable to that from interband transition. For weakly doped Si however, the free-carrier absorption plays only a minor role at room temperature in the near infrared region (λ ¡ 1100 nm).

5.3.3 Measurement of Infrared Absorption in Si

The transmittance of a 300 μm thick Si wafer was measured to determine the absorption coefficient. A Perkin-Elmer Lambda 2 spectrometer[33] made the measurement possible for a wavelength range from 200-1100 nm. The result of the transmittance measurement is shown in Figure 5.5 (a). As expected, the transmittance rises with increasing wavelength.

Taking into account the multiple internal reflections in the thin wafer, the absolute transmittance t is given as[34]:

$$t = \frac{(1-R)^2 exp(-\alpha d)}{1 - R^2 exp(-2\alpha d)} \tag{5.13}$$

d is the thickness of the probe. R is the surface reflectance, determined as $R = [(n-1)^2+k^2]/[(n+1)^2+k^2]$, where $n(k)$ is the real (imaginary) part of the complex refractive index. Since k is very small compared to n in the investigating range of the wavelengths, it can be neglected in the calculation.

Using Eq. 5.13 the absorption coefficient of Si can be determined (using $n = 3.55$ as constant). The result is shown in Figure 5.5 (b).

As discussed above, the infrared absorption in Si is mainly concerned with the indirect interband transitions and the free-carrier transitions. Therefore the absorption coefficient is fitted as $\alpha = \alpha_{BG}+C$ (in cm^{-1}). This leads to E_g =(1.120±0.001) eV by applying Eq. 5.3 and C = (7.470±0.563) cm^{-1} . The fitted E_g is in good agreement with the calculation from Eq. 5.10 (1.112 eV at T=290 K).

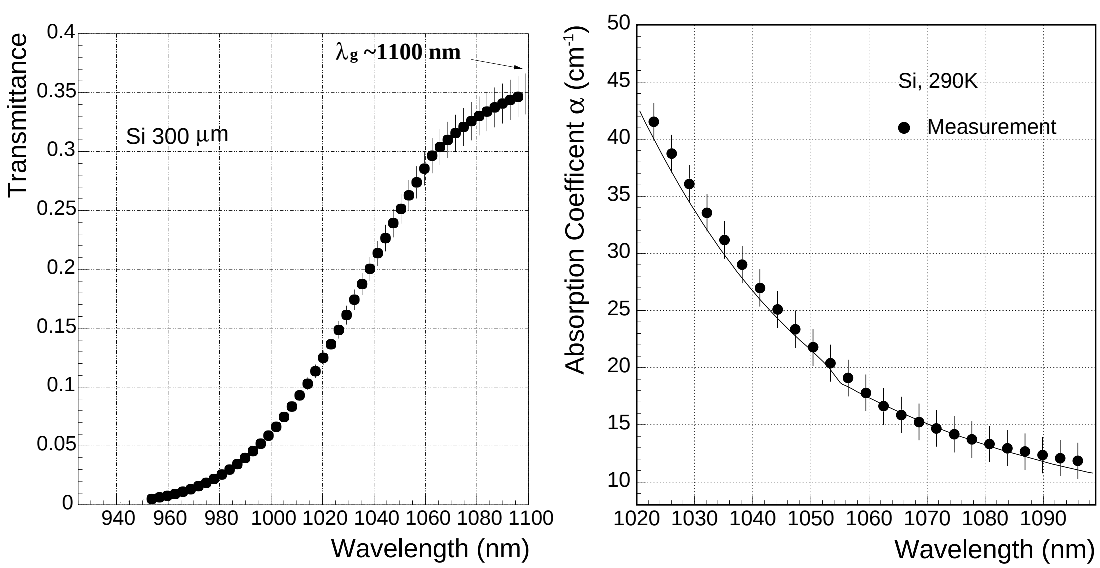

(a) Transmittance of a Si wafer in dependence of wavelength. The band gap energy corresponds to a wavelength of 1100nm.

(b) Absorption coefficient of Si in dependence of wavelength. Solid curve presents the fit to the data.

Figure 5.5: Transmittance and absorption coefficient measured with a 300 μm thick Si wafer (measurements were made at room temperature).

5.4 Absorption Process in GaAs

Three processes are relevant for the absorption in GaAs in the infrared region:

- direct interband transitions
- EL2 absorption
- free-carrier absorption

5.4.1 Direct Interband Transitions

Allowed direct interband transition is concerned with the absorption transition between two direct valleys where all the momentum-conserving transitions are allowed (see Figure 5.6). The absorption coefficient α is given as[35]:

$$\alpha = A^*(h\nu - E_g)^{1/2} \tag{5.14}$$

where $h\nu$ is the photon energy, E_g is the band gap energy. A^* is a coefficient depending on the refractive index and the effective mass of electrons and holes of the semiconductor.

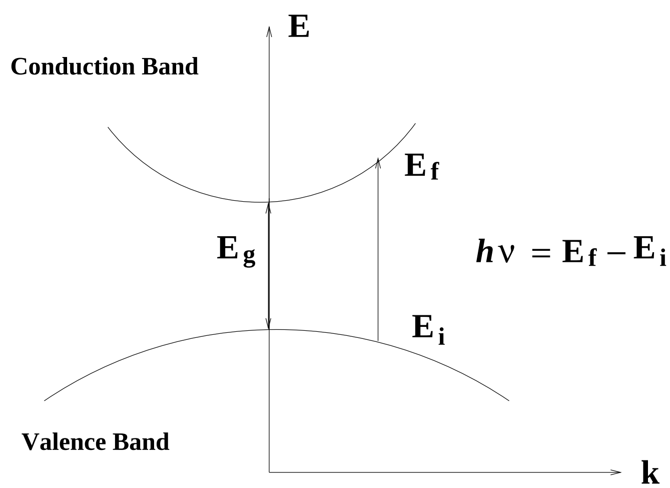

Figure 5.6: Allowed direct transitions in GaAs. E_g is the band gap energy (E_g=1.42 eV at 300 K for GaAs, which corresponds to λ_g=875 nm). E_i is the electron energy of the initial state, while E_f the energy of the final state. $h\nu$ is the photon energy.

With E_g of 1.42 eV at 300 K in GaAs, the direct band-to-band transition is dominant if the photon wavelength $\lambda < 875$ nm at room temperature.

It is expected from Eq. 5.14 that there is no absorption below the band gap. But in practice the optical absorption is found to increase exponentially with the photon energy $h\nu$ in the absorption edge region just below the band gap. This exponential absorption edge of GaAs is concerned with the transitions between the band tails, which can be controlled by doping. One has [36]:

$$\alpha = \alpha_g exp(\frac{h\nu - E_g}{E_o}) \tag{5.15}$$

where E_o is the characteristic width of the absorption edge. E_g is the extrapolated band gap energy and α_g is the absorption coefficient at this band gap energy. All the parameters E_g, E_o and α_g are dependent on the temperature.

5.4.2 EL2 Absorption

The GaAs wafers used for the investigations in this work were produced with the LEC[1]-grown technology[37]. Due to the resulting low effective carrier concentration the GaAs becomes the so called semiinsulating (SI)-GaAs . As a consequence a typical detector with a thickness of 250 μm can be fully depleted at reasonable operation voltages ($\leq$ 200 V).

SI-GaAs contains a high concentration of the lattice defect EL2. The photoionization of EL2[38] (energy level of EL2 is shown Figure 5.7) turns out to be a dominant contribution to the optical absorption in the spectral range 950 nm $\leq \lambda \leq$ 1400 nm. Generally this kind of the transitions between the impurity(defect) and the band levels can be divided into four categories, as shown in Figure 5.8.

The absorption coefficient due to EL2 absorption is given as [40] :

$$\alpha_{EL2} = N_{EL2}[f\sigma_n + (1-f)\sigma_p] \tag{5.16}$$

where N_{EL2} is the total EL2 concentration. σ_n and σ_p are the optical cross sections of the electron ionization and hole ionization respectively. $f(0 \leq f \leq 1)$ is the occupation function of EL2, which is determined as:

$$f = [1 + exp(-E_F - E^{\cdot}_{EL2}/kT)]^{-1} \tag{5.17}$$

where E_F is the Fermion energy. $E^{\cdot}_{EL2}$ is the effective EL2 energy (which includes the contribution from a degeneracy factor); it is given as $E^{\cdot}_{EL2} = 0.759 - 0.237 \times 10^{-3}T$ [40].

Using the typical parameters of the probe made of LEC GaAs listed in the Table 5.9, one has α_{EL2} =1.02 cm^{-1} at a wavelength λ=1100 nm at room temperature. Due to the high f the dominant contribution to the EL2 absorption is from the photoionization of electrons.

[1]Liquid Encapsulated Czrochalski

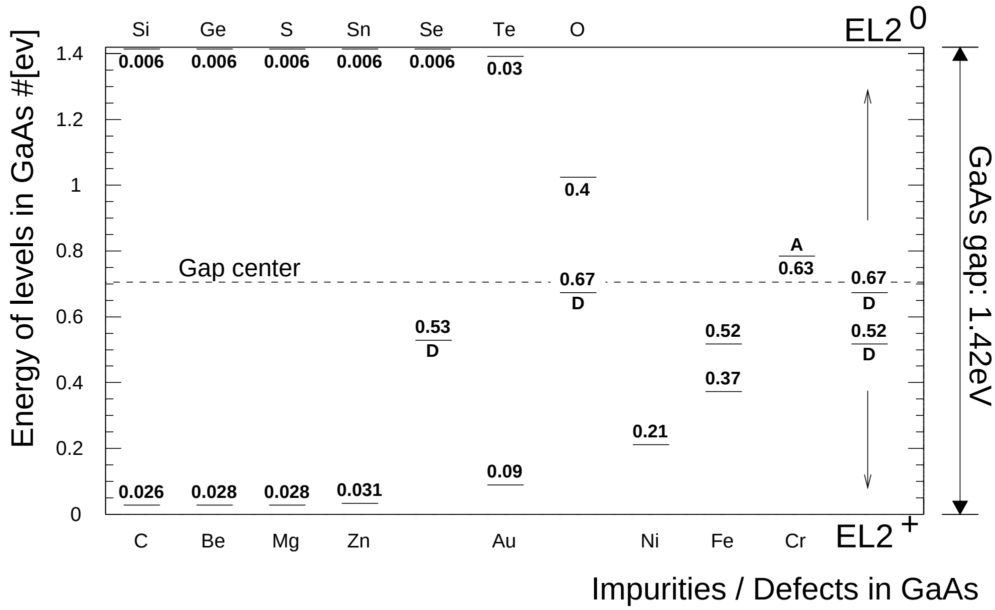

Figure 5.7: Energy levels of various impurities and defects in the energy band diagram of GaAs[27][39]. The levels below the gap center are referred to the top of the valence band; they are acceptor levels unless those indicated by D for donor levels. The levels above the gap center are referred to the bottom of the conduction band; they are donor levels unless those indicated by A for acceptors. The most important lattice defect in SI-GaAs is EL2. The energy level of the neutral EL2 is 0.67 eV above the top of the valence band at 300 K, while the energy level of $EL2^+$ (ionized EL2) is roughly 0.52 eV above it.

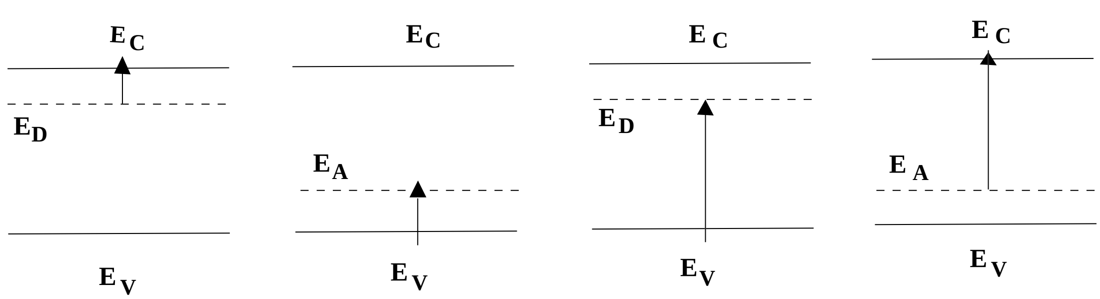

Figure 5.8: Absorption transition between impurities(defects) and bands: (a) donor to conducting band; (b) valence band to acceptor; (c) valence band to donor; (d) acceptor to conduction band. The energy of the photon in the absorption process must be at leat equal to the ionization energy of the impurity(defect).

	LEC GaAs	
N_{EL2}	10^{16}	cm^{-3}
N_A	$5 \cdot 10^{14}$	cm^{-3}
N_D	$4 \cdot 10^{14}$	cm^{-3}
E_F (above the valence band)	0.807 [41]	eV
σ_n (λ=1100 nm, T=300 K)	9.07×10^{-17} [42][43]	cm^2
σ_p (λ=1100 nm, T=300 K)	3.20×10^{-17} [42][43]	cm^2

Figure 5.9: Typical parameters of LEC GaAs.

5.4.3 Free-carrier Absorption

The free-carrier absorption of GaAs is measured to be:

$$\alpha_{FC} = 5.0 \cdot 10^{-20}\, N \tag{5.18}$$

at a photon wavelength of 1064 nm at 300 K. N is the free-carrier concentration. Since the GaAs probe being studied here (parameters given in Table 5.9) has a very low concentration ($n = 2.01 \times 10^7$ cm^{-3}, $p = 1.96 \times 10^5$ cm^{-3} [41]), α_{FC} can be ignored in our case.

5.4.4 Measurement of Infrared Absorption in GaAs

The same experimental setup presented in Section 5.3.3 was also used to measure the transmittance of a 250 μm thick GaAs wafer. Figure 5.10 (a) shows the result of such a measurement. As expected, the transmittance drops steeply with decreasing wavelength.

By applying the Eq. 5.13 the absorption coefficient α can be determined. The result is shown in Figure 5.10 (b). It can be seen that the absorption coefficient decreases significantly at small wavelength.

As discussed above, the absorption just below the band gap is dominated by the transitions between the band tails. The measurement data are therefore fitted according to Eq. 5.15. The fit curve leads to: α_g=(7432 $\pm$ 935) cm^{-1}, E_o =(5.02$\pm$0.17) meV, E_g=(1.422$\pm$0.0003) eV at room temperature. The fitted parameters of E_o and α_g are in agreement with the literature values (E_o= 5.9(7.5) meV in [44] ([36]) and α_g=8000 cm^{-1} in [45]). The fitted value of E_g from the measurement is also in agreement with the theoretical value E_g = 1.427 eV at a temperature T=290 K [31].

Figure 5.11 shows the measured absorption in a Si and GaAs wafer by means of the spectrometer (both wafers are 250 μm thick). It can be seen that the drop of absorption just below the band gap is much steeper in GaAs than that in Si and the absorption of GaAs in the infrared region is much less than that of Si. However, by applying high laser intensity and a reflective backside it is still possible to detect charge injection with GaAs detectors, as it will be shown in the next section.

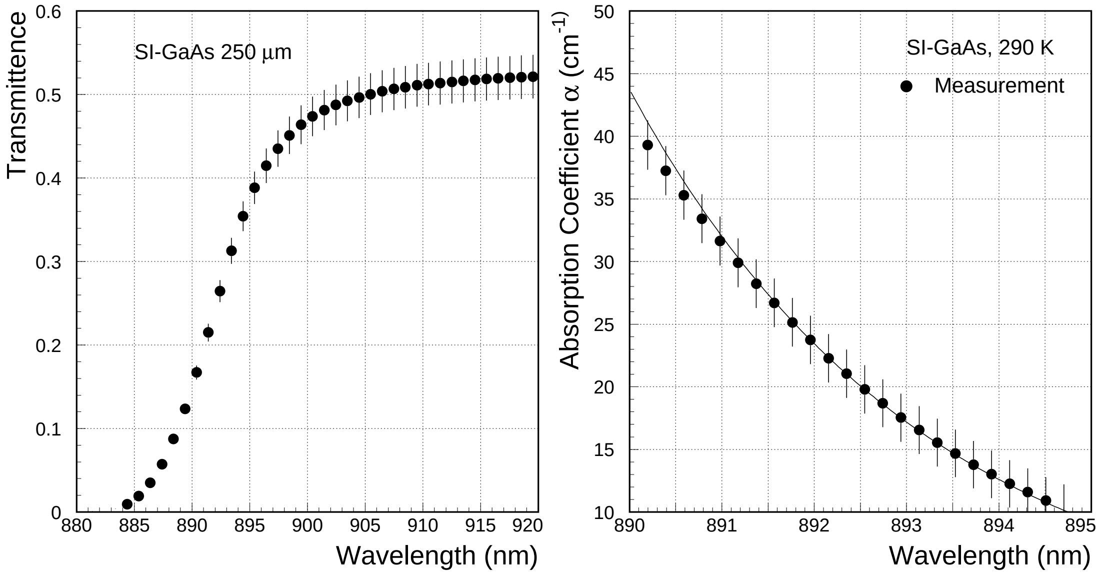

(a) Transmittance of a GaAs wafer in dependence of wavelength. The band gap energy corresponds to a wavelength of 875nm.

(b) Absorption coefficient of GaAs in dependence of wavelength. Solid curve presents the fit to the data.

Figure 5.10: Transmittance and absorption coefficient measured with a 250 μm thick GaAs wafer (measurements were made at room temperature).

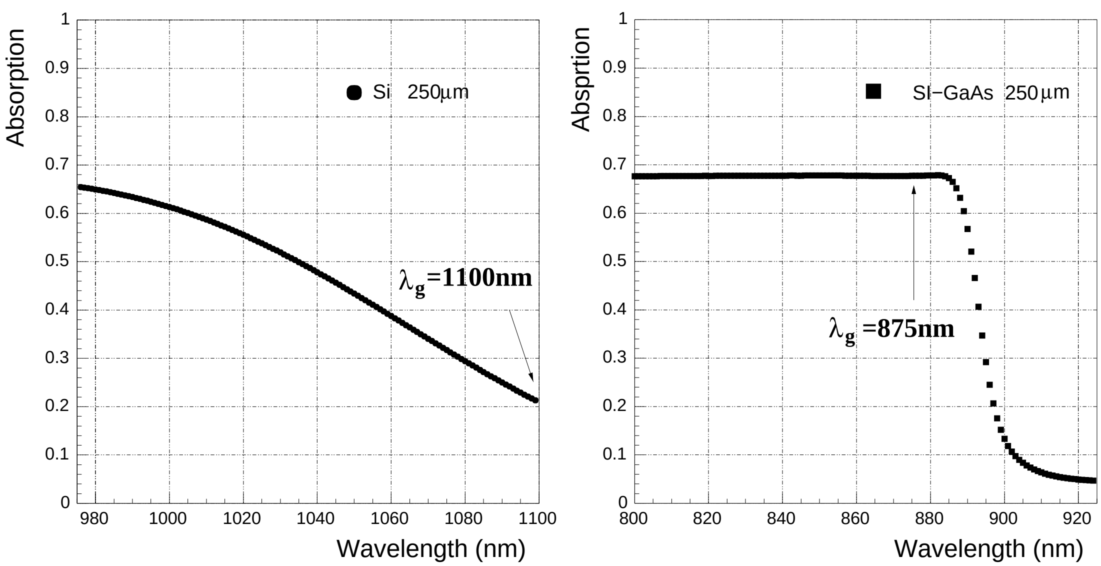

Figure 5.11: Absorption of Si (250 μm thick) [46] and GaAs (250 μm thick) .

5.5 Measurement of GaAs Schottky Diode with a Pulsed Laser

Pulse height spectra of a GaAs Schottky diode were measured with a 1084 nm laser diode[47] (the same laser diode used for the AMS Alignment System[48]). The diode was built by the I. Physics Institute of RWTH Aachen. Figure 5.12 shows a schematic view of such a GaAs diode with a thickness of 250 μm. Figure 5.13 shows the I-V characteristic of the Schottky diode.

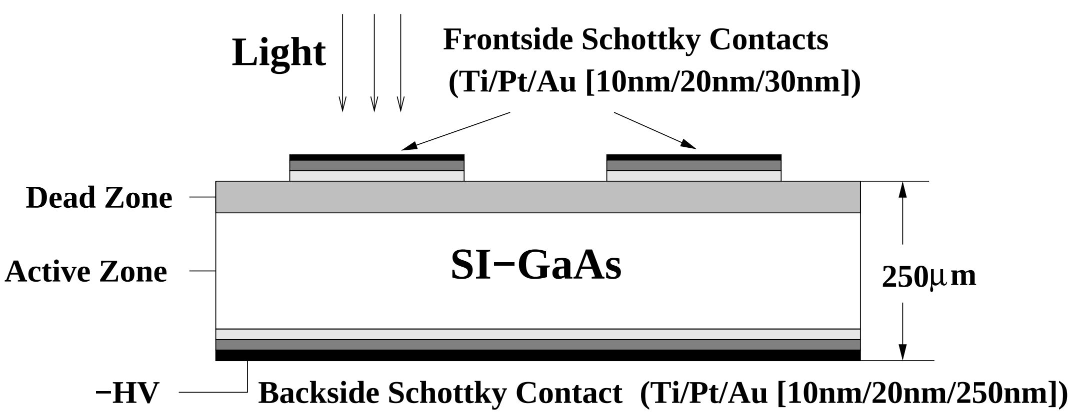

Figure 5.12: Structure of a GaAs Schottky diode (made of a SI-GaAs bulk with Schottky contacts on both the frontside and the backside). The laser illuminates the frontside of the diode.

5.5.1 Distribution of Electric Field and Charge Collection Efficiency in Schottky Diode

The GaAs diode can be divided into an active zone where the electric field $E >$ 2 kV/cm and a dead zone with $E <$ 2 kV/cm (see Figure 5.12). In the active zone the drift velocity of the electrons is constant with $v_e \sim 10^7$ cm/s, whereas in the dead zone the generated free-carriers have a very low free drift length so that their contribution to signal is much less than that from the active zone.

The distribution of the electric field in the Schottky diode is shown in Figure 5.14 (a). Figure 5.14 (b) shows the thickness of the active zone as a function of reverse bias voltage. Generally the thickness X_A of the active area is determined by EL2 concentration, the energy level of EL2, the density of shallow donors(acceptors), leakage current density, thickness of the detector and the applied reserver bias voltage.

After the Ramo's theorem[50] the local charge collection efficiency $\varepsilon_A(x_o)$ for a MIP signal in the active area is given as:

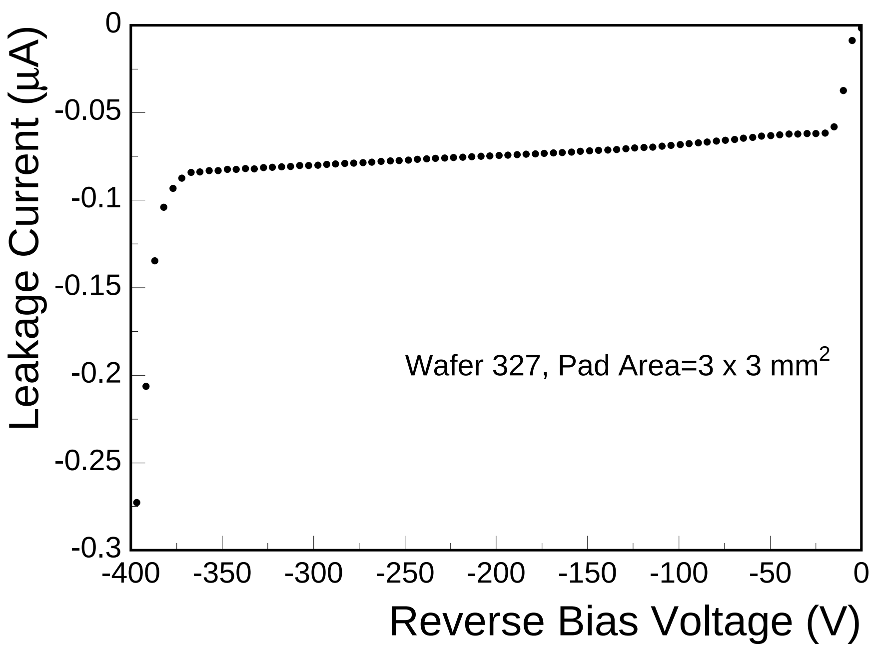

Figure 5.13: I-V characteristic of the GaAs Schottky diode.

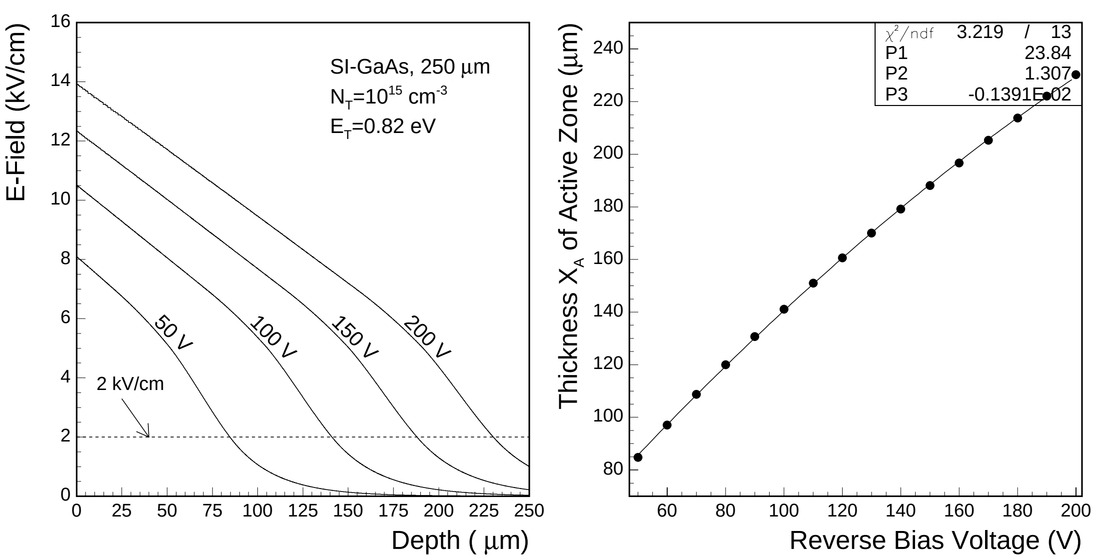

(a) Distribution of the electric field for a SI-GaAs detector at diferent reserse bias voltages.

(b) Thickness of the action zone as a function of reverse bias voltage (solid line is the fit to the data).

Figure 5.14: Electric field and thickness of the active zone in a 250 μm thick GaAs detector[49].

$$\varepsilon_A(x_o) = \frac{1}{d}[\int_o^{x_o} e^{\frac{x-x_o}{\lambda_h^A}} dx + \int_{x_o}^{X_A} e^{\frac{x_o-x}{\lambda_e^A}} dx + e^{-\frac{X_A-x_o}{\lambda_e^A}} \int_{X_A}^{d} e^{\frac{X_A-x}{\lambda_e^D}} dx\,] \quad (5.19)$$

where $\lambda_e^A(\lambda_e^D)$ and $\lambda_h^A(\lambda_h^D)$ are the mean free drift lengths of electrons and holes in the active(dead) zone. The first term describes the contribution from the drifting holes and the second term describes the contribution from the electrons drifting toward the dead zone. The third term represents those electrons which reach the dead zone and drift toward the forward biased Schottky contact. Similarly the local charge collection in the dead zone $\varepsilon_D(x_o)$ is expressed as:

$$\varepsilon_D(x_o) = \frac{1}{d}[\int_{x_o}^{d} e^{\frac{x_o-x}{\lambda_e^D}} dx + \int_{X_A}^{x_o} e^{\frac{x-x_o}{\lambda_h^D}} dx + e^{\frac{X_A-x_o}{\lambda_h^D}} \int_0^{X_A} e^{-\frac{X_A-x}{\lambda_h^A}} dx\,] \quad (5.20)$$

For the MIP signal, the charge collection efficiency ε_{MIP} is determined as:

$$\varepsilon_{MIP} = \frac{1}{d}[\int_0^{X_A} \varepsilon_A(x_o)dx_o + \int_{X_A}^{d} \varepsilon_D(x_o)dx_o\,] \simeq \frac{1}{d}\int_0^{x_A} e_A(x_o)dx_o \quad (5.21)$$

By using a laser beam with a wavelength of 1084 nm, the absorption coefficient α is of the order of 1 cm^{-1} so that electrons and holes are generated homogeneously along the propagation track. However, the contributions from the electrons and holes are different due to the different occupation function. The ratio between the two contributions is denoted as η, the charge collection efficiency ε_{laser} is therefore defined as:

$$\varepsilon_{laser} = \varepsilon_e + \eta \cdot \varepsilon_h \quad (5.22)$$

where $\varepsilon_e(\varepsilon_h)$ describes the contribution from the electrons(holes), which can be determined according to Eq. 5.19 and Eq. 5.20.

5.5.2 Experimental Setup

The setup of the laser system is shown in Figure 5.15. It is incorporated in the test setup with radioactive sources[41]. Only a minor modification was made in terms of a different trigger systems. The 1084 nm laser diode is self-triggered and the minimum pulse length of the laser is 100 ns. The output of the laser diode is coupled to a single mode (SM) fiber. The beam from the fiber is then directed to the frontside of the GaAs diode.

The charge pulses from the GaAs diode are amplified and converted to voltage pulse by a charge sensitive preamplifier (PA). The output of the preamplifier is connected to a pulse shaper (SHA) and is then amplified by a main amplifier (MA1) with a peaking time of 2.2 μs.

After that the signal is transfered to a delay unit and then to an analogue-to-digital converter (ADC). From that the signal is readout by a PC through a CAMAC interface. The signal is additionally connected to a discriminator (DIS) followed by a gate generator (GG). The output of the gate generator is used as the gate for the ADC. The pedestal position is obtained by independent radom triggers produced by a pulse generator (PG).

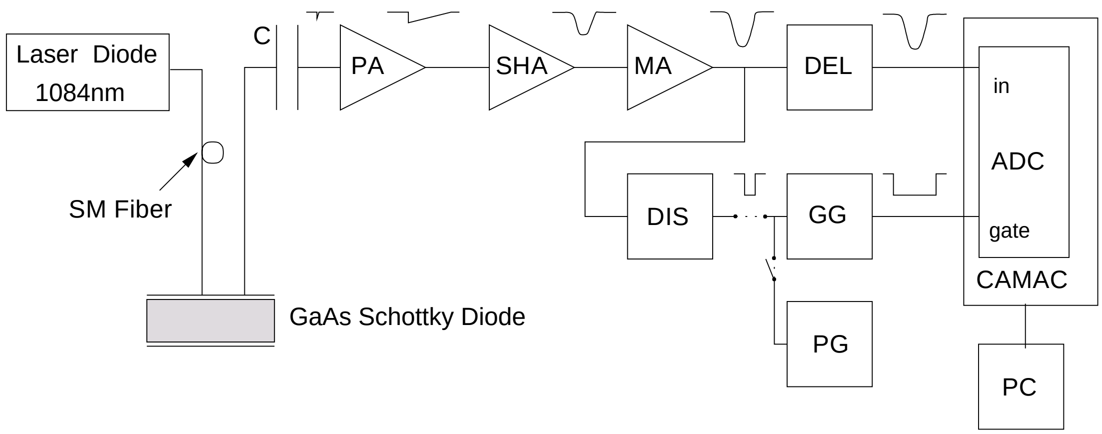

Figure 5.15: Schematic view of the test setup with a 1084 nm laser diode.

5.5.3 Results

Figure 5.16 shows a typical pulse height spectrum of the laser pulses measured at a reverse bias voltage of 200 V. In comparison to the asymmetric form of a MIP signal (resulting from the Landau distributed energy deposition), the laser pulse spectrum has a distinctive Gaussian distribution. Measurements with the test pulses demonstrate a good linearity up to an input charge of $1.62{\times}10^5$ e^- and the calibration factor is determined to be 180 e^-/bin. Therefore the mean signal of the spectrum is evaluated as $3.8{\times}10^4$ e^- (∼1.1 MIPs in a 250 μm thick GaAs detector).

Laser signals were measured in dependence of laser current and bias voltage respectively. The results are shown in Figure 5.17. A good linearity between the signal height and the laser current is measured provided that the laser diode is operated above its threshold current of about 85 mA (see Figure 5.17 (a)).

In Figure 5.17 (b) the theoretical values of charge collection efficient ε are calculated and they are normalized with $\varepsilon = 1$ at a reverse bias voltage of 200 V; η in Eq. 5.22 is set to 0.1. The measured signal height is also normalized by setting the signal to 1 at the bias voltage of 200 V. It shows a good agreement between the measurement and the calculation.

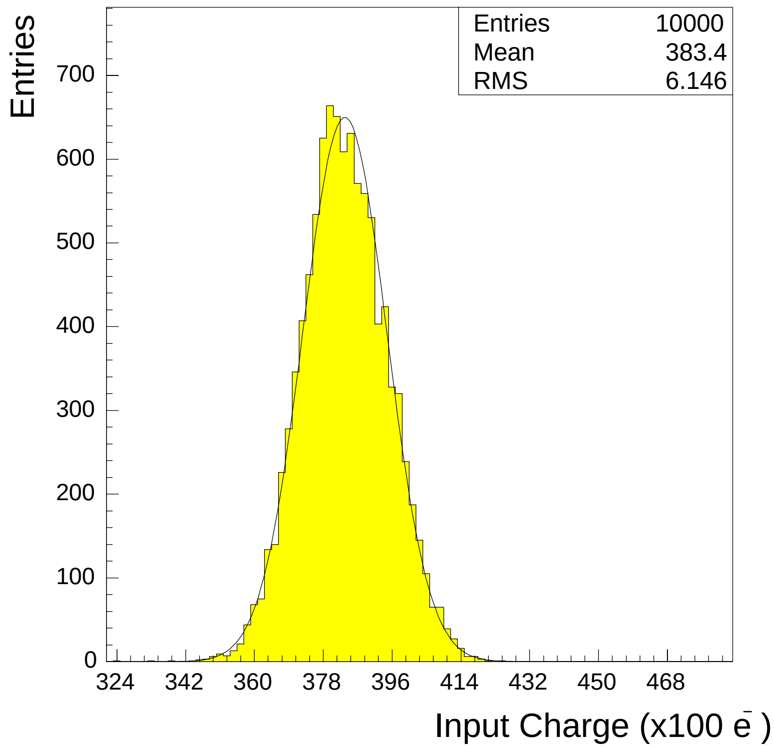

Figure 5.16: Pulse height spectrum for the laser pulses from the 1084 nm laser diode (pedestal subtracted).

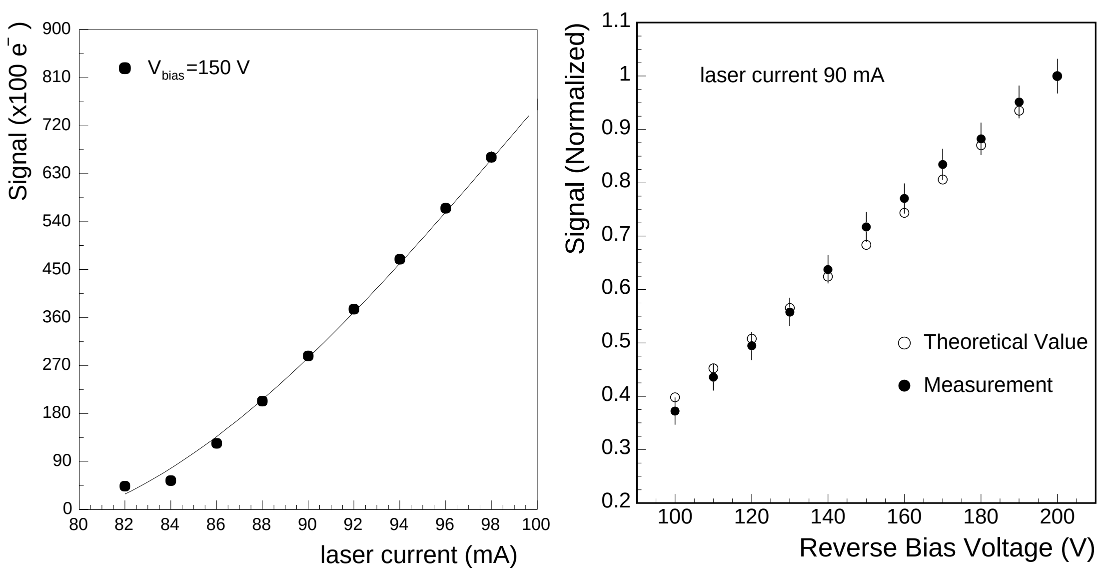

Figure 5.17: Signal in dependence of laser current and reverse bias voltage.

5.6 Measurement of GaAs Strip Detector with a Pulsed Laser

I also measured a GaAs strip detector with a 1064 nm Nd:YAG laser. Detailed investigations on Si strip detectors with the pulsed laser can be found in [51][52].

The GaAs detector was fabricated by the I. Physics Institute of the RWTH Aachen[53][54]. A schematic overview of the detector is presented in Figure 5.18. There are all together 128 strips on the detector; each strip is 30 mm long and 25 μm wide; the pixel pitch is set to 50 μm. The experimental setup is illustrated in Figure 5.19. A detailed description of the laser system can be found in Chapter 6.

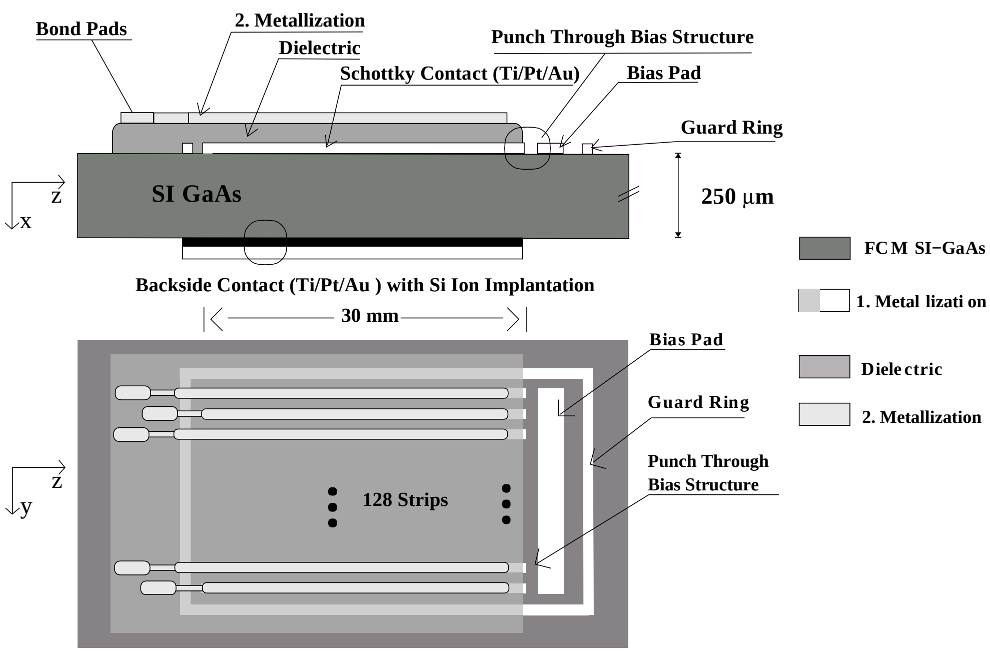

Figure 5.18: Schematic overview of a GaAs strip detector prototype[53]. There are all together 128 strips on the detector; the strip pitch is 50 μm.

The start signal for the laser driver is generated by a sequencer[55]. The sequencer also sends out digital control signals to the detector via a fast trigger board and mother board[56]. The readout chip of the GaAs strip detector is the so called Premux128 chip[57]. The analog output of the readout chip is digitized by a 8-Bit FADC[58]. Both sequencer and FADC are programmed by a PC via a VME interface.

The laser collimator is situated on a x-y stage, so that the position of the laser spot can be moved in two dimensions. Figure 5.20 shows the measured beam profile. It has a Gaussian distribution with a standard variance of about 0.25 mm (5 strips). The integrated signals spread over the strips are estimated to be 5.0×10^5 e^-, which is about 14.7 MIP signals.

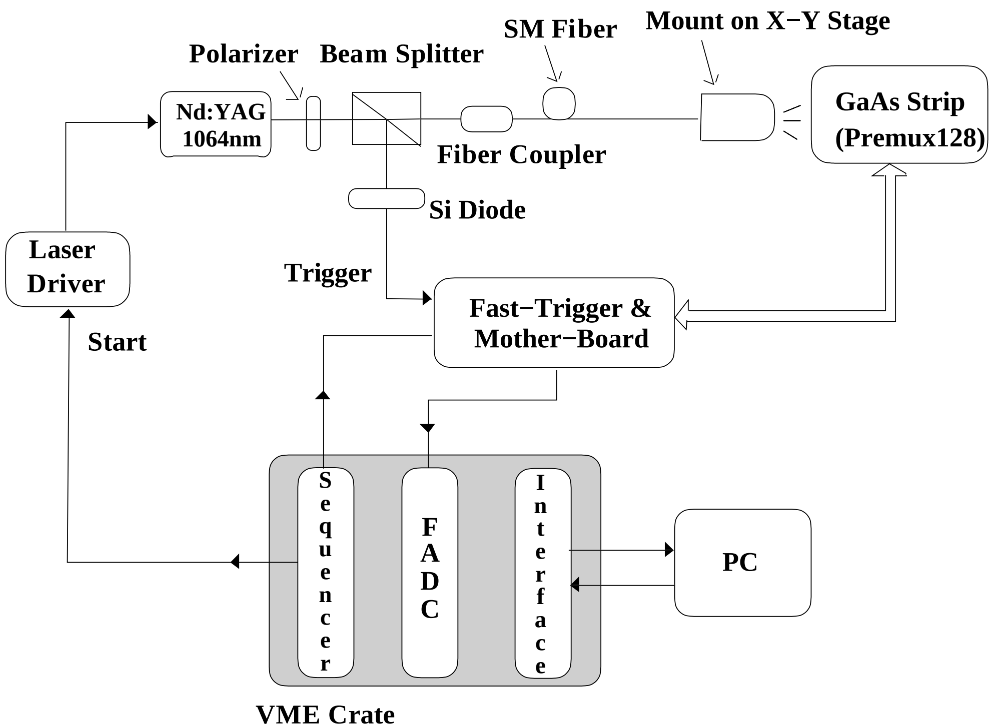

Figure 5.19: Experimental arrangement of a Nd:YAG laser system. The output of the laser is sent to the front side of the GaAs strip detector.

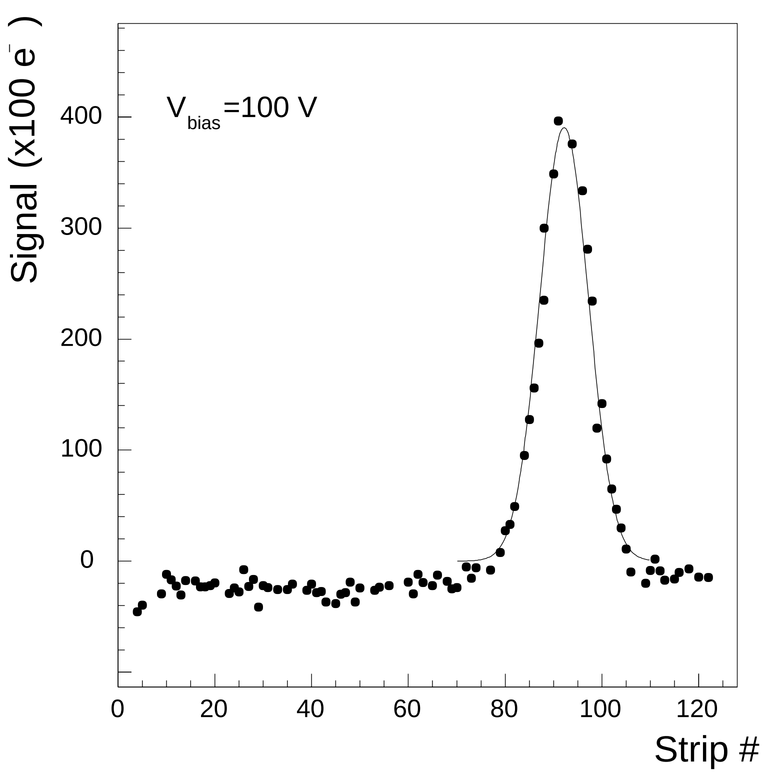

Figure 5.20: Beam profile of the output of the 1064 nm Nd:YAG laser, measured with the GaAs strip detector with a pitch of 50 μm.

5.7 Summary

The transmittance of Si and GaAs wafers were measured to determine the absorption coefficient α of both materials in the infrared region. The measured α of Si can be described as the sum of α_{BG} and a constant. The dominant contribution α_{BG} comes from the indirect interband transitions, in which transverse acoustic and optical phonons are either absorbed or emitted. The extrapolated value of the band gap energy E_g is in good agreement with the theoretical value. At a wavelength λ of 1064 nm the transmittance is measured to be 30% (the wafer is 300 μm thick) and α is 15 cm^{-1}.

α was also determined for GaAs in a narrow wavelength range just below the band gap. It can be seen that α of GaAs drops steeply with increasing λ. The dominant contribution to the absorption is concerned with the transitions between the band tails. The fitted values of E_g, E_o (the characteristic width of the absorption edge) and α_g (the absorption coefficient at E_g) are in agreement with the literature. The transmittance is measured to about 50% when λ is above 905 nm (the wafer has a thickness of 250 μm). At a wavelength of 893 nm α is measured to be 15 cm^{-1}.

In comparison to Si, the change of α of GaAs is much more significant near the band gap and the absorption is much lower in the near infrared region. At λ=1064 nm the absorption of 250 μm thick Si is measured to be 35%, whereas the absorption in GaAs of the same thickness is only about 2%.

With the help of high laser intensity and a reflective backside, signals from a 1084 nm laser diode and 1064 nm Nd:YAG laser were detected with a GaAs diode and strip detector respectively. At both wavelengths the absorption is mainly caused by the EL2 ionization; α is estimated to be of the order of 1 cm^{-1} and the photon energy is deposited homogeneously along the propagation path. The pulse height spectrum of the laser diode was measured with the diode; it shows a distinctive Gaussian distribution. The beam profile of the Nd:YAG laser was measured with the strip detector; it has a Gaussian distribution with a standard variance of 0.25 mm (5 strips). The integrated charge signal is equal to 14.7 MIPs.

Chapter 6

Characterization of a Si Pixel Detector

This chapter is concerned with the test stands to characterize the CMS Si pixel detector prototype. Two signal sources are used: a test pulser and a laser pulser. The experimental arrangements (Section 6.1) will be first introduced, after that performance parameters will be described, such as: I-V characteristics (Section 6.2.1), full depletion voltage (Section 6.2.2), use of the trim bits (Section 6.2.3), threshold distribution (Section 6.2.3), noise (Section 6.2.4), pulse form (Section 6.2.5), peaking time (Section 6.2.5), time walk (Section 6.2.5), linearity (Section 6.2.6), gain (Section 6.2.6) and spatial resolution (Section 6.2.7). Finally results of the measurements with the test pulses and the laser pulses will be presented and discussed.

6.1 Test Setup

6.1.1 Introduction

The measurements with the test and laser pulses are incorporated in the same setup sketched in Figure 6.1. It is based on two subsystems: the readout system of the pixel detector and the test pulse (laser pulse) system. The test setup was designed for both Si and GaAs pixel detectors. However, since no GaAs pixel detectors with transparent backside were available, the measurements have only been done with a CMS Si pixel detector prototype. The prototype is made of a Si bulk with a thickness of 250 μm; the pixels of the detector are arranged in a 22x32 array with a pitch of 125 μm.

As shown in Chapter 3, the pixel sensor is bonded to an AC30 chip via bump bonding. The pixel detector is then connected to an interface card via a fine pitch connector. Both the detector and the card are electromagnetically shielded in a box made of aluminum, which is cooled with compressed air at a temperature of about 16^{o}C.

6.1.2 Readout System

The electronics chain for controlling and reading out the pixel detector consists of the following:

- Sequencer[55], which generates the fast digital control signals for the AC30 chip such as PHI1, PHI2 etc.
- IO-Register[59] generating the slow digital signals such as PPHI1, PPHI2
- FADC (40 MHz 12-Bit, [60]) digitizing the output signal A_{out} and D_{out} of the chip
- Signal preparation board: signals from the sequencer and the IO-Register are transfered to the signal preparation board and converted to appropriate signal levels.
- Interface card: signals and voltages from the signal preparation board are transfered to the chip via the interface card, as well as the external test pulses from a pulse generator. Analog drivers of A_{out} and D_{out} are also implemented on the card. It is also possible to change manually the supply

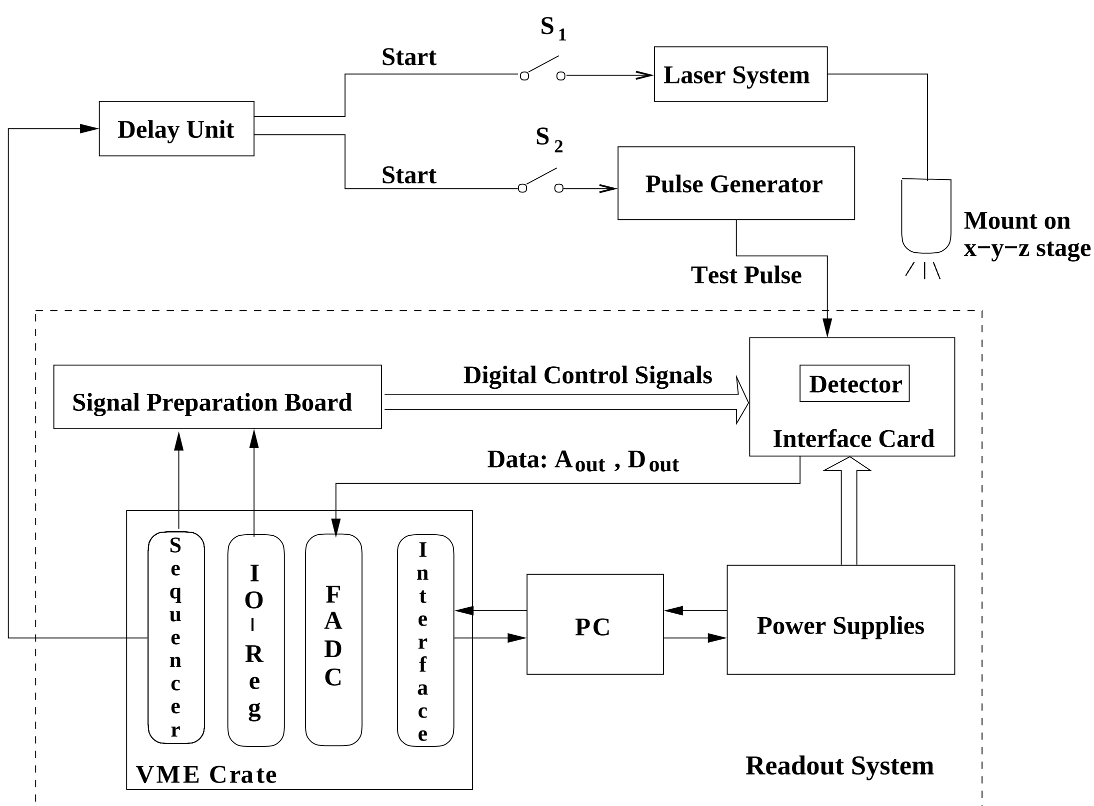

Figure 6.1: Experimental setup to characterize the CMS pixel detectors with test pulses and laser pulses.

and control voltages of the chip by changing the corresponding resistors installed on the card.

- DC power supplies: providing the detector voltage, together with the supply and control voltages of the AC30 chip, including V_{ssf} (controlling the source follower), V_{ssana} (supply voltage of the analog part of the chip) and V_{comp} (controlling the global comparator threshold). The first two voltages cause the dominant contribution to the currents on the chip.

- VME Interface: the entire data taking is controlled by a master program running on a standard Pentium-PC which accesses the sequencer, the IO-Register and the FADC via the VME bus.

6.1.3 Test Pulse System

A start signal generated by the sequencer is first sent to a delay unit and from there to a pulse generator[61]. Pulses with varying amplitudes and pulse lengths are initiated. The delay unit is essential for the pulse form measurement. Details about the measurement will be given in Section 6.2.5.

6.1.4 Laser Pulse System

The laser system is principally composed of a laser driver, laser and the optics. Two kinds of light sources are used for the measurements:

- 670 nm laser diode
- 1064 nm Nd:YAG laser

	Laser Diode $\lambda = 670$ nm	Nd:YAG laser $\lambda = 1064$ nm	
absorption coefficient α	$\sim 10^3$	15	cm^{-1}
penetration depth d	~ 10	667	μm
absorption (300 μm thick)	0.70	0.30	

Table 6.1: Absorption parameters at wavelength of 670 nm and 1064 nm (d=1/α, the value of α is extracted from the measurements presented in Chapter 5).

Table 6.1 compares the parameters between the wavelength of 670 nm and 1064 nm. Due to the high absorption coefficient α at 670 nm the free carriers are generated only on the surface of the bulk. The benefit of using a laser diode is the simplicity and low cost of the test station. It is also possible to use normal optics apparatus for the focusing. Therefore it is more suitable to investigate parameters such as full depletion voltage, pulse shape and gain factors.

A Nd:YAG laser is a good source to simulate charged particle tracks; it is therefore a more reliable instrumentation to study spatial resolution. The laser provides much higher power than that of the laser diode, but the test setup is relatively complex. Special instruments have to made for the focusing. The interference effect caused by the multiple internal reflections also makes it difficult to calibrate the readout electronics for each pixel.

The technical specifications of the two light sources will be described in the following sections.

6.1.4.1 1084 nm Nd:YAG Laser

The Nd:YAG laser system is sketched in Figure 6.2. This configuration will be later referred as Laser III.

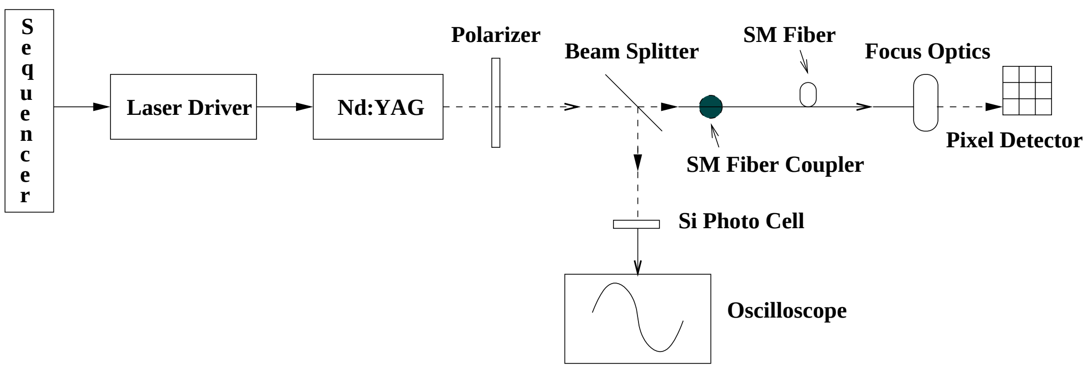

Figure 6.2: Schematic view of the Nd:YAG laser system.

The start signal for the laser driver is generated by a sequencer. The laser beam is first extracted by a polarizer so that the laser intensity can be modulated by rotating the polarizer. The beam is then sent to a beam splitter. One output of the splitter is led to a Si photo cell and the response signal is transfered to a digital oscilloscope so that the timing and intensity of the laser can be monitored. The laser beam passing through the splitter is transmitted to single mode (SM) fiber via a SM fiber coupler. The focused beam is finally sent to the backside of the pixel detector.

6.1.4.2 670 nm Laser Diode

The test stand with the 670 nm laser diode has two different configurations. One is similar to the arrangement with the Nd:YAG laser, where SM fiber coupler, fiber and focusing optics are employed. This configuration will be referred as Laser II.

The other configuration - Laser I is rather simple: the output of the laser diode is directly sent to the pixel detector. In order to maintain a Gaussian profile of the laser spot, the distance between the detector and the laser diode is kept of the order of several mm.

To sum up, Table 6.2 gives the technical data of the different configurations.

laser system	Laser I	Laser II	Laser III
light source	Laser Diode [62]	Fiber Pigtailed Laser Diode [63]	Nd:YAG [64]
wavelength (nm)	670	670	1064
pulse length (ns)	$\simeq$10	$\simeq$10	¡ 20
typical beam spot (FWHM in μm)	$\sim$600	$\sim$100	$\sim$200
experimental arrangement	without SM coupling	SM fiber, focusing optics	polarizer, beam splitter, SM fiber, focusing optics

Table 6.2: Specifications of three different configurations of the laser system.

6.1.5 X-Y-Z Stage

The laser output is mounted on a x-y-z stage to access different regions of the pixel detector. The coordinates of the stage are controlled by the PC. Figure 6.3 shows a photograph and the coordinate system of such a stage.

By moving the stage along the z-axis the distance between the laser source and the detector can be changed. The x-axis is parallel to the pixel columns of the detector, while the y-axis corresponds to the row direction. In this way the distribution of the laser spot over the pixels can be modulated by varying the distance between the focusing optics and the detector, while the charge sharing among the pixels can be changed by moving the stage in the x- and y-directions.

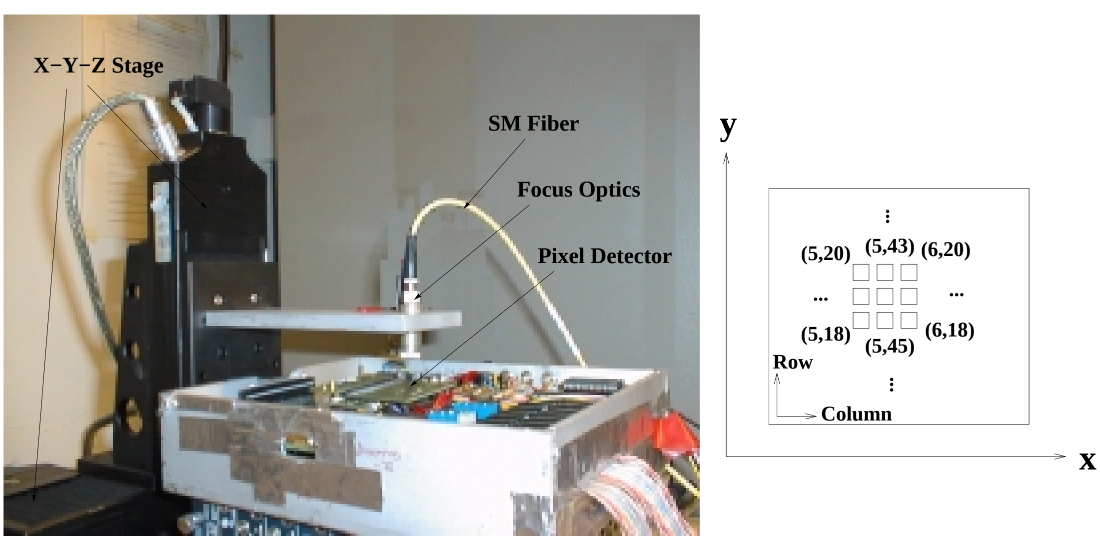

Figure 6.3: A photograph and the coordinate system of the x-y-z stage. (i,j) denotes the pixel with the double column number i (i = 1..11) and the pixel number j ($j = 1..64$).

Due to the geometrical layout of the pixel detector, the detector has to be illuminated from the backside. It is possible for the laser to enter the silicon bulk and deposit free-carriers in it, since the backside is not entirely metalized (only one small spot on the backside is aluminumized and it is wire bonded to V_{bias} on the fine pitch connector). The surface of the frontside of the AC30 chip is protected with an Aluminum layer. therefore when the laser transmits through the sensor (in the case of Laser III), the light will be reflected on the surface of the readout chip (see Figure 6.4).

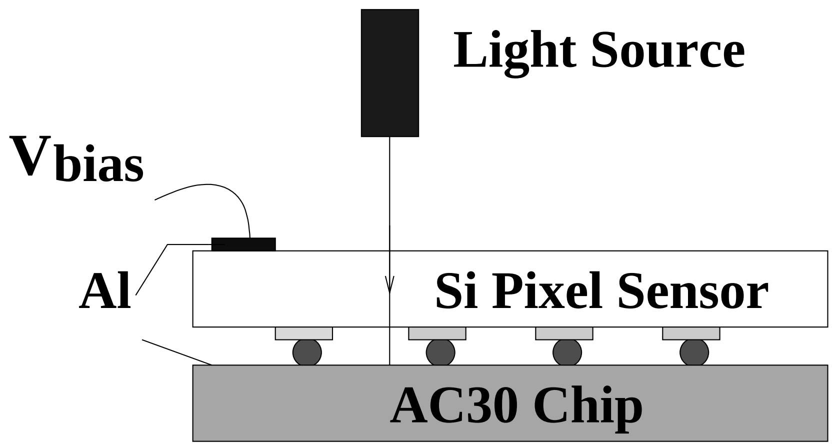

Figure 6.4: Schematic view of the laser source illuminating the backside of the detector.

6.1.6 Properties of Laser Output

Before characterizing the pixel detector with the laser pulses, beam profiles of the different sources have been investigated with the pixel detector.

6.1.6.1 Beam Profile of Laser I

Figure 6.5 shows such a 3-D and 2-D beam profile of Laser I (see Table 6.2). The laser spot has a Gaussian profile with a standard deviation of $\sim 248\ \mu$m.

6.1.6.2 Beam Profile of Laser II

Figure 6.6 shows a 3-D beam profile of Laser II. The measurements were taken at two different positions of the x-y stage. The beam width is found to be smaller than two pixel pitches (250 μm).

6.1.6.3 Beam Profile of Laser III

Figure 6.7 shows the 3-D beam profile of Laser III. The beam spot is found to be distributed over six pixels.

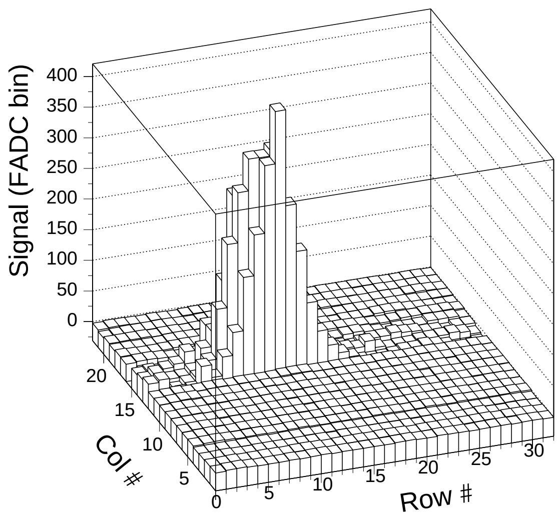

(a) Signals of the pixels arranged in a 22x32 array.

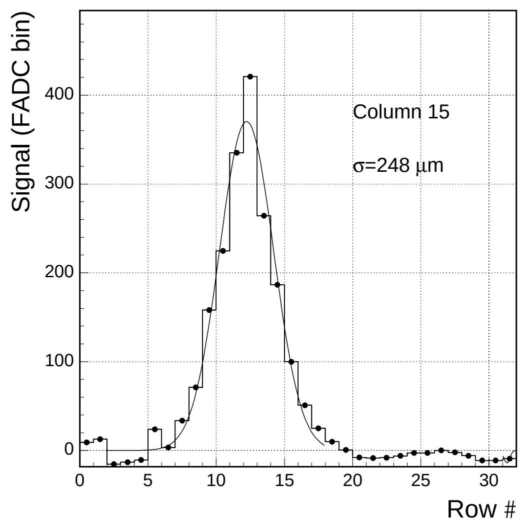

(b) Signals of the pixels in column 15.

Figure 6.5: 3-D and 2-D Profile of the laser spot from Laser I, measured with a 22x32 Si pixel array with a pitch of 125 μm.

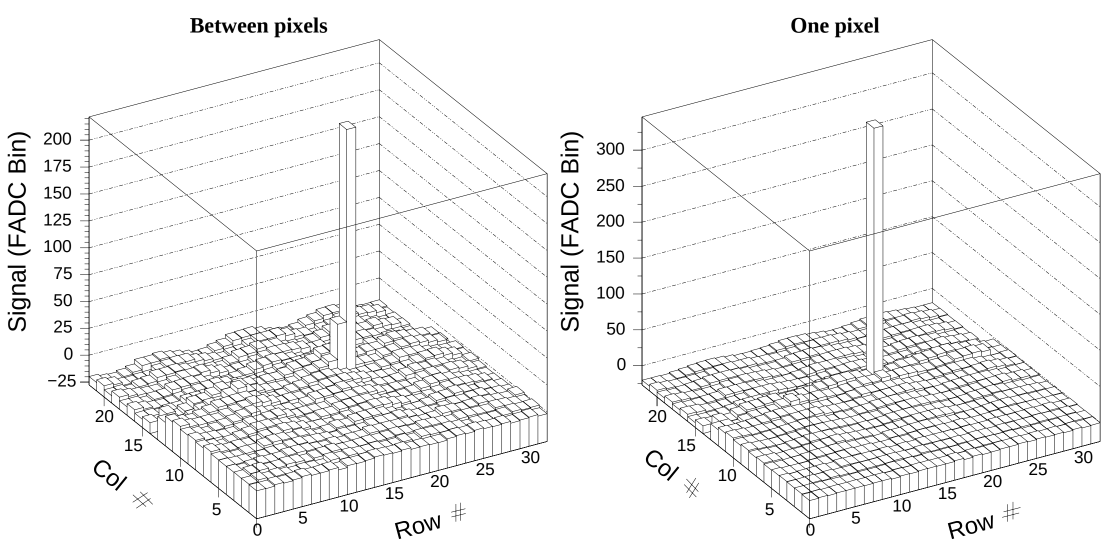

Figure 6.6: 3-D profile of the laser spot from Laser II, measured with a 22x32 Si pixel array with a pitch of 125 μm. The measurements were done at two different positions of the laser beam. At one setup the laser signal is spread over two pixels, while at the other setup the laser spot is focused on only one pixel.

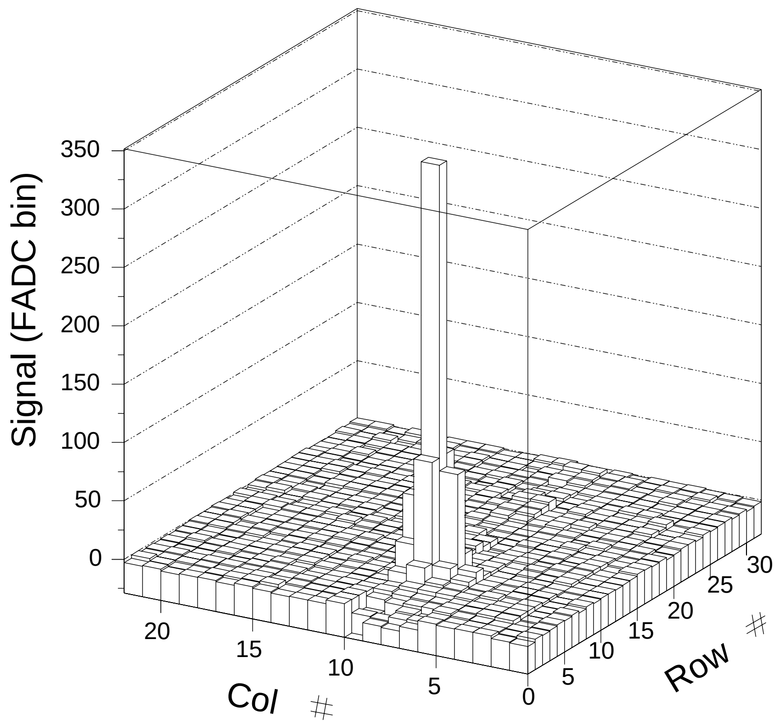

Figure 6.7: 3-D Profile of the laser spot from Laser III, measured with a 22x32 Si pixel array with a pitch of 125 μm.

6.1.6.4 Stability of Laser Output

Since no cooling system is designed for the laser diode, the stability of laser intensity have to be studied. This was done by measuring the laser signal at different time points. Figure 6.8 shows the result of such a measurement on Laser II over 4 1/2 hours. The first data were taken at 6 p.m. and the time difference between successive measurements was half an hour. All the following measurements on the pixel detector have taken less than that time period.

The measurement shows a variation of 14 FADC bins, which is about 4% of the average value of the signal. It can be concluded that the performance of the laser is quite stable during this time period. The stability of Laser III was also studied[65]; the fluctuation of the intensity was measured to be less than 10%.

6.2 Performance Parameters

In order to characterize a pixel detector, a set of performance parameters has to to be considered:

1. I-V Characteristic

2. full depletion voltage

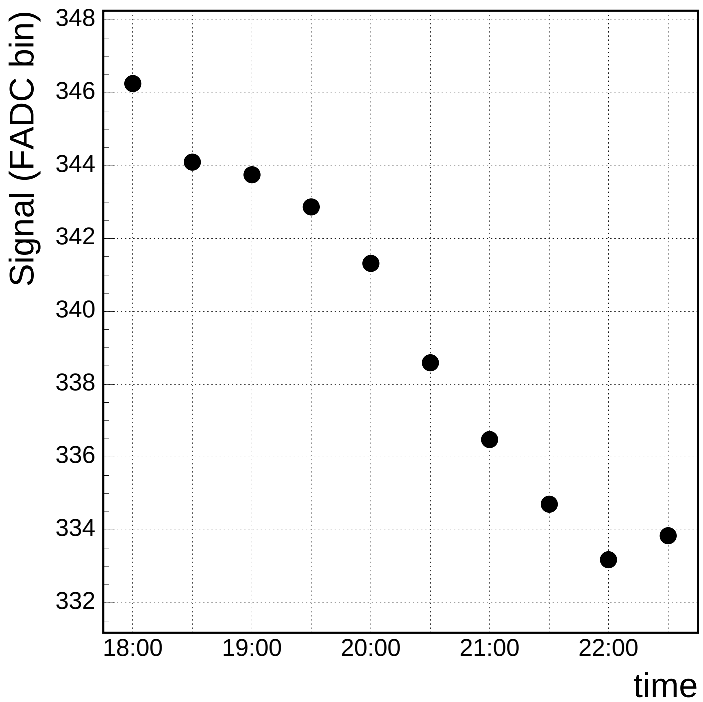

Figure 6.8: Measurement of the laser signal over 4 1/2 hours, measured with Laser II.

3. trim bits and threshold distribution
4. noise
5. pulse form, peaking time and time walk
6. linearity and gain
7. spatial resolution

They will be described in the following sections, together with the methods to measure them. The results of the measurements are presented in Section 6.3.

6.2.1 I-V Characteristic

The I-V characteristic, giving the dependence of the leakage current on the bias voltage, is an easy and quick way to check the functionality of a detector. It is always the first step in the whole characterization procedure.

To measure the I-V characteristics of a pixel detector, the backside of the detector has to be reversely biased. The frontside (i.e the structured side) of the detector has to be biased to ground potential via the bond pad and a p-type feedback transistor (which is also implemented on the AC30 chip). This is accomplished by applying the suitable voltages on the V_{ssana} and V_{rgpr} lines.

6.2.2 Full Depletion Voltage

Charge created in the neutral, non-depleted zone recombines with free-carriers and is lost. Therefore increasing the width of the space charge region increases the collected signal. The depletion zone width d_{Dep} can be expressed in terms of resistivity as[66]:

$$d_{Dep}(V_{bias}) = \sqrt{2 \cdot \varepsilon \cdot \mu \cdot \rho \cdot V_{bias}} \tag{6.1}$$

where ε is the dielectric constant and ρ is the specific resistivity of the detector material. μ is the majority carrier mobility. V_{bias} is the detector bias voltage.

To fully deplete a 250 μm thick n-type Si detector with a resistivity ρ of 7.4 kΩ·cm, one needs to apply a bias voltage V_{dep} =30 V.

Two methods can be employed to determine the full depletion voltage:

- by measuring V_{comp} as a function V_{bias} without charge injection
- by measuring the demanded laser intensity to reach a certain detection efficiency of the comparator as a function of V_{bias}

The first method will be discussed in the following section.

6.2.2.1 Control Voltage Vcomp in Dependence of Detector Bias Voltage

As mentioned in Chapter 3, V_{comp} is the control voltage of the global comparator threshold. Figure 6.9 (a) shows the threshold of pixel(5,20) measured for different values of V_{comp}. It can be seen that the pixel threshold increases linearly with the absolute value of V_{comp}.

At a defined detector voltage the absolute level of V_{comp} should be set as low as possible (V_{comp} has always a negative value) in order to obtain the lowest possible threshold; however, too low value of V_{comp} would cause fake hits from noisy pixels (such pixels have “hits” even when no charge is injected). The highest acceptable number of such noisy pixels is then used to define the suitable value of V_{comp}.

Figure 6.9 (b) shows the total number of noisy pixels in a double column as a function of V_{comp}. When the highest acceptable number of noisy pixels is set to be two(zero), V_{comp} is set to 2160 mV(2170 mV).

When V_{bias} exceeds the full depletion voltage V_{dep}, V_{comp} is expected to be stable in spite of the increasing detector voltage. When the detector voltage is much less than the full depletion voltage, the noise is much lower due to the smaller leakage current; therefore the absolute level of V_{comp} and consequently the comparator threshold are expected to drop with decreasing V_{bias}.

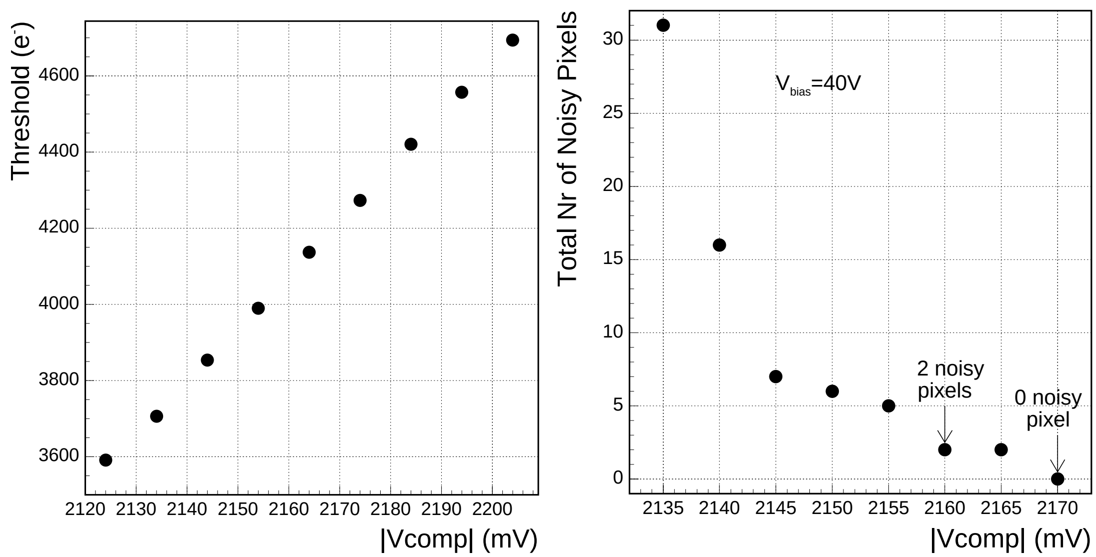

(a) Threshold as a function of Vcomp, measured on pixel(5,20).

(b) Total number of noisy pixels in a double column as a funtion of Vcomp.

Figure 6.9: V_{comp} as the control voltage of the global comparator threshold.

6.2.3 Trim Bits and Threshold Distribution

For the proper operation of the AC30 chip, one has to go through the following procedure:

1. Fix the value of V_{comp} by choosing the acceptable level of noisy pixels; switch off the noisy pixels by setting for them trim bits DTR=0.

2. Search for individual threshold with DTR=4 (middle of the available range) for all functional pixels by scanning the test pulses of different amplitudes. The comparator threshold of each pixel is supposed to have a distribution due to the electronic noise. In order to minimize this effect the threshold is defined as the input charge for which the comparator has a detection efficiency of 50%. Switch off the insensitive pixels whose comparators have no response to the test pulses of sufficiently high amplitude (¿ 30000 e^{-}) by setting for them DTR=8.

3. Search for the individual thresholds with an optimized set of trim bits. To do this the test pulse height is first set to be equal to the average value of the comparator thresholds, then scan the trim bits (DTR from 1 to 7) for each functional pixel, stopping the scan when the detection efficiency exceeds 50%. Upload the new set of the trim bits and map the threshold of each pixel by scanning the test pulses of different amplitudes again and check out whether the remaining pixels are functional.

6.2.4 Noise

The signal-to-noise ratio is a critical parameter for the CMS pixel detectors during the whole period of operation. Two factors affect the S/N ratio: the electronics and the detector itself.

The electronics noise ENC_1 is calculated as an equivalent noise charge (ENC) from the formula :

$$ENC_1^2 = A + B \cdot C^2 \tag{6.2}$$

where A and B are constants depending on the preamplifier(shaper) and C is the detector capacitance. In the case of the pixel detectors the main contribution to the electronics noise comes from the preamplifier(shaper); the capacitance of the pixel to the back plane, as well as the inter-pixel capacitance are kept very small.

The detector leakage current is another source of noise. The associated equivalent noise ENC_2 can be calculated with a simple model of a CR-RC filter. It is given as [67]:

$$ENC_2^2 = (\frac{e}{q})^2 \cdot \frac{qIT_p}{4} \tag{6.3}$$

where e is the base of natural logarithms, q is the electron charge, I is the diode leakage current and T_p is the peaking time. A leakage current of 100 nA per pixel would induce a noise of about 200 e^- with a peaking time of 25 ns.

The noise ENC ($ENC^2 = ENC_1^2 + ENC_2^2$) can be measured by a threshold scan (see Figure 6.10, the so called S-curve), in which the test pulse with increasing amplitude is injected into the pixel detector. The detection efficiency, defined as the fraction of the hits detected by the comparator, is modulated by the noise. A Gaussian noise distribution with mean value Q_o and standard variance σ ($\sigma \equiv ENC$) can be expressed as:

$$f(Q_s) = \frac{1}{\sqrt{2\pi\sigma^2}} exp[-\frac{1}{2}(\frac{Q_s - Q_o}{\sigma})^2] \tag{6.4}$$

So that the detection efficiency $P(Q_0)$ for an input charge $Q = Q_0$ is:

$$P(Q_0) = \int_{-\infty}^{Q_o} f(Q_s)\, dQ_s = 0.5$$

Detection efficiency $P(Q_1)$ for an input charge $Q_1 = Q_0 + \sigma$ is:

$$P(Q_1) = \int_{-\infty}^{Q_o+\sigma} f(Q_s)\, dQ_s = 0.84$$

By measuring the S-curve, ENC is evaluated as the increase of input charges which are needed to raise the detection efficiency from 50% to 84%.

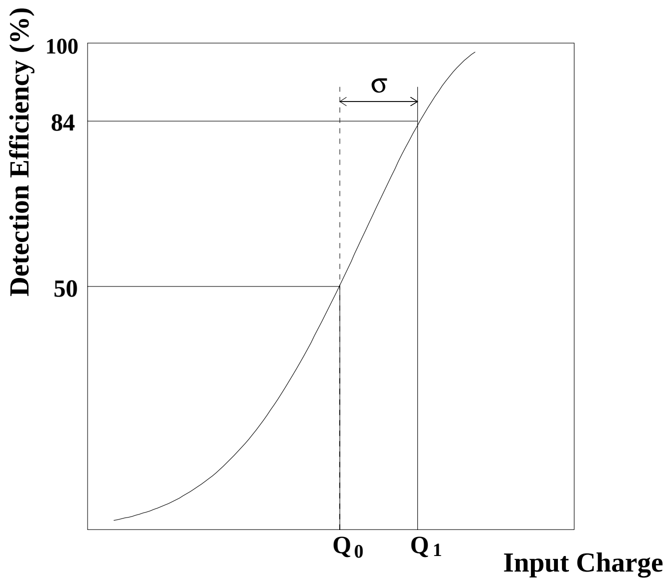

Figure 6.10: Determination of the noise $ENC \equiv \sigma$. It is given by the increase of input charges which are needed to raise the detection efficiency from 50% to 84%.

6.2.5 Pulse Form, Peaking Time and Time Walk

The pulse form of the signal is a very important characteristic of a pixel detector; it determines the performance parameters such as peaking time, time walk and gain factor of the readout electronics.

The pulse form at A_{out} is measured by varying the sampling time (i.e. the arrival time of the $HOLD$ signal), as illustrated in Figure 6.11. With the arrival of the $HOLD$ signal, the switch is opened so that the output of the shaper is then stored on the capacitance (see Figure 4.3).

The peaking time is determined as the time elapsed between the trigger and the signal maximum. The time walk is the time difference in the comparator response for large input charges and small input charges. The consequence of the time walk is the different sampling time between the large and small signals when the internal $HOLD$ signal is used. One can evaluate the time walk by comparing the pulse form between large (typically 20000 e^- $\sim$ MIP signal in a 250 μm thick Si sensor) and small signal (typically 2000 e^-), as shown in Figure 6.12.

6.2.6 Linearity and Gain

The gain is defined as the ratio of the output signal height to the input charge. In order to simplify the data analysis the detector readout electronics is normally designed to have a linear dependence between the two variables. For the CMS pixel detectors however, the situation turns out to be a little bit different. Due to the charge sharing between the pixels in a large magnetic field (4 T) at LHC,

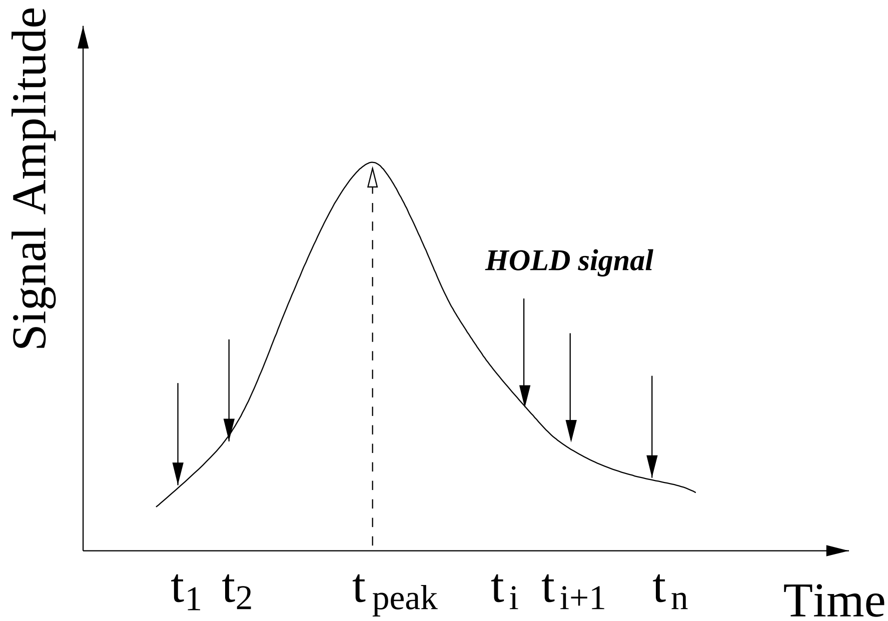

Figure 6.11: Measurement of the pulse form by varying the sampling time (i.e. the arrival time of the *HOLD* signal of the pixel readout electronics).

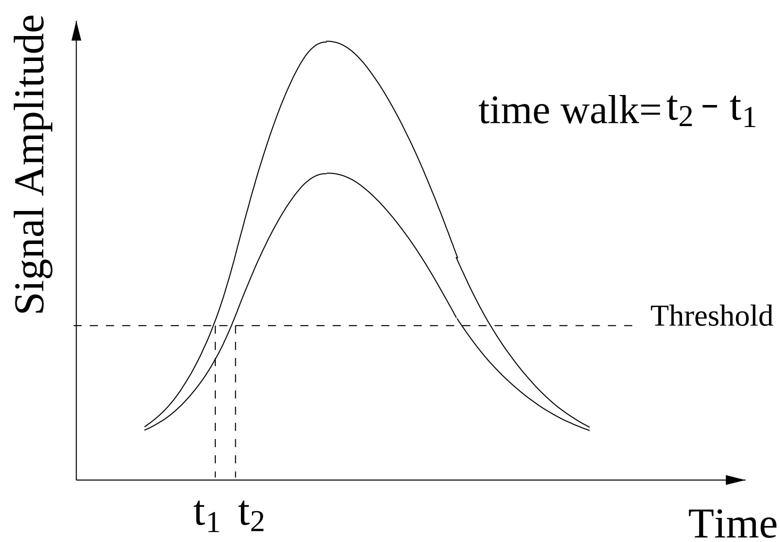

Figure 6.12: Measurement of the time walk by comparing the difference of the time needed to reach the threshold between large and small input charge.

small signal pulses are more frequent to appear than large ones. Therefore, the pixel electronics aims for a large gain for relatively small charge at the expense of non-linearity for the relatively large charge.

The gain characteristic of each pixel should be determined by a calibration run and the measurement can also show the homogeneity over the whole chip. The results for the final analogue output A_{out} will be given as follows. Measurements at the preamplifier and shaper outputs are presented in [68].

6.2.7 Spatial Resolution

The localization accuracy of a pixel detector depends on physical processes such as statistical fluctuations of the energy loss, diffusion of carriers during the drift, as well as external parameters like the pixel size and electronics noise[69].

When a particle traverses the sensor, the signal is usually spread over several pixels of the detector. The group of these pixels is called a cluster. To study the spatial resolution, one has to first consider the algorithms of cluster finding and position determination. These will be discussed in the following section. After the discussion, instrumentation to determine the resolution will be presented.

6.2.7.1 Algorithms of Cluster Finding and Position Determination

Different algorithms can be used to identify a cluster:

- Digital cluster finding algorithm (DIG-CFA)

  One searches for the pixel with the highest signal-to-noise ratio above a pre-defined value (the first selection criterion) in all available channels. The algorithm stops here and neglects all possible signals in neighboring pixels. The selected pixel is called the seed of the cluster. In this algorithm, the seed is of course the whole cluster.

  In the digital algorithm, the track position (x, y) is given by the center of the seed pixel. The maximum possible error is then half the pitch of the detector $\Delta x_{max} = \Delta y_{max} = p/2$; the spatial resolution $\Delta x = \Delta y$ is calculated to be:

$$\Delta x^2 = \frac{1}{p} \int_{-\frac{p}{2}}^{\frac{p}{2}} x^2 dx = \frac{p^2}{12} \qquad \Rightarrow \Delta x = \frac{p}{\sqrt{12}}$$

  With $p = 125\ \mu$m, the spatial resolution with a cluster size of one is 36 μm. This gives the spatial resolution for the worst case.

- Free size cluster finding algorithm (FS-CFA)

  There is no limit on the cluster size in this algorithm. The cluster is defined through the following procedure:

1. Similarly to the first step in the DIG-CFA, find the seed of the cluster according to the first selection criterion.
2. Check all eight neighboring pixels of the seed by comparing their signal-to-noise ratio to a given value (the second selection criterion). If none such pixels are found, the algorithm stops here and the cluster has a size of one pixel. Otherwise pixels whose ratio exceeds the cut are added to the cluster. The selected pixels are all considered as the seed of a cluster and the search is recursively repeated around the eight neighboring pixels until no pixels are found to meet the second selection criterion. Since the neighboring pixels usually contain a small fraction of the total signal, the second criterion is set lower than the first one.
3. The overall signal-to-noise ratio of the cluster has to exceed a given value (the third selection criterion). If this criterion is not fulfilled, the whole cluster is rejected.

- Dual cluster algorithm (Dual-CFA)

  This is the special case of the free size cluster finding algorithm. In this algorithm the cluster size is set to be two. After the first seed of the cluster has been found, the eight neighboring pixels are all checked to see whether their signal-to-noise ratio exceeds a given value (the second selection criterion). The pixel with the highest signal-to-noise ratio among the eight neighbors is added to the cluster.

  In dual and free size cluster finding algorithms the center of gravity (COG) method provides the simplest way to determine the track position. The COG method is based on the assumption that pulse height is linearly correlated to the distance of the passing particle from the pixel center, so that each point is assigned a weight proportional to the deposited charge, the coordinates (x, y) of the cluster are then given as:

$$x_{COG} = \frac{\sum_{cluster} S_i x_i}{\sum_{cluster} S_i} \tag{6.5}$$

$$y_{COG} = \frac{\sum_{cluster} S_i y_i}{\sum_{cluster} S_i} \tag{6.6}$$

where S_i are the individual pixel signals in the cluster and $(x_i,\ y_i)$ are the positions of the pixels in the defined coordinate system.

The values chosen for the cluster selection cuts depend on experimental conditions such as input charge, incident angle of traversing particle, magnetic field and detector performance. Generally they have to be set as low as possible in order to obtain a high detection efficiency, but on the other hand too low values of cuts could lead to a high ratio of fake clusters. Since the pixel detectors have a relatively low noise and the laser pulses usually have a high intensity, the occurrence of fake clusters in the laser beams is negligible.

The choice of cluster finding algorithms is also related to the experimental conditions. The digital algorithm is simple and fast, so it is usually used when very fast track finding is required. The more complicated free cluster finding algorithm produces accurate information, but it consumes more time and suitable values for the selection criteria have to be applied. It should certainly be used when high cluster sizes are expected. The dual cluster algorithm is a compromise between the two.

Provided that the laser spot size is of the order of 100-500 μm, the possibility that the signal is spread over more than two pixels is high. The free cluster finding algorithm will therefore be employed for the analysis of the laser data.

6.2.7.2 Measurement of Spatial Resolution

To determine the spatial resolution with the laser pulses, the distribution of the residuals has to be measured. The residual is defined as the difference between the measured position (x_{det}, y_{det}) given by the detector signals and the defined position (x_{stage}, y_{stage}) given by the coordinates of the x-y-z stage, which can be read out from the PC. One has: $\Delta_x = x_{det} - x_{stage}$ and $\Delta_y = y_{det} - y_{stage}$.

With the x-y-z stage one can move the laser spot to measure residuals at various positions on the detector. One can also do the measurements at one fixed position, thus having a defined cluster size distribution. There are several differences between the test beam and laser measurements:

- Due to the effect of δ-electrons, the distribution of the cluster charge in a beam test is not Gaussian and the most probable cluster charge is evaluated, while in a laser test the Gaussian distribution is expected.
- In a beam test, one has to take account of multiple scattering to determine the resolution. This is not needed for the laser pulses.
- It is possible to fix the position of initial charge injection with the laser system, so that the cluster size distribution is fixed.

When the position of the laser is not moved, events can be sorted according to the cluster size. Assuming that for a cluster size c the fitted Gaussian distribution of the cluster charge has a mean value S_c and a standard deviation σ_{s_c}, the mean cluster charge over clusters of all sizes is evaluated as:

$$S = \frac{\sum_c \frac{S_c}{(\sigma_{s\_c})^2}}{\sum_c \frac{1}{(\sigma_{s\_c})^2}} \tag{6.7}$$

Similarly, the cluster noise is determined as:

$$(N)^2 = max(\frac{\sum_c (\frac{S_c - S}{\sigma_{s\_c}})^2}{\sum_c (m-1)\frac{1}{(\sigma_{s\_c})^2}}, \frac{1}{\sum_c \frac{1}{(\sigma_{S\_c})^2}}) \quad (6.8)$$

where m is the total number of different cluster sizes. The x-residual is given as:

$$x_{res} = \frac{\sum_c \frac{x_c}{(\sigma_{x\_c})^2}}{\sum_c \frac{1}{(\sigma_{x\_c})^2}} \quad (6.9)$$

where x_c and σ_{x_c} are the mean value and standard deviation of the x-residual distribution for events with a cluster size c. For events with cluster size one, the digital resolution of 36 μm is used for the calculation. The x-resolution is then evaluated as:

$$(\sigma_x)^2 = max(\frac{\sum_c (\frac{x_c - x_{res}}{\sigma_{x\_c}})^2}{\sum_c (m-1)\frac{1}{(\sigma_{x\_c})^2}}, \frac{1}{\sum_c \frac{1}{(\sigma_{x\_c})^2}}) \quad (6.10)$$

Considering both x and y coordinates, the resolution is defined as:

$$\sigma^2 = \sigma_x^2 + \sigma_y^2$$

6.3 Results of Measurements

After the discussion of the performance parameters of the pixel detector, the measurement results will be presented in the following sections:

6.3.1 I-V Characteristic

Figure 6.13 gives the I-V characteristic of the Si pixel detector. As expected, the leakage current increases as the detector voltage rises. At a voltage of 65 V, the current is below 100 nA. The measurement shows a reasonable I-V characteristic of the detector.

6.3.2 Full Depletion Voltage

6.3.2.1 Control Voltage Vcomp in Dependence of Detector Bias Voltage

Figure 6.14 (a) shows the level of V_{comp} as a function of the detector bias voltage V_{bias}. The measurement shows that the detector is fully depleted when V_{bias} is above 34 V.

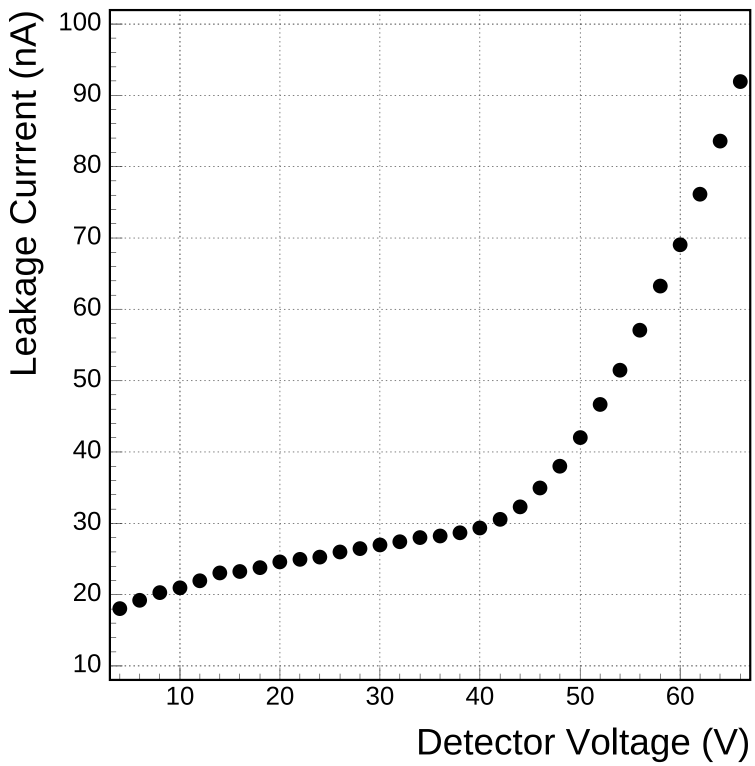

Figure 6.13: I-V Characteristics of a Si pixel sensor bonded to an AC30 chip.

6.3.2.2 Measurement with Laser I

Like the test pulse, the laser pulse needs to have sufficiently high intensity to reach 100% detection efficiency of the pixel, otherwise the detection efficiency decreases with decreasing intensity. Figure 6.14 (b) shows the demanded laser voltage (as a measure of laser intensity) in dependence of detector voltage to obtain a detection efficiency of 50%. The required laser intensity drops significantly as the depletion of the detector increases over its whole thickness and it remains constant after the full depletion. The full depletion voltage is about 30 V; the value is comparable to that from the previous measurement of V_{comp}.

6.3.3 Trim Bits and Threshold Distribution

Figure 6.15 shows the distribution of trims bits measured with the test pulses. The distribution peaks around trim bits DTR=4 and DTR=5. There is a considerable number of insensitive pixels (DTR=8), most of them are located in the outermost rows and/or columns of the chip. The main contribution to the insensitive pixels is the defective bump bonding between the sensor and the readout chip. Mechanical deformation while handling could be the reason of the damage.

Figure 6.16 shows the threshold distribution for two different sets of trim bits. It is seen that the distribution becomes narrower and is much better represented

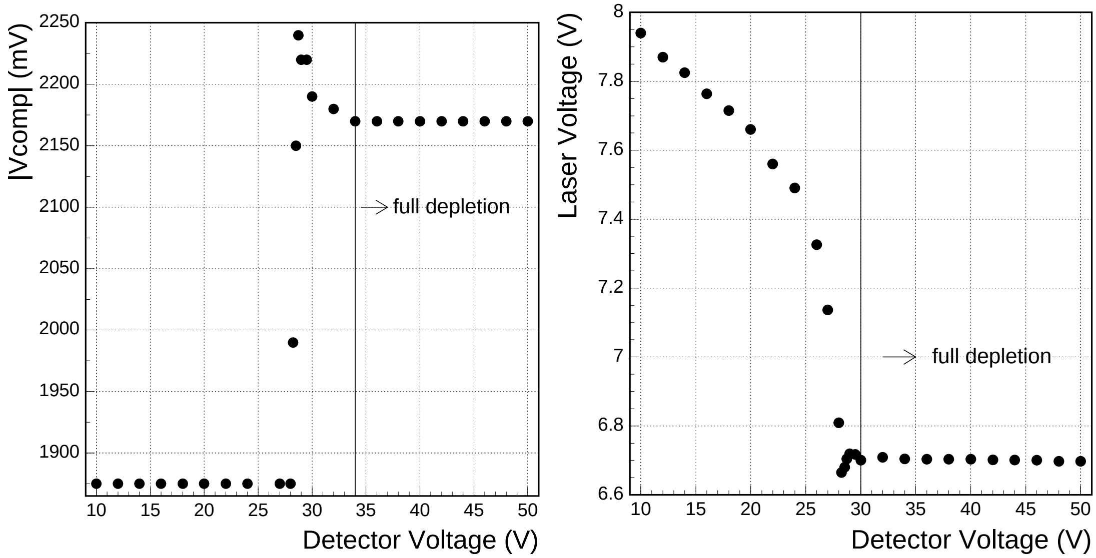

(a) V_{comp} in dependence of detector bias voltage.

(b) Laser voltage as a function of detector bias voltage, measured with Laser I.

Figure 6.14: Measurement of full depletion voltage.

by a Gaussian function with the DTR configuration shown in Figure 6.15. The average threshold of all functional pixels is (3710±157) e^- with the optimized DTR configuration, which is much lower than that with DTR=4 for all pixels.

6.3.4 Noise

Figure 6.17 shows the S-curve for pixel(6,20) and pixel(7,20) measured with the test pulses. The noise of pixel(5,20) is determined to be (135±34) e^-. Pixel(7,20) has a lower noise of (105±38) e^-.

6.3.5 Pulse Form, Peaking Time and Time Walk

6.3.5.1 Measurement with Test Pulses

Figure 6.18 shows the pulse forms with the test pulses of different amplitudes. The peaking time is in the range of 30-41 ns. The measurements demonstrate that the peaking time is different for large and small input charges. The difference is about (5.0±1.4) ns for an input charge variation between 5000 e^- and 20000 e^-.

It can be seen from Figure 6.18 that the difference of the response time between the input charge of 5000 $e^-$and 20000 e^- is about 5.0 ns (the comparator threshold is set to 2000 e^- , i.e. $\sim$ 20 FADC bins).

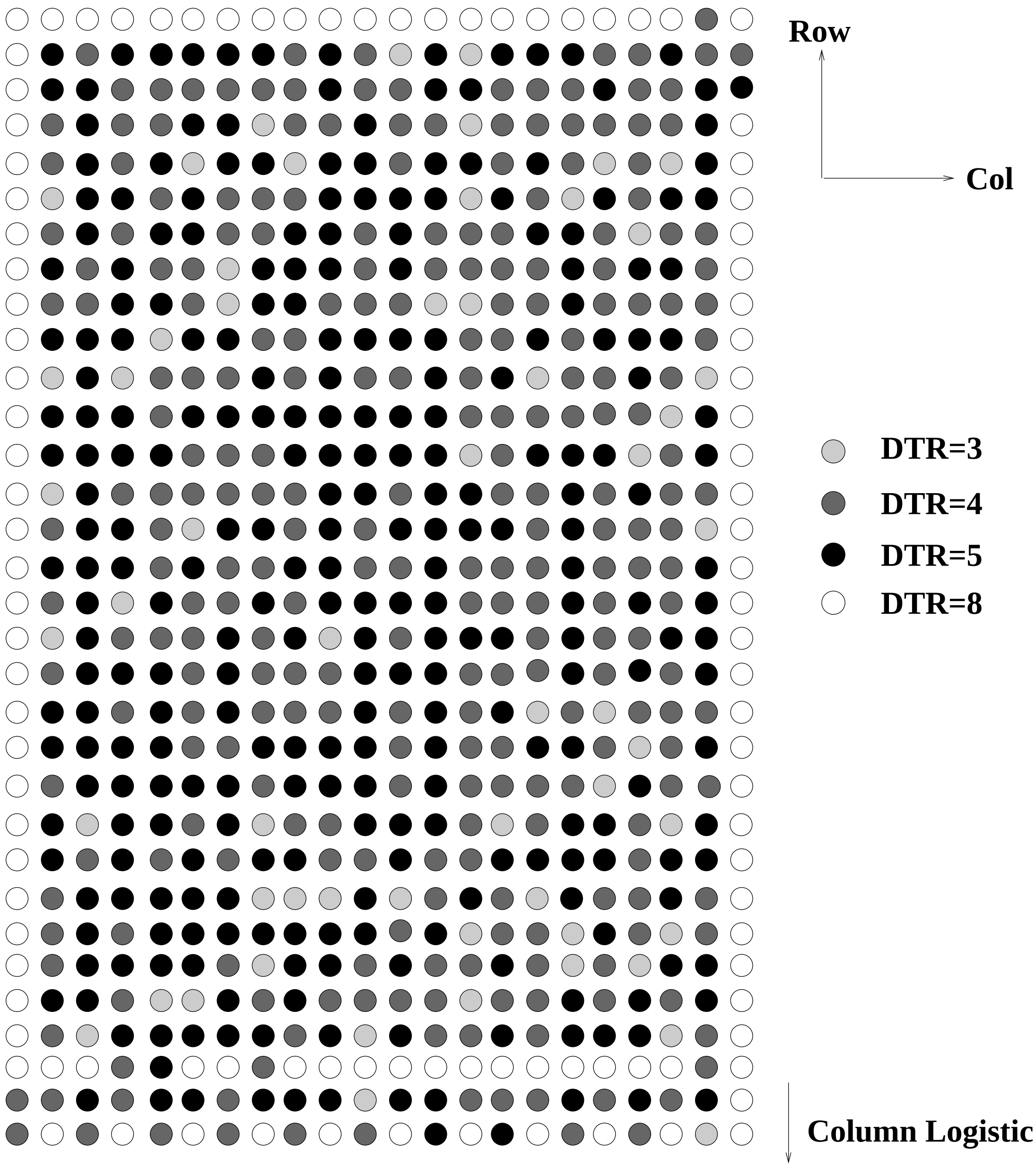

Figure 6.15: Set of trim bits (DTR). Most of the insensitive pixels are scattered around the borders of the detector.

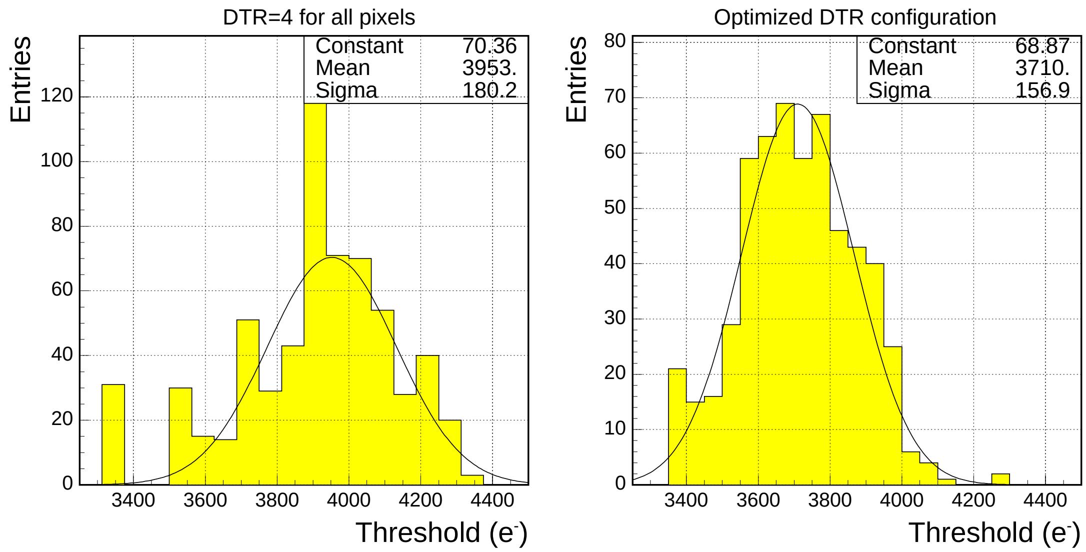

Figure 6.16: Threshold distribution for two different sets of trim bits. One set refers to trim bits DTR=4 for all pixels, while the other is the optimized configuration shown in Figure 6.15.

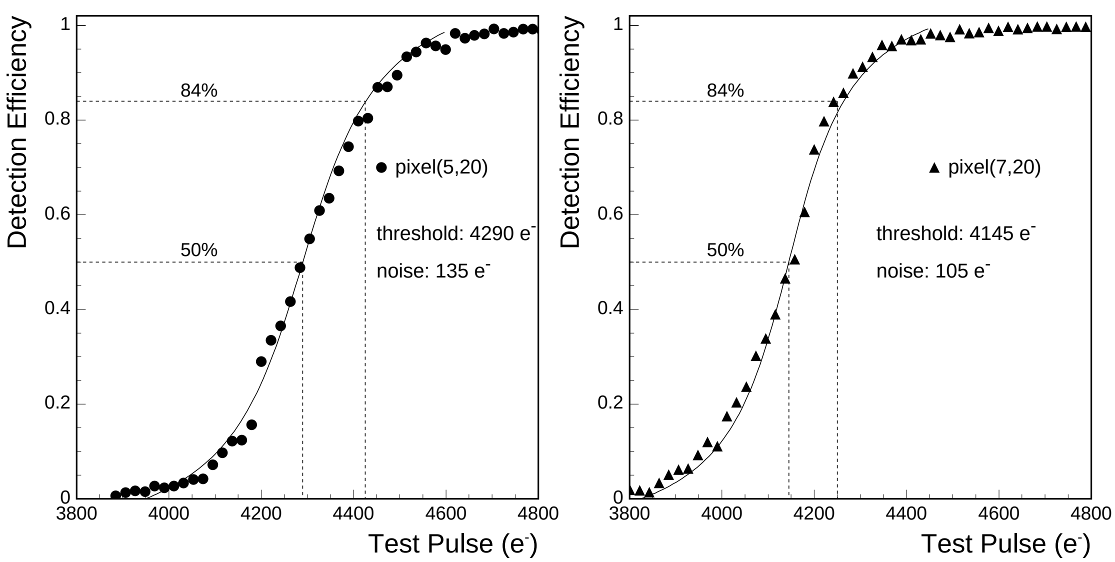

Figure 6.17: Detection efficiency as a function of test pulse height, measured at two different pixels (solid curves are the fits to the data).

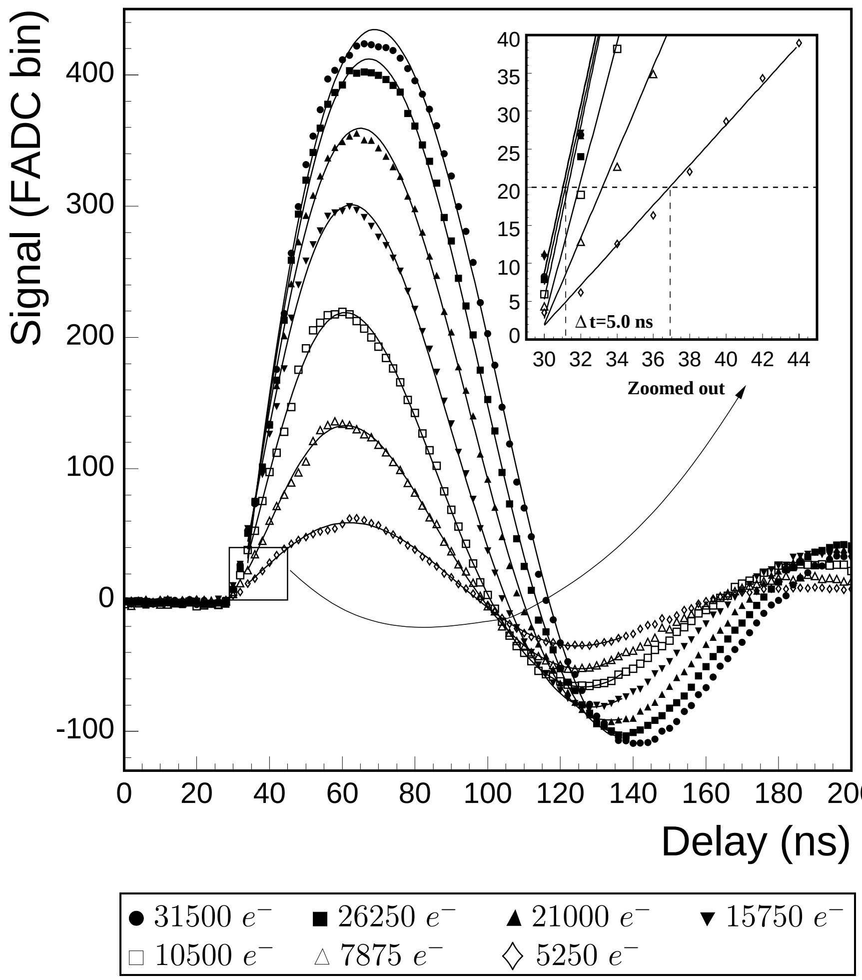

Figure 6.18: Pulse form of A_{out} measured with the test pulses of different amplitudes (solid curves are the fits to the data, V_{bias}=40 V).

6.3.5.2 Measurement with Laser Pulses

Figure 6.19 shows the result of the pulse form measurements with Laser II. The laser spot is focused on pixel(5,20). The peaking time is evaluated to be 44 ns. The reason why the value is different from that from the previous measurements with the test pulses is the pulse length of the laser (also see the zoomed picture in Figure 6.19). From the measurement of the oscilloscope, the pulse length of the laser is $\sim$ 10 ns. Therefore it takes more time to integrate the signal. The difference of the response time between the large (20000 e^-) and the small input charge (7000 e^-) is measured to be 7.4 ns.

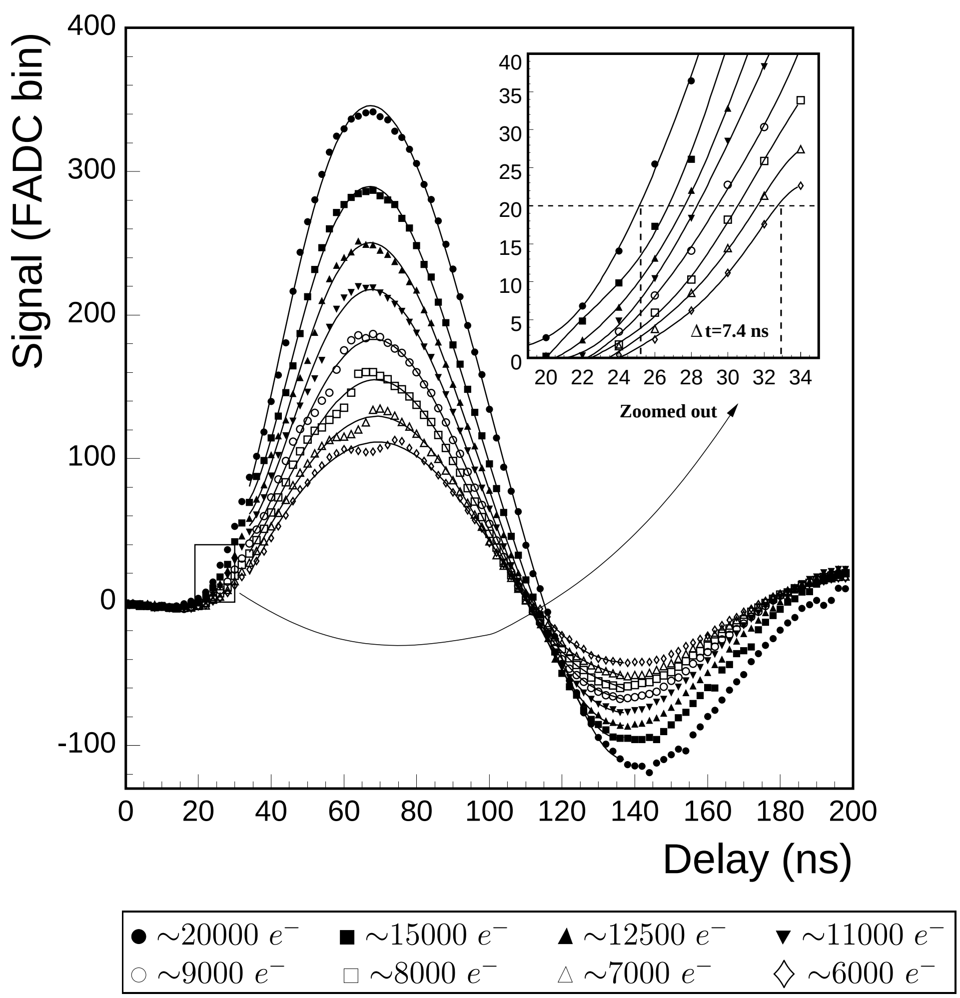

Figure 6.19: Pulse form of A_{out} measured with Laser II. The laser spot is focused on pixel(5,20) (solid curves are the fits to the data, V_{bias}=40 V).

6.3.6 Linearity and Gain

6.3.6.1 Measurement with Test Pulses

Figure 6.20 (a) shows the gain factor measured for three different pixels. As expected the gain is linear only for small input charges. In the range from 5000 e^- to 10000 e^- the gain of the three pixels is identical; it is evaluated as 33 e^-/FADC bin. When the input charge increases above 0.5 MIP, the gain factors become nonlinear and they are different for different pixels. It is therefore important to calibrate each pixel before data taking.

6.3.6.2 Measurements with Laser Pulses

Characteristics like gain and linearity were also studied with the laser pulses. To do the measurement the laser spot must be focused on only one pixel. This is possible to do with Laser II. The results are shown in Figure 6.20 (b).

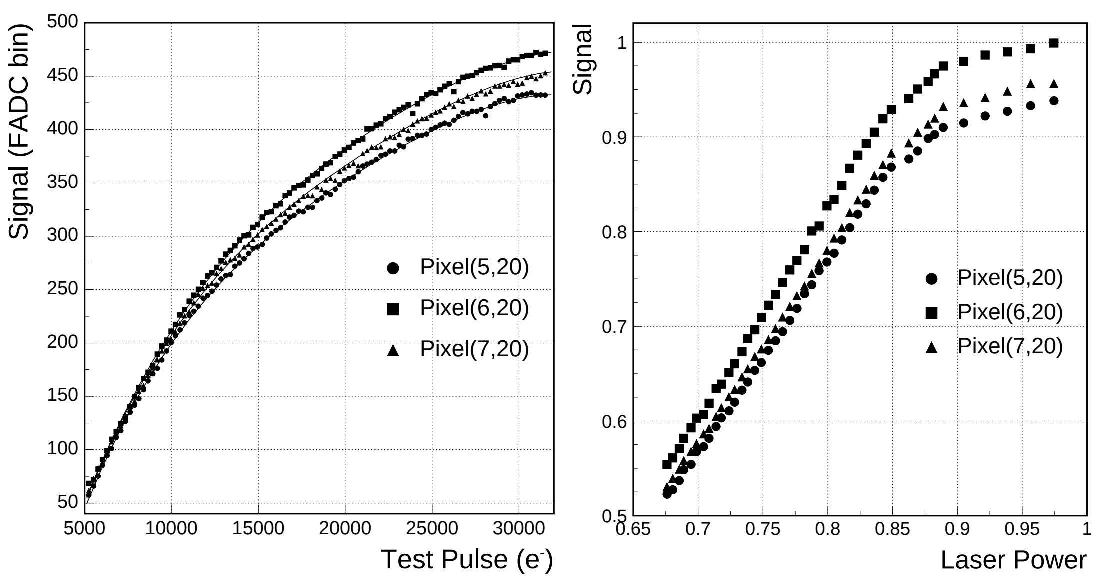

Figure 6.20: Linearity and gain factor measured for pixel(5,20), pixel(6,20) and pixel(7,20). The laser power is measured by a power meter; the values are normalized by setting the maximum laser power to 1, as well as the signal height measured with the laser pulses.

It can be seen that the results are similar with those from the test pulse measurements: pixel(6,20) has the maximum gain factor, pixel(7,20) the next, and pixel(5,20) has the lowest gain factor. The measurements also show that the amplifier saturates for large signals. However, it is impossible to compare the results quantitatively without an accurate calibration of the laser intensity.

6.3.7 Cluster Size, Cluster Charge and Spatial Resolution

I measured the cluster size, cluster charge and spatial resolution with four different configurations. Their specifications are listed in Table 6.3. The results are presented and discussed in the following sections.

configuration	Laser II 670 nm laser diode	Laser III 1064 nm Nd:YAG
unmoved x-y-z stage	A	B
moving x-y-z stage	C	D

Table 6.3: Four configurations to measure the cluster size, cluster charge and spatial resolution.

6.3.7.1 Configuration A: Laser II, x-y-z stage unmoved

Figure 6.21 shows the results of the cluster charge and x-resolution when the x-y-z stage is not moved. 10000 laser pulses were sent during the measurement. The mean cluster size is 3.93. The x-resolution σ_x given by the distribution of the residuals is determined to be 1.96 μm.

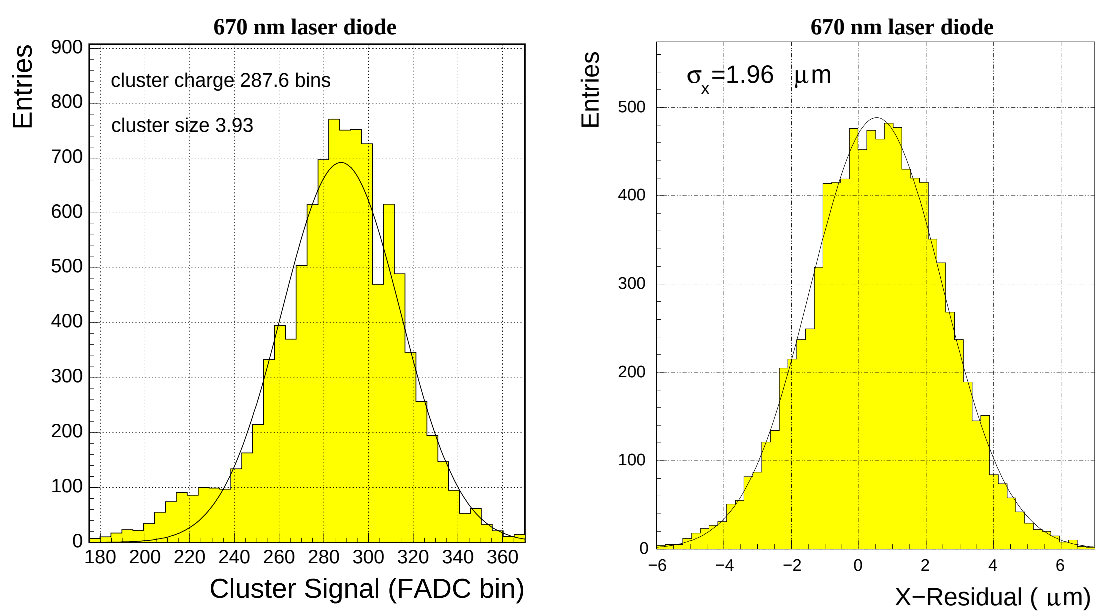

Figure 6.21: Cluster size, cluster charge and resolution measured in Configuration A.

Figure 6.22 shows the results from the same kind of measurement but at a different position of the laser spot. At this position the spot is spread over several pixels, while only a small amount of the signal is covered by one of these pixels. The detection efficiency of this pixel is below 100% due to the relative high noise and comparator threshold. As a result the signal is detected by 3 pixels for more than half the events, while for the other events the signal is found to be distributed over 4 pixels. Only a few events have a cluster size of 2.

Both the distribution of the cluster charge and that of the residuals can be described as a combination of two Gaussian functions corresponding to the different cluster size. The mean cluster size is calculated to be 3.47. The cluster charge is determined as 169.8 bins (see Section 6.2.7.2). The resolution is 7.52 μm in the x-direction and 7.03 μm in the y-direction; both are comparable to each other.

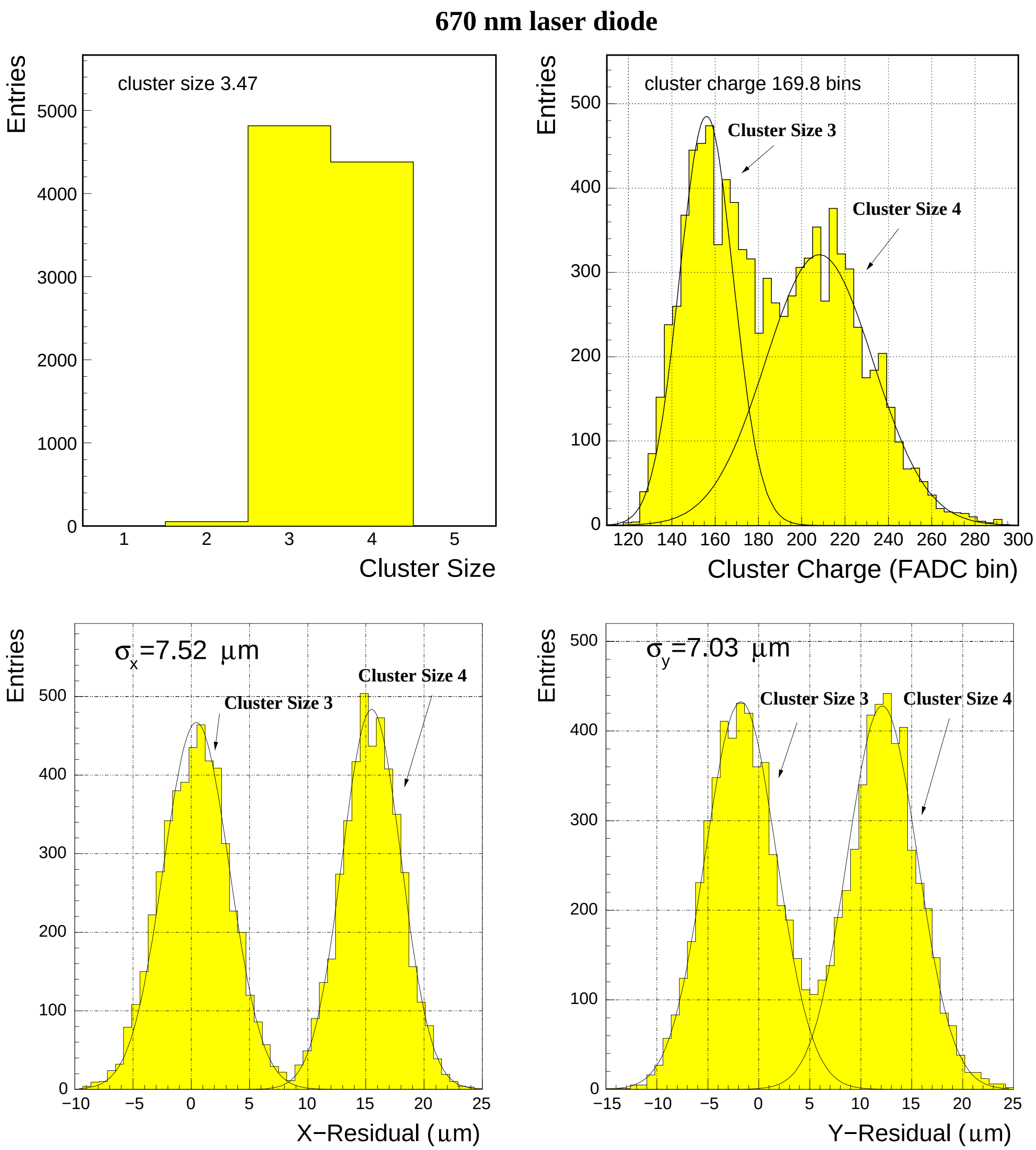

Figure 6.22: Cluster charge and resolution measured in Configuration A.

Figure 6.23 shows the dependence of the resolution on the cluster signal-to-noise ratio with a defined cluster size. It can be seen that the resolution improves as the cluster S/N ratio increases from 10 to 20. At high S/N ratio the resolution is little different between the cluster size of 3 and 4.

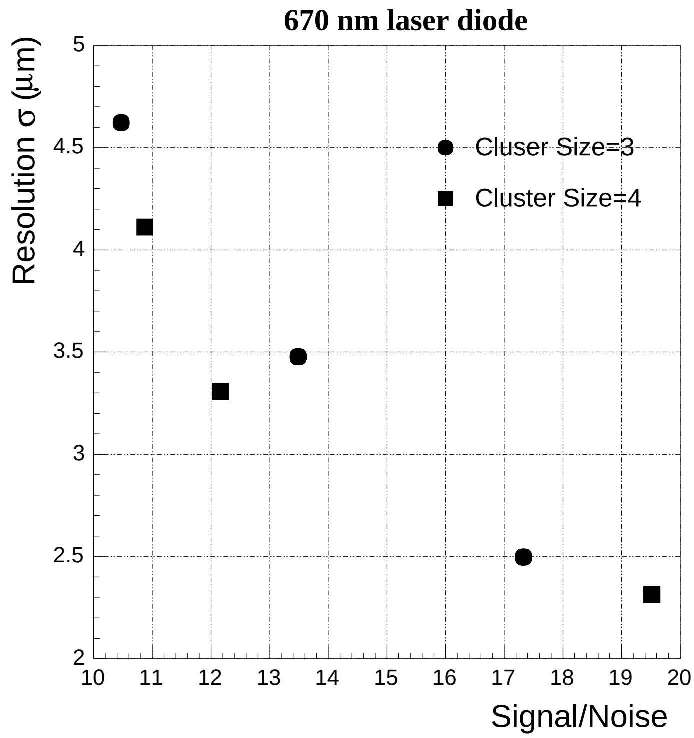

Figure 6.23: Resolution σ (defined as $\sigma = \sqrt{\sigma_x^2 + \sigma_y^2}$) in dependence of signal-to-noise ratio, measured in Configuration A.

6.3.7.2 Configuration B: Laser III, x-y-z stage unmoved

Similar to Configuration A, 10000 pulses from the Nd:YAG laser were sent to the sensor while the laser spot was fixed at one position. Figure 6.24 shows the results of such a measurement. The mean cluster size is 3.00. The resolution is determined as 0.99 μm, which is better than that of Configuration A. The main reason is the much higher S/N ratio.

Figure 6.26 shows the result of the same kind of measurement but with the laser spot at a different position. As discussed above, some events are found to have a cluster size 3, while a small amount of events have a cluster of 4. The mean cluster size is evaluated to be 3.31, the cluster charge is 492.3 bins. The resolution is 3.24 μm in the x-direction and 3.99 μm in the y-direction. Similarly to Configuration A the resolution in x- and y-direction are comparable to each other. The better value of the spatial resolution than that of Configuration A can also be explained with the much higher cluster S/N ratio.

Figure 6.25 shows the spatial resolution σ in dependence of cluster size. A significant improvement of the resolution is archived when the cluster size increases from 2 to 3.

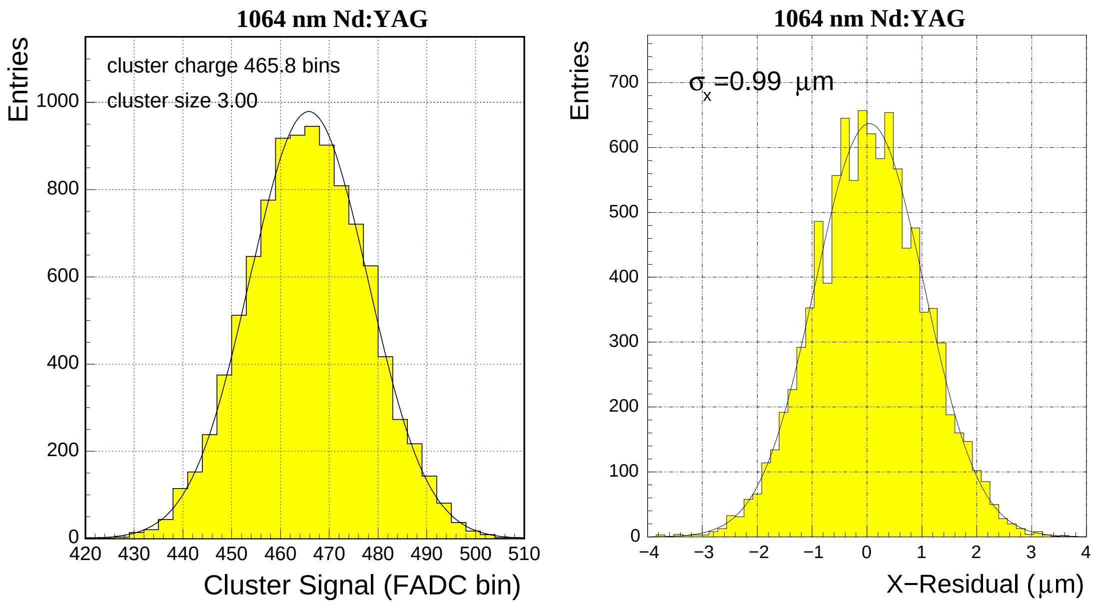

Figure 6.24: Cluster signal and spatial resolution measured in Configuration B.

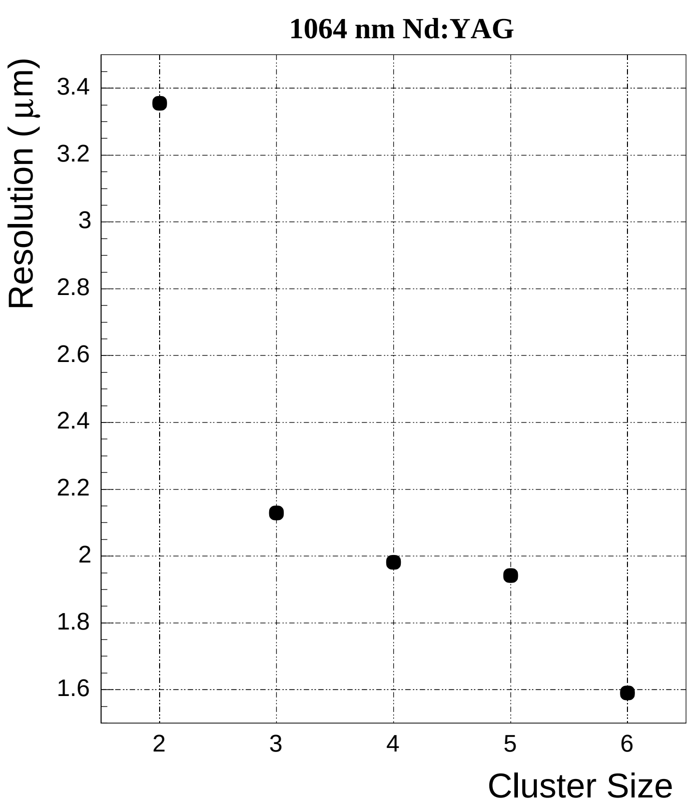

Figure 6.25: Spatial resolution in dependence of cluster size, measured in Configuration B.

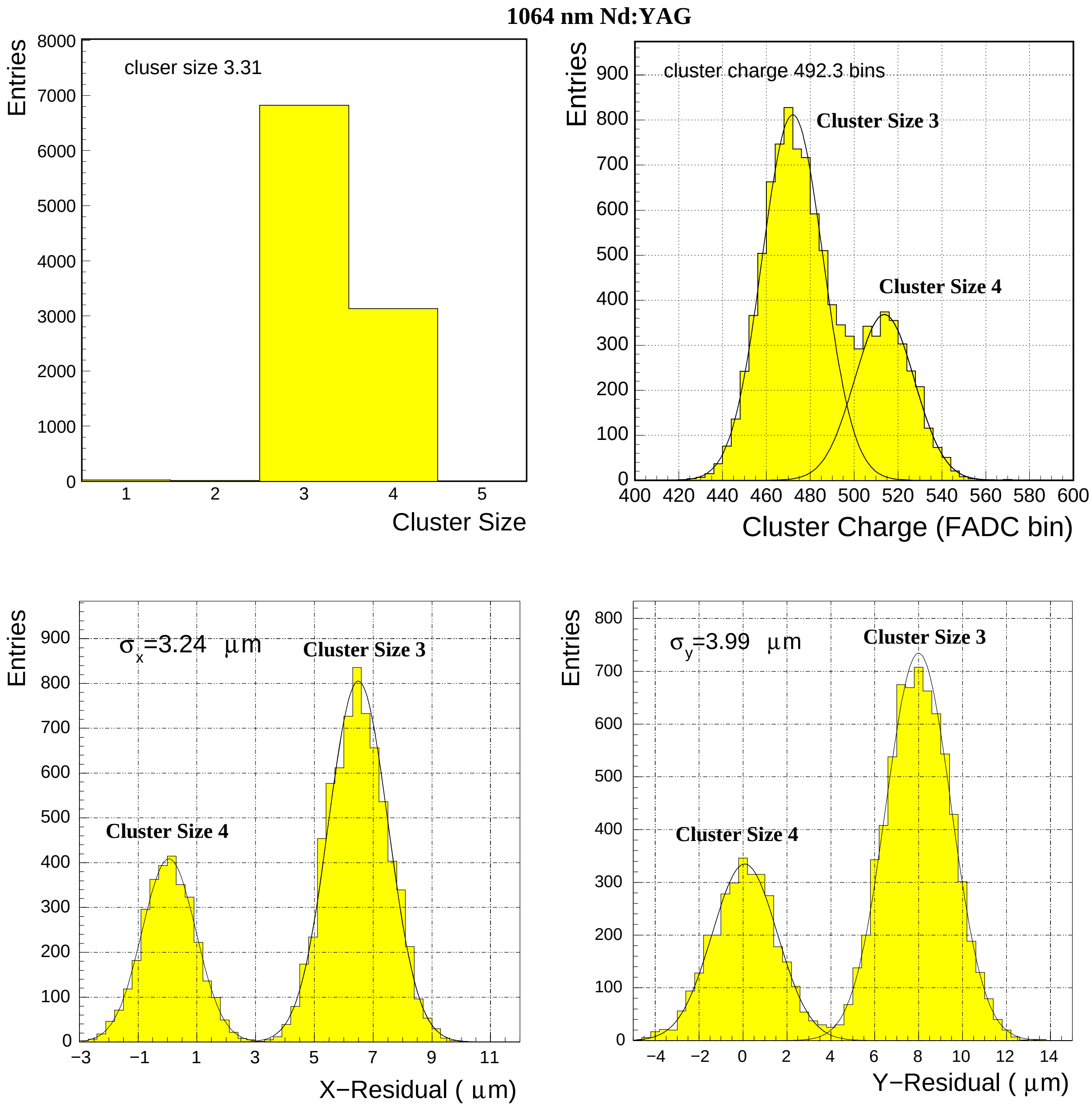

Figure 6.26: Cluster size, cluster signal and resolution measured with Laser III in Configuration B.

6.3.7.3 Configuration C: Laser II, x-y-z stage moved

Figure 6.27 (a) shows the signal distribution for pixel(6, 45) as the laser spot from Laser II is moved in the x-direction (along the pixel columns) in steps of 0.5 μm. As expected, the signal rises as the center of the spot approaches the pixel and then declines as the spot moves away. The spot size (FWHM) is measured to be about 100 μm.

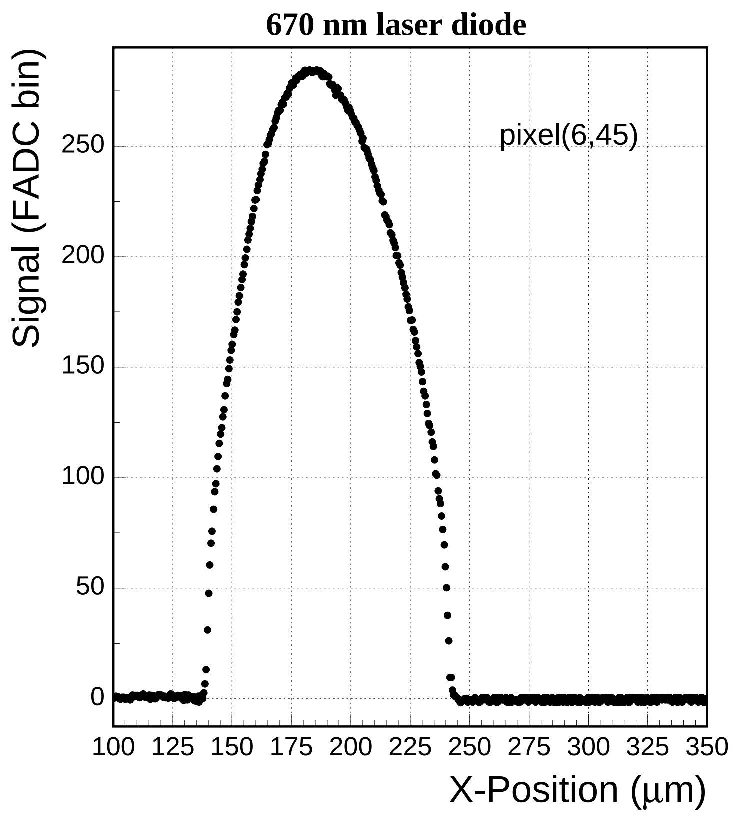

Figure 6.27: Signal of a pixel with the laser scanning the columns (Configuration C).

Figure 6.28 shows the cluster charge in dependence of laser position, together with the geometry at three selected positions. The cluster charge shows a certain pattern at different laser positions. The distance between the two neighboring minima (position 1 and 3) is about 125 μm, which is exactly the pixel pitch. At position 1 and position 3 the signals are mainly shared by two pixels; at position 2 however, the signal is dominantly received by only one pixel.

It can be seen from the pulse form of A_{out} that signals can be lost when the sampling time is not exactly the same as the peaking time (see Section 6.2.5 and Section 6.3.5). Due to the time walk the sampling time is different for small and large input charges when the internal $HOLD$ signal is used. When the sampling time is adjusted for large signals, a certain amount of small signals are therefore lost. That is why the detected cluster charge is dependent on the position of the laser spot and it reaches its maximum when the laser is focused on only one pixel.

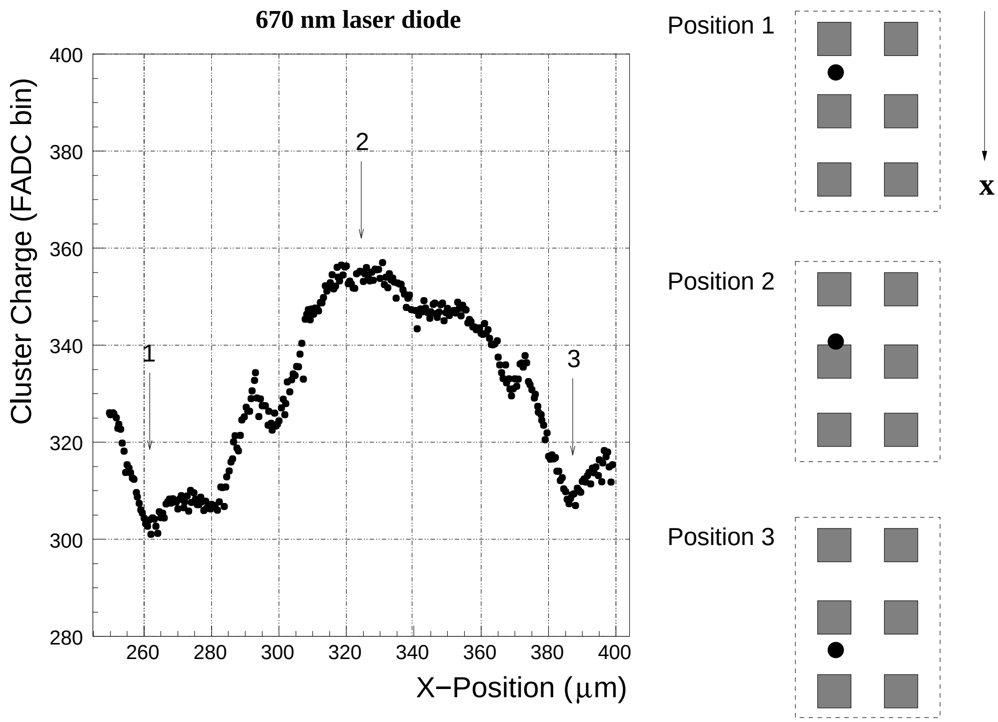

Figure 6.28: Cluster charge in dependence of laser position (Configuration C). Right-side picture shows the geometry of the laser spot at three different positions (squares represent the pixels; circles represent the center of the laser spot).

Figure 6.29 shows the measured residual in x-direction. The x-resolution is determined to be 3.55 μm.

6.3.7.4 Configuration D: Laser III, x-y-z stage moved

Figure 6.30 shows the signal distribution for pixel(5, 10) as the laser spot from Laser III is moved in the x-direction (along the pixel columns) in steps of 1.0 μm. The spot size (FWHM) is measured to be about 200 μm.

Figure 6.31 shows the residual of the reconstructed x-position. The cluster charge has a mean value of 604.1 FADC bins. The mean cluster size is 3.80 and the x-resolution is evaluated as 2.75 μm. The better value than that with Laser II (see Figure 6.29) is mainly due to the much higher S/N ratio.

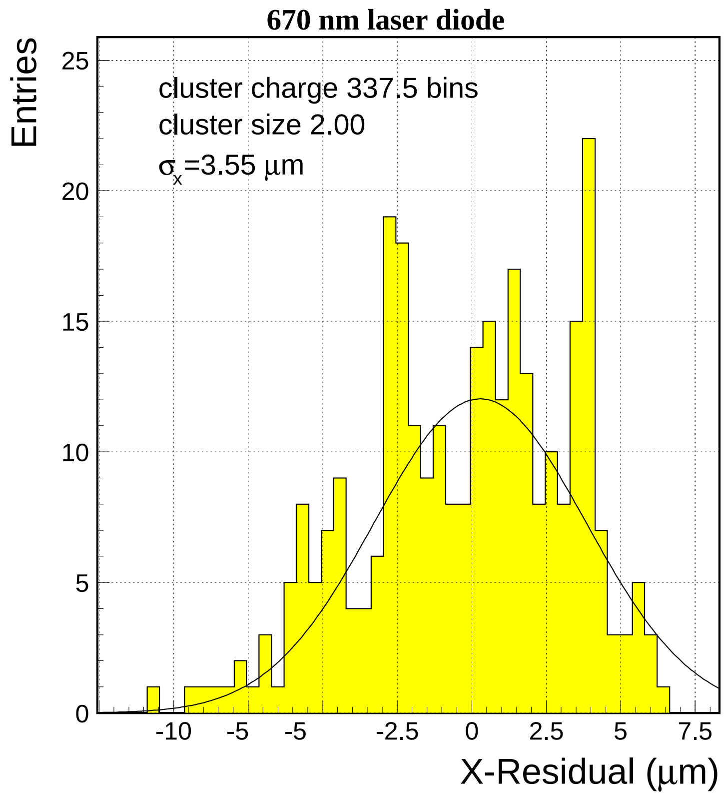

Figure 6.29: Spatial resolution measured in Configuration C.

6.4 Summary

The CMS pixel detector prototype was characterized with the test and laser pulses. The results described in this thesis can be summarized as follows:

- Detector leakage current: ¡ 100 nA up to a detector voltage of 65 V.
- Full depletion voltage: 34 V(30 V) according to the test(laser) pulse measurement.
- The average of the trim bits distribution (used for the individual adjustment of comparator threshold) is 4.91. Insensitive pixels are mostly located in the outermost rows and/or columns of the chip.
- Threshold: average value 3710 e^- with a standard deviation of 157 e^-.
- Noise: average value is (120±36) e^-.
- Peaking time: in the range of 30-41 ns according to the measurement with the test pulses with a difference of about (5.0±1.4) ns between input charge 5000 e^- and 20000 e^-.

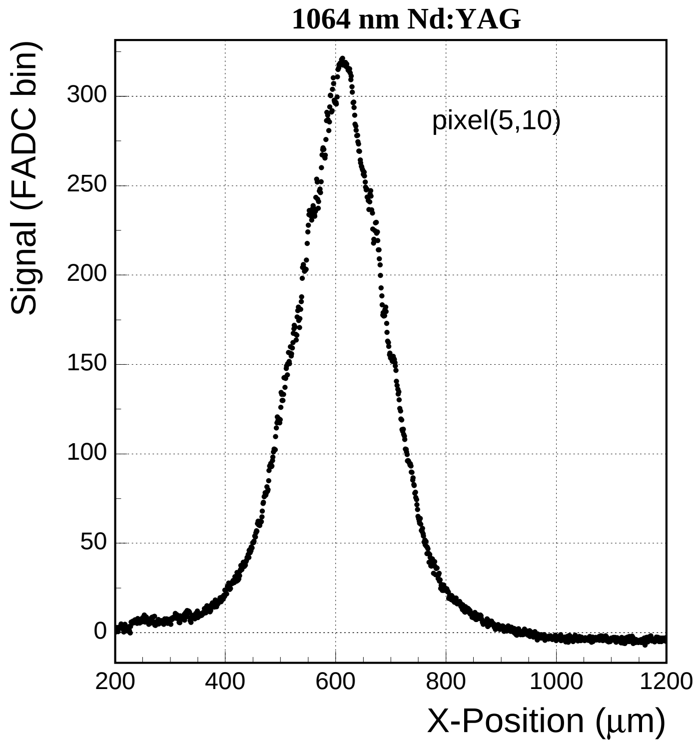

Figure 6.30: Signal of one pixel with the laser scanning the columns (Configuration D).

A peaking time of 44 ns was measured with the laser pulses. The discrepancy of the two measurements is caused by the length of the laser pulses, which is about 10 ns.

- Time walk: 5.0(7.4) ns measured with the test(laser) pulses.
- Good linearity and homogeneity of the analogue output signal was measured with the test pulses up to an input charge of 10000 e^-. The measurements with the laser pulses show the same pattern of behavior for the pixels. However, it is impossible to compare the results quantitatively without an accurate calibration of the laser intensity.
- Gain: 33 e^-/FADC bin up to an input charge of 10000 e^- according to the measurements with the test pulses.
- The spatial resolution was determined with the laser pulses by studying the distribution of the residuals. The results with the fixed laser positions are comparable between the measurements with a 670 nm laser diode and 1064 nm Nd:YAG.

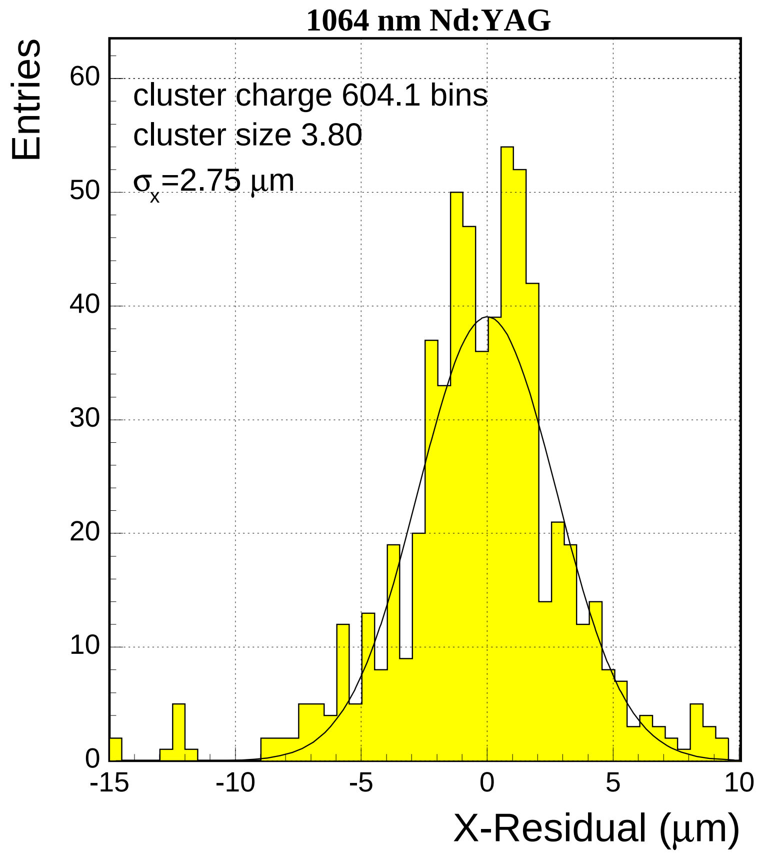

Figure 6.31: Spatial resolution measured in Configuration D.

It has been proved that high signal-to-noise ratio enhances the resolution. The resolution is also improved when the cluster size changes from 2 to 3; however the improvement is less significant when the cluster size is above 3. The resolution in x- and y-direction have been measured to be comparable to each other. With a cluster size of 3 a resolution of about 2.1 μm can be achieved.

A worse value of the resolution was measured with the moving x-y-z stage. This is caused by the much higher systematic errors than that with the unmoved x-y-z stages. Main contributions to the errors are the time walk and uncertainties on the alignment between the coordinate systems of the stage and the detector.

Chapter 7

Conclusion

This work concentrates on the characterization of the CMS Si pixel detector prototype. The prototype has in total 704 pixels, which are arranged in a 22x32 array. Each sensor pixel with a size of 125×125 μm^2 is connected via a solder bump to a pixel unit cell on the AC30 chip. An analog readout scheme in radiation hard technology is implemented on the chip .

The CMS pixel detector uses silicon as the baseline material, whereas GaAs was the candidate material. Before studying the detectors with the laser pulses, photon absorption was measured in both materials in the near infrared region up to a wavelength of 1100 nm. At λ=1064 nm the absorption in Si with a thickness of 250 μm is measured to be 35%, whereas the absorption is of the order of 2% in GaAs. With the help of high laser intensity and a reflective backside however, signals from a 1084 nm laser diode and 1064 nm Nd:YAG were detected with a GaAs Schottky diode and strip detector respectively.

Two sources of charge injection were used to characterize the CMS Si pixel detector prototype: the test pulses and the laser pulses. The measurements with both sources were incorporated in the same experimental setup. The distribution of trim bits and threshold were only determined by means of the test pulses; spatial resolution can only be studied with the laser pulses, while full depletion voltage, pulse shape and gain factor were studied with both sources.

Two kinds of light sources were employed: a 670 nm laser diode and a 1064 nm Nd:YAG laser. At the wavelength of 670 nm the penetration depth of light is of the order of 10 μm so that the energy is deposited only on the surface of the bulk. A 1064 nm laser, on the contrary, can be used to simulate charged particle track because the free carriers are generated homogeneously along the propagation path. The test station with the laser diode is simple, low-cost and easy for focusing; therefore it is more suitable to investigate the parameters such as full depletion voltage, pulse shape and gain factor; Nd:YAG laser, on the other hand is a more reliable instrumentation to study the spatial resolution.

The results of the full depletion voltage, the peaking time and the time walk with two different charge sources are comparable. The full depletion voltage was given as 30 V(34 V) according to the measurement with the test(laser) pulses. The peaking time was measured to be in the range of 30-41 ns with the different amplitudes of the test pulses. It was determined to be 44 ns with the laser pulses; this can be explained by the pulse length of the laser, which is of the order of 10 ns. The time walk is evaluated as 5.0(7.4) ns with two sources. The performance regard to the gain factors and linearity was found to follow the same pattern according to the measurements with the test pulses and the laser pulses. However, a quantitative comparison is missing without an accurate calibration of the laser intensity.

The spatial resolution was determined by the distribution of the residuals. The free cluster search algorithm and the center of gravity method were employed to evaluate the coordinates.

The spatial resolution was measured with four different configurations: two different wavelengths (670 nm and 1064 nm) and moving(unmoved) stage. It can been seen that the resolution is dependent on the signal-to-noise ratio and the cluster size. The resolution is improved when the signal-to-noise ratio increases from 10 to 20. It is also improved when the cluster size increases from 2 to 3.; the enhancement is not significant when the signal is spread over more than 3 pixels. With a cluster size of 3 a resolution of 2.1 μm was achieved.

The work demonstrated the applicability of a laser system to characterize the CMS pixel detectors. The benefit of using a laser system is the provision of a flexible test stand, easy trigger system, high statistic and completely controllable source for the laboratory use. However, in order to measure the parameters such as gain factors, the calibration of the laser power with high resolution is demanded. It is also desirable to limit the pulse length of the laser to the order of 1 ns in order to improve the resolution in peaking time and spatial resolution of the detector.

Acknowledgements

I would like to thank Prof. Lübelsmeyer for giving me the opportunity to study in Germany, to work on this interesting subject and for his guidance and insight. I would also like to thank Prof. Schael for his great support during the time at his institute.

My special thanks to Dr. Pandulas and St. König for their careful reading of the manuscript. I am also very grateful to J. Breibach, St. König and B. Wittmer for the fruitful discussions. Furthermore, my great appreciation to W. Karpinski and G. Piershel for their useful suggestions by the operation and the readout of the AC30 chip.

I am also grateful to all the members of the personnel, the electrical and mechanical workshops of the I. physics institute in Aachen for their assistance. Most of all I would like to thank my husband Bo and my parents for their encouragement and patience.

List of Figures

List of Tables

Bibliography

[1] S. Glashow, Nucl. Phys. 22 (1961) 579;
A. Salam, Phys. Rev. 127 (1962) 331;
A. Salam, Proc. 8th Nobel Symposium, ed. N. Svartholm (Almquist & Wiksell, Stockholm) (1968) 367;
S. Weinberg, Phys. Rev. Letters 19 (1967) 1264

[2] LEP Collaborations, A Combination of Preliminary Electroweak Measurements and Constraints on the Standard Model, CERN-EP/2001-021, Feb 28, 20001

[3] P.W. Higgs, Phys. Letters 12, pp. 131, 1964;
P.W. Higgs, Phys. Rev. Letters 13, pp. 508, 1964;
P.W. Higgs, Phys. Rev. 145, pp. 1156, 1966

[4] D. Bomeštar, *SM Higgs Search at LHC*, CMS TN/95-156, CMS technical note

[5] M. Dittmar, *Searching for the Higgs and other Exotic Objects*, CMS CR 1999/009, CMS reference report, Feb. 23 1999

[6] L3 Collaboration *et al.*, *Higgs candidates in* e^+e^- *interactions at* $\sqrt{s}$*=206.6* GeV, Physics Letters B, Vol 495, pp. 18-25, 2000

[7] F. Pauss and M. Dittmar, *Experimental Challenges at the LHC*, CMS CR 1999/008, CMS conference report, Feb. 23 1999

[8] The LHC Study Group, *Conceptual Design of the large Hadron Collider*, CERN/AC/95-05 (LHC)

[9] M. Spira, *Standard Model Higgs cross sections (NLO) and PYTHIA*, CMS Note 1997/080, CMS note 1997

[10] S. Gonzślez, *Physics prospects with the ATLAS detector at the LHC*, QFTHEP'97, Semara/Russia, 1997

[11] CMS Collaboration, CMS, *Technical Proposal*, CERN/LHC 94-38

[12] CMS Collaboration, CMS, *The Muon Project*, Technical Design Report, CERN/LHC 97-32

[13] CMS Collaboration, CMS, *The Hadron Calorimeter Project*, Technical Design Report, CERN/LHC 97-31

[14] CMS Collaboration, CMS, *The Electromagnetic Calorimeter Project*, Technical Design Report, CERN/LHC 97-33

[15] CMS Collaboration, CMS, *The Tracker Project*, Technical Design Report, CERN/LHC 98-6

[16] CMS Collaboration, *Addendum to the CMS Tracker TDR by the CMS Collaboration*, CERN/LHC 2000-016, CMS TDR 5 Addendum 1, 21 February 2000

[17] M. Lenzi, *Performance of the all-silicon CMS Tracker*, Elsevier Preprint, Firenze/Italy, Nov. 22th 2000

[18] F. Hartmann, *The CMS All-Silicon Tracker-Strategies to ensure a high quality and radiation hard Silicon Detector, VCI 2001*, Preprint Elsevier, Karlsruhe/Germany, Mar 22th, 20001

[19] J. Breibach *et.al., Development of GaAs Pixel Detectors*, Dissertation, Preprint RWTH Aachen, PITH 00/14, 2000

[20] J. Breibach *et al.*, *Development of a bump bonding interconnect technology for GaAs pixel detectors*, Nucl. Instr. and Math. A 470 (3), pp. 576-582, 2001

[21] J. Breibach *et al.*, *Investigation of a bump bonding interconnect technology for GaAs pixel detectors*, Nucl. Instr. and Math. A 470 (3), pp. 571-575, 2001

[22] W. Karpinski et al, *Pixel Readout Electronics in Honeywell SOI CMOS*, Proceedings of the fourth Workshop on Electronics for LHC Experiment, Rome/Italy, CERN/LHCC/98-36, Sep. 21-25 1998

[23] W. Karpinski et al, *Performance Studies of Pixel Readout Electronics in RICMOS IV-SOI and DMILL processes*, Proceedings of the fifth Workshop on Electronics for LHC Experiment, Snowmass, Clorado/USA, Sep. 20-24 1999, CERN/LHCC/99-33

[24] R. Baur, *Readout Architecture of the CMS Pixel Detector*, Elseview Preprint, PSI, Oct. 24, 2000

[25] G. Piershel, private communication

[26] W. Wagner et.al., *Characterization of silicon microstrip detectors using an infrared laser system*, Nucl. Instr. and Math., A 423, pp. 303-319, 1999
Y. Unno *et al., A new laser test stand for simulating charged-particle tracks*, Nucl. Instr. and Math. A 383, pp. 238-244, 1996
J. Krizmanic et. al., *A 1064 nm diode laser system for dynamically probing silicon detectors*, Nucl. Instr. and Math. A 374, pp. 315-319, 1996

J. Simon-Gillo *et al.*, *Characterization and quality control of silicon microstrip detectors with an infrared diode laser system*, Nucl. Instr. and Math., A 352, pp. 573-578, 1995

[27] S.M. Sze, *Physics of Semiconductor Devices*, John Wiley & Sons, New York, 1981

[28] P. Widmann, Diploma Thesis, Ludig-Maximilians-Universität, Munich, MPI Report, MPI-PhE/94-21, September 1994

[29] G. E. Jellison and D. H. Lowndes, *Optical absorption coefficient of silicon at 1.152 μm at elevated temperatures*, Appl. Phys. Lett,. 41, pp. 594-596, 1982

[30] B. N. Brockhouse, *Lattice vibrations in silicon and germanium*, Phys. Rev. Lett, Vol 2, pp. 256-258, 1959

[31] C. D. Thurmond, *The Standard thermodynamic functions for the formation of electrons and holes in Ge, Si, GaAs and GaP*, J. Electrochem. Soc., Vol. 122, pp. 1133-1141, 1975

[32] J. C. Sturm *et al.*, *Silicon Temperature Measurement by Infrared Absorption: Fundamental Processes and Doping Effects*, IEEE Transactions on Electron Devices. 39(1), pp. 81-88, 1992

[33] S. Morris, *Technical Documentation of Lambda 2 Spectrometer: RS-232-C Interface*, Perkin Elmer, Ueberlingen/Germany, August 1988

[34] H. A. Weakliem and D. Redfield, Temperature dependence of the optical properties of silicon, J. Appl. Phys. 50(3), pp. 1491-1493, 1979

[35] J. I. Pankove, *Optical Process in Semiconductors*, Dover Publications, Inc. New York, 1975

[36] S.R. Johnson and T. Tiedje, *Temperature dependence of the Urbach edge in GaAs*, J. Appl. Phys., 78(9), pp. 5609-5613, 1995

[37] M. Topowski, *Development and Characterization of Tracking Detectors made of SI-GaAs for the LHC Experiments*, Dissertation, Preprint RWTH Aachen, PITHA 97/7

[38] R. K. Willardson and A. C. Beer, *Semi-Insulating GaAs*, published in *Semiconductors and Semimetals*, Vol. 20, Academic Press, Orlando, 1984

[39] E.Weber, *Imperfections in III/V Materials* published in: R. K. Williard and A.C. Beer, *Semiconductors and Semimetals*, Vol. 38, Academic Press, Boston, 1993

[40] W. Walukiewicz *et al.*, *On the optical evaluation of the EL2 deep level concentration in semi-insulating GaAs*, Appl. Phys. Lett., 43(2), pp. 192-194, 1983

[41] W. Xiao, *Investigation of Radiation Hardness of SI GaAs Detectors for their Application in the Tracking System at the LHC Experiments*, Dissertation, Preprint RWTH-Aachen PITHA 98/18

[42] P. Silverberg *et.al.*, *Hole photoionization cross sections of EL2 in GaAs*, Appl. Phys. Lett, 52(20), pp. 1689-1691, 1988

[43] S. K. Brierley and D. S. Lehr, *Full-Wafer mapping of total and ionized EL2 concentration in semi-insulating GaAs using infrared absorption*, Appl. Phys. Lett., 55(23), pp. 2426-2428,1989

[44] M. Beaudoin, *et al., Optical absorption edge of semi-insulating GaAs and InP at high temperatures,* Appl. Phys. Lett., 70(26), pp. 3540-3542, 1997

[45] J. I. Pankove, Phys. Rev. 140, A 2059, 1965

[46] O. Kappertz, private communication

[47] Technical Data, SDL-6702-H1, SDL

[48] W.Wallraff *et.al., Space flight experience with the AMS infrared Tracker Alignment System*, Proceeding of the 27th International Cosmic Ray Conference, Hamburg/Germany, August 2001;
J. Vandenhirtz, *Ein Infrarot Laser Positions-Kontroll-System für das AMS Experiment*, Dissertation, RWTH-Aachen, September 2001

[49] Th. Kubiki *et.al.*, *Calculation of the Electric Field in GaAs Particle Detectors,* Nucl. Instr. and Math. A 345, pp. 468-470, 1994

[50] Ramo, P.I.R.E. 27, pp. 584, 1939

[51] St. König, *Aufbau eines Teststandes für Silizium-Zähler des Spurdetektors im CMS-Experiment*, Diploma thesis, Preprint RWTH-Aachen, PITHA 99/5

[52] B. Wittmer, Dissertation in preparation

[53] O. Syben, *GaAs Strip and Pixel Detectors for Application in High Energy Physics*, Dissertation, Preprint RWTH-Aachen, PITHA 99/13

[54] D. Albertz *et al., Beam test measurements on GaAs strip and pixel detectors*, Nucl. Instr. and Math. A 410 (1) pp. 1-5, 1998

[55] M. Morrissey, SEQSI, December 1993

[56] V. Commichau, F. Beißel, PreMux AD00, 1996

[57] L. Jones, PreMux128 Specification 2.3, Rutherford Appleton Laboratory

[58] F. Beißel, VFADC50 Version 1.0, 1998

[59] Benutzhandbuch, DIG 16-I/O, ROTEC Industrieautomation GmbH

[60] Technical Information Manual, MOD. V 729A, C.A.E.N, December 1998

[61] User's Guide, HP 8110A 150 MHz Pulse Generator, March 1993

[62] Technical Data, HL6720G, Hitachi

[63] Technical Data, TLD-670-11A, Newport

[64] Instruction Manual, Laser Model QTL-021QT, Laser2000

[65] B. Wittmer, private communication

[66] W.R. Leo, *Techniques for Nuclear and Particle Physics Experiments*, Springer Verlag, Berlin, 1993

[67] E. Nygȧrd et al., *CMOS low noise amplifier for microstrip readout Design and results,* Nucl. Instr. and Math. A 301, pp. 506, 1991

[68] D. Quadflieg, *Vergleichende Messungen an Pixelelektronik-Chips für das CMS-Experiment*, Diploma thesis, RWTH-Aachen, 2000

[69] A. Peisert, *Silicon Microstrip Detectors*, published in: Fabio Sauli, *Instrumentation in High Energy Physics*, World Scientific, CERN Geneva, 1992

Lebenslauf

Ich wurde am 20. Oktober 1970 als Tochter von Zhou Cui Feng und Zhen Biao Gu in Shanghai, V.R. China geboren. Die Abiturprüfung legte ich im Juli 1988 am Shanghai Jian Qing Gymnasium ab. Im September 1988 habe ich ein Studium der Physik an der Shanghai Jiao Tong Universität erworben und im Juli 1992 schloss ich das Hauptstudium mit B.S. ab. Zum Wintersemester 1993 nahm ich das Studium der Physik an der RWTH Aachen auf und habe die Diplomarbeit mit dem Titel "Konzipieren, Aufbau und Test eines Kühlsystems für die Spurdetektoren des CMS-Experimentes am LHC Speicherring" im Sommersemester 1996 am I. Physikalischen Institut der RWTH Aachen angefertigt. Die abschlissenden Diplomprüfungen legte ich im Oktober 1996 mit Erfolg ab. Im November 1996 begann ich unter der Leitung von Prof. Dr. K. Lübelsmeyer mit der Anfertigung der vorliegenden Dissertation "Characterization of the CMS Pixel Detectors".